UNIVERSITÀ DEGLI STUDI DI PARMA

DOTTORATO DI RICERCA IN
INGEGNERIA INDUSTRIALE

CICLO XXXVII

Thermoelastic models for layered structures. Applications to laminated glass

Coordinatore:

Chiar.mo. Prof. Gianni Royer-Carfagni

Tutore:

Chiar.mo. Prof. Gianni Royer-Carfagni

Co-Tutore:

Prof. Laura Galuppi

Dottorando: **Ali Haydar**

ANNI ACCADEMICI 2021/2022-2023/2024

Abstract

This work focuses on the structural and thermal analysis of layered structures. The first half is dedicated to studying the structural response of laminated glass beams through both analytical and numerical methods. My primary contribution in this area is the introduction of the "Special Zigzag" theory. In addition to providing analytical solutions for common engineering problems, I developed a finite element to address more general cases.

The second half of the work concentrates on the transient heat conduction problem. My contribution here involves developing a novel flux-based variational principle, which builds on the original variational/Lagrangian analysis of heat conduction formalized by M. Biot. This new variational principle greatly simplifies the thermal analysis of composite structures made from materials with varying thermal properties. It also facilitates the formulation of a simple and accurate C^0 isoparametric finite element.

The work is further supported by a variety of examples that serve both as validation and practical applications for the developed concepts.

To Abu Hadi

1960-2024

Contents

List of Figures

List of Tables

Chapter 1

Introduction

I present here my modest contribution to the development of thermoelastic models for layered structures. The work can be divided into two major parts: the development of the "Special Zigzag" theory for inflexed laminated glass beams and the formulation of the "neat" flux-based weak formulation for transient thermal analysis.

1.0.1 Objectives

The primary objectives of this thesis can be outlined as follows:

- Development of a Novel Model for Inflexed Laminated Glass Beams: This includes the introduction of the "Special Zigzag" theory, which provides a framework for understanding the mechanical behavior of laminated glass beams by integrating both classical and advanced modeling techniques.
- Innovation in Thermal Analysis via Variational Principles: This involves extending M. Biot's framework for transient thermal analysis through the proposal of a novel flux-based weak formulation, thereby enhancing the analysis of inhomogeneous materials and complex thermal conditions.

1.0.2 Outline

Here is a short outline of the work done in the thesis, divided into six chapters. The work includes a novel model for inflexed laminated beams and a variational treatment of the thermal problem in solids and composites.

Chapter 2: **Advanced theories for laminated beams**: This chapter provides a review of the treatment of laminated beams, tracing the evolution of modeling techniques from classical approaches to advanced theories. Starting with Timoshenko's beam theory and progressing through the development of layer-wise and zigzag theories, ending with introducing the author's novel contribution, the "Special Zigzag" theory. The analytical solution based on the special zigzag theory is specific to a certain configuration, while the Finite Element based on the special zigzag theory can handle a variety of cases with different loading configuration and boundary conditions.

Chapter 3: **Laminated glass beams**: In this chapter, a straightforward model for inflexed multilayered laminated glass beams based on the Special Zigzag theory is developed. The analytical solution for multilayer laminated glass balustrades is derived. This solution eliminates the need to consider the effective thickness—the thickness of a monolithic beam with equivalent bending properties in terms of stress and deflection—and the complications related to it. The chapter includes practical examples and numerical experiments to illustrate the application and efficiency of the proposed model.

Chapter 4: **Thermal analysis via variational principles**: In this chapter, the ingenious approach developed by M. Biot in the 1950s for transient thermal analysis in solids is presented. Biot sought to create a comprehensive framework for analyzing irreversible phenomena by transforming the classical mechanics concept of virtual work. He introduced a broader perspective through the variational scalar product, which serves as an advanced extension of the principle of virtual work within functional space. This opened the door to developing a treatment of irreversible phenomena that involves Lagrangian-type equations and generalized coordinates. The resulting equations are, in part, a true variation of scalars, and the other part is similar to generalized forces in Lagrangian mechanics.
Here, the author's contribution, summarized by a novel flux-based weak formulation for thermal problems, is presented. This formulation develops Biot's variational principle by considering the "heat displacement" field, whose time derivative is the heat flux, as a primary variable, while the temperature only appears as a boundary term. The fact that the heat displacement field is more regular than the temperature field allows for the natural treatment of inhomogeneous materials, thermal shocks, and uneven heating conditions. Additionally, a comparison between the neat variational principle and the classical one developed by Biot, along with the numerical implementation of the neat flux-based variational principle in a C^0 isoparametric FE framework, is presented.

Chapter 5: **Validation and Numerical Examples**: The novel variational principle presented in Chapter 4 is validated through several examples from the literature. The remainder of this chapter includes examples related to laminated glass under convective boundary conditions and composites with Interfacial Thermal Resistance (ITR).

Chapter 6: **Final remarks.** The concluding chapter offers a summary of the contributions and conclusions derived from this study.

Chapter 2

Advanced Theories for Laminated Beams

2.1 Modeling of Plain Laminated Beams

A review of the theories related to modeling of plain laminated beams is in order. This will help to build a coherent understanding of beam theories arriving to the novel contribution the author has suggested. This chapter is mainly concentrating on theories that are formulated in terms of displacement fields.

2.1.1 Timoshenko Beams

Beam bending problems are analyzed based on assumptions about the displacement field, influenced by beam properties affecting its structural response. Bending characteristics are affected by the beam dimensions, loading configuration, and the amount of deflection it undergoes. In the small deflection regime, a main distinction has been made regarding the dimensions of the beam, the slender beams, and the thick beams. The former's structural response to lateral loads is characterized by an insignificant effect of shear stress and deformations, consequently, the main assumption is that a plain cross-section that is perpendicular to the beam axis remains plain and perpendicular to that axis after deformation (normal orthogonality condition). This assumption characterizes the behavior of Euler–Bernoulli beams. Additionally, these beams are characterized by two more assumptions: the deflection of a point that belongs to a cross-section is small and equal to the deflection of the beam axis, and the lateral displacements are negligible. From a finite elements perspective, the aforementioned assumptions result in a definition of strains that involves the second derivative of deflection; consequently a C^1 continuity is required. The geometrical degrees of freedom (DOFs) are the deflection and it's first derivative, and the determination of the deflection is sufficient to assess the stress state in the structure.

This approximation, which works well for slender beams, becomes unreliable for considerably thick beams or beams that are axially loaded with significant eccentricity, and for composite beams where the shear deformation and stresses are significant. In these cases, the normal orthogonality condition no longer holds. Instead, it is assumed that a plain cross-section normal to the beam axis before deformation remains plain but not necessarily perpendicular to the beam axis after deformation. This assumption characterizes what is commonly known as Timonshenko's beam theory. In this theory, the displacement field takes the following form :

$$u(x,z) = u_0(x) - z\theta(x) \quad ; \quad w(x,z) = w_0(x) \tag{2.1}$$

Here, $u(x,z)$ represents the displacement in the axial direction, $u_0(x)$ is the axial displacement of the beam axis, $\theta(x)$ is the rotation angle, and $w(x,z)$ denotes the transverse displacement.

The rotation angle $\theta(x)$ represents an average rotation of the deformed cross section, which remains plain after deformation Figure 2.1.

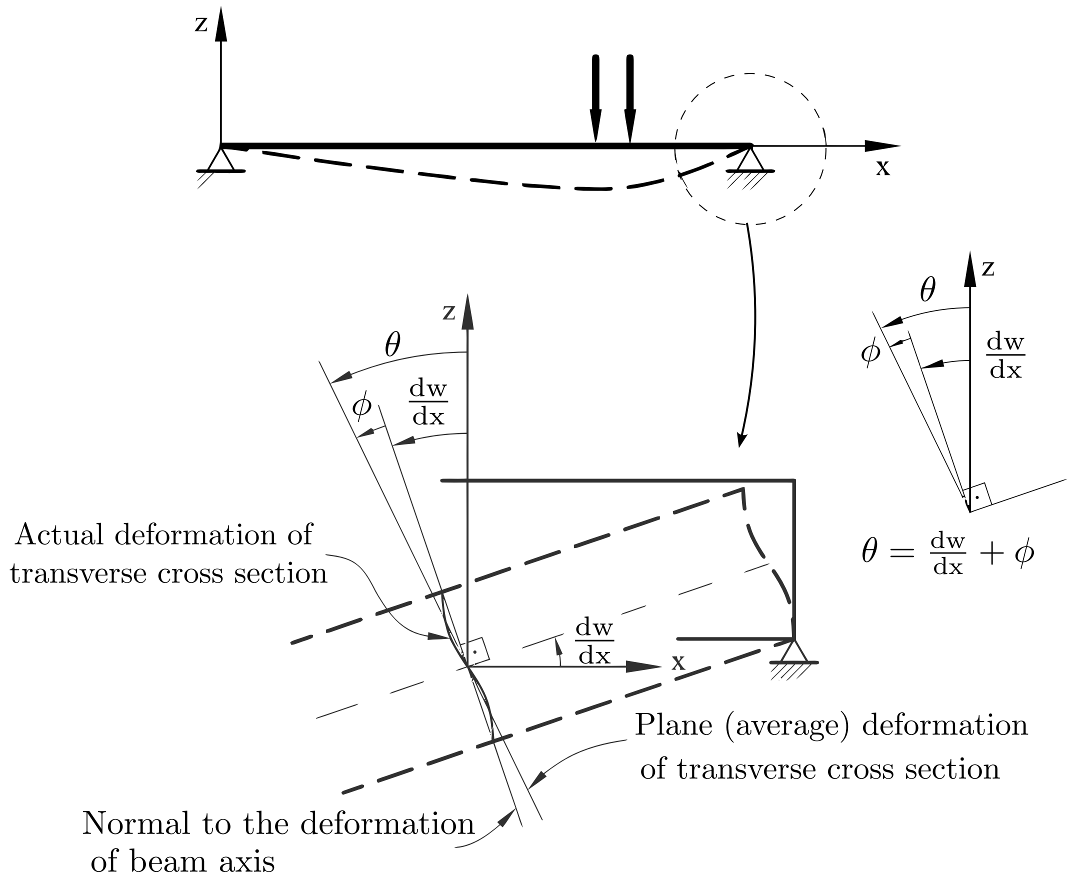

Figure 2.1: Timoshenko beam theory. Rotation of the transverse cross section[1].

The strains, under the assumptions of Timoshenko's theory, are all functions of the first derivatives of the displacement variables; consequently, the finite element formulation requires C^0 continuity. Nonetheless, the finite element suffers from shear locking problems, resulting in unrealistic stiffness of slender beams. This issue has many solutions, like reduced integration, linked interpolations, etc. A noteworthy issue with Timoshenko's beam theory is that it provides inadequate predictions when applied to relatively thick composite beams with material layers that have a high difference in stiffness characteristics: even with a well-chosen shear correction factor, the axial stress at the extrados and the intrados is underestimated. Furthermore, the transverse shear stress at the interface between the layers exhibits erroneous discontinuities. The main reason for these shortcomings is related to the fact that the real variation of in-plain displacement is more complex than that considered in Timoshenko's theory, especially when the layers of a composite beam have high differences in shear stiffness as in laminated glass. Although Timoshenko's theory has significantly improved predictions by considering shear deformation and stress, the shortcomings mentioned above required further developments. Timoshenko's theory can also be called the first order shear deformation theory, next section presents a glance at the higher-order shear deformation theories.

2.1.2 Higher-order Shear Deformation Theories

Considering that the first-order shear deformation theory predicted a uniform shear stress through the thickness, which is generally in violation of the surface conditions, this theory required correction factors derived from a comparison with elastic solutions. Lo *et al.* [2] suggested the addition of higher-order terms as a function of the thickness coordinate to the displacement field in order to better approximate the shear stress distribution. Reddy [3] developed a higher-order shear deformation theory for laminated elastic shells, in which he accounted for the parabolic distribution of shear strains through the thickness. [4] demonstrated a generalized expression for the displacement field in higher-order shear deformation theories:

$$u(x,z) = u_0(x) + \psi(x)z + \xi z^2 + \phi z^3 \quad ; \quad w(x,z) = w_0(x). \tag{2.2}$$

Many other similar theories are reported in the literature. Theories with a displacement field of a degree higher than the third order are also reported; nonetheless, all these theories that consider a continuous displacement field over the thickness had difficulties approximating the zigzag distribution of the axial displacement, especially in the case of laminated structures with highly heterogeneous layers.

2.1.3 Layer-Wise Theories

The special structural response of laminated beams with highly heterogeneous layers requires a more detailed representation of the displacement field; consequently, layer-wise theories emerged during the 1980s, as formulated by Reddy and Barebo [5]. Layer-wise theories describe the displacement field individually for each layer of the laminate; consequently, the displacement field for the laminate results from the assembly of these displacement fields. Theories that assume a continuous axial displacement field on the entire laminate, like Shear Deformation theories, lose the ability to capture the zigzagging distribution of axial displacement through the beam's thickness and produce an incorrect stress on the interface between the laminate's layers. Different physical continuity requirements are enforced, including the interfacial continuity of displacement as in [5] and interlaminar continuity of the shear and axial stresses as in [6]. The displacement field in layer-wise theories can be seen as a linear combination of a known function of the thickness and an independent function of the position within each layer.

The displacement field in layer-wise theories takes the form:

$$u(x,z) = \sum_{j=0}^{N} u^j(x) N_j(z) \quad ; \quad w(x,z) = w_0(x) \tag{2.3}$$

Where N is the number of analysis layers, u and w are the axial and vertical displacements respectively, and N_j is the linear shape function for each layer, Figure 2.2 shows the axial displacement field. On the contrary to Timoshenko's theory

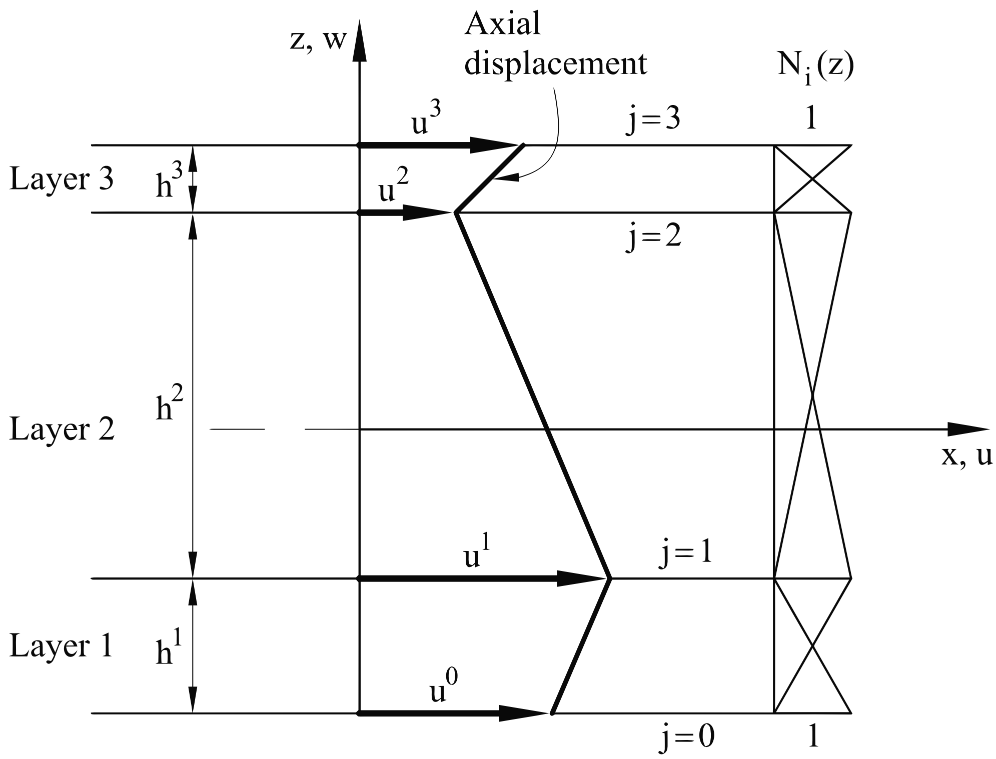

Figure 2.2: Distribution of the axial displacement field for three-layered beam in layer-wise theory [1].

and Shear Deformation theories, the layer-wise theory doesn't require any shear correction factors and the resulting equations of motion include the same variables, as in the first-order shear deformation theory. It was found that the layer-wise theory by [6] is the most accurate theory among all laminate theories available in the literature [4]. Nonetheless the computational efficiency is low because the number of kinematic variables increases with the number of the laminate's layers.

2.1.4 Zigzag Theories

The inefficiency of Layer-Wise theories due to the increment of kinematic variables with the increase in the number of layers was addressed by zigzag theories. These theories can be considered a subclass of Layer-Wise theories because they describe the displacement field of the individual layers. By assuming a piecewise zigzag axial displacement, these theories break the dependence of the number of kinematic variables on the number of laminate layers.

In early zigzag theories [7], [8], only the displacement continuity condition on the interfaces of the layers was considered. Capturing the zigzag distribution of displacement in the thickness direction was the main advantage of these theories; consequently, the C^0 assumption of the zigzag displacement results in constant shear stress in each layer. In both cases, a post-processing technique had to be used to obtain the true values of shear stress. The theory by [8] relied on a variational principle by Reissner [9] and demonstrated that including a zigzag-shaped C^0 function improves the prediction of the axial displacement over the thickness much better than including higher-order smooth functions, even for thick beams. Although layer-wise theories like [10] can capture the zigzag distributions of the axial displacement through the thickness, assuming the zigzag distribution *ab initio* as in [7] allows the contact condition on transverse shear stress to be automatically satisfied.

The aforementioned first-order zigzag theories [7], [8] produce good predictions of global behavior, i.e., buckling loads and natural frequencies; nonetheless, this is only true in the case of symmetric laminates. Some zigzag theories have added higher-order terms to approximate the zigzag distribution of axial displacement but still had problems predicting the correct transverse shear stresses and suffered theoretical difficulties in satisfying equilibrium at fixed supports. The displacement field by [7] requires C^1 continuity to approximate the deflection field, which is a drawback with respect to theories based on Timoshenko's assumptions. The kinematic field in zigzag beam theories is written as follows:

$$u^k(x,z) = u_0(x) - z\theta(x) + \bar{u}^k(x,z) \ ; \ \ w(x,z) = w_0(x), \tag{2.4}$$

where

$$\bar{u}^k = \phi^k(z)\psi(x), \tag{2.5}$$

The uniform axial displacement $u_0(x)$, the rotation $\theta(x)$, and the transverse deflection $w_0(x)$ are the primary kinematic variables of the underlying single-layer Timoshenko beam theory. The function $\phi^k(z)$ denotes a piecewise linear zigzag function, yet to be established, and $\psi(x)$ is a primary kinematic variable that defines the amplitude of the zigzag function along the beam's axis.

Averill [11] has proposed a finite element based on a generalized form of linear zigzag theory, where the number of kinematic variables is independent of the number of laminate layers. Using a penalty function and an interdependent element interpolation scheme, he enforced the continuity of transverse shear stress, which allowed for the formulation of a C^0 finite element. In a later work, Averill *et al.* [12] developed another C^0 finite element based on a quadratic layer-wise zigzag theory, and by enforcing the consistency of the shear strain field, they eliminated the shear locking problem. Despite these improvements, these works suffer from errors in modeling clamped supports. Cho *et al.* [13] suggested a higher-order theory for general lamination by superimposing a cubic displacement field on the linear zigzag displacement, in which the choice of a cubic displacement field was made to account for the parabolic distribution of the transverse shear stress, and the linear zigzag distribution is needed to accommodate strain discontinuities necessary for accounting for the contact stress continuity. The displacement field of Cho's theory [13] can be expressed in a generalized form as follows:

$$u^k(x,z) = u_0^k(x) + u_1^k(x)z + u_2(x)z^2 + u_3(x)z^3 \ ; \ w^k(x,z) = w_0(x) \ . \tag{2.6}$$

Cho's theory represents the first zigzag approach that enables direct and accurate calculations of shear stresses derived from constitutive equations. However, it has two main drawbacks: first, the natural boundary conditions necessitate a higher-order resultant due to the self-equilibrating stress distribution through the thickness; second, the transverse shear stresses calculated from the constitutive equations erroneously vanish at the clamped boundary.

2.1.5 Refined Zigzag Theory (RFT)

Tessler *et al.* [14], [15] developed a variationally consistent refined zigzag beam theory for composite and sandwich beams, relying primarily on the kinematic variables of first-order shear deformation theory and on a piecewise-linear zigzag displacement field. The proposed linear zigzag function vanishes at the top and bottom surfaces of the beam, and the continuity of transverse shear stress across the beam section is not enforced; consequently, the true shear stress distribution is approximated correctly by a simple piecewise-constant function. The refined zigzag theory doesn't face any issues in correctly modeling clamped supports. The displacement field of RFT takes the following form:

$$u^k(x,z) = u_0(x) - z\theta(x) + \phi^k(z)\psi(x) \ \ ; \ \ w(x,z) = w_0(x)\,, \tag{2.7}$$

where the zigzag function ϕ^k is expressed in the following manner

$$\phi^k = \frac{1}{2}(1-\xi)\bar{\phi}^{k-1} + \frac{1}{2}(1+\xi)\bar{\phi}^k\,. \tag{2.8}$$

Here ϕ^k and ϕ^{k-1} are the values of the zigzag function at the kth and $k-1$th interfaces. Figure 2.3 demonstrates the main feature of the refined zigzag theory, where the value of the zigzag function vanishes at the external and internal surfaces

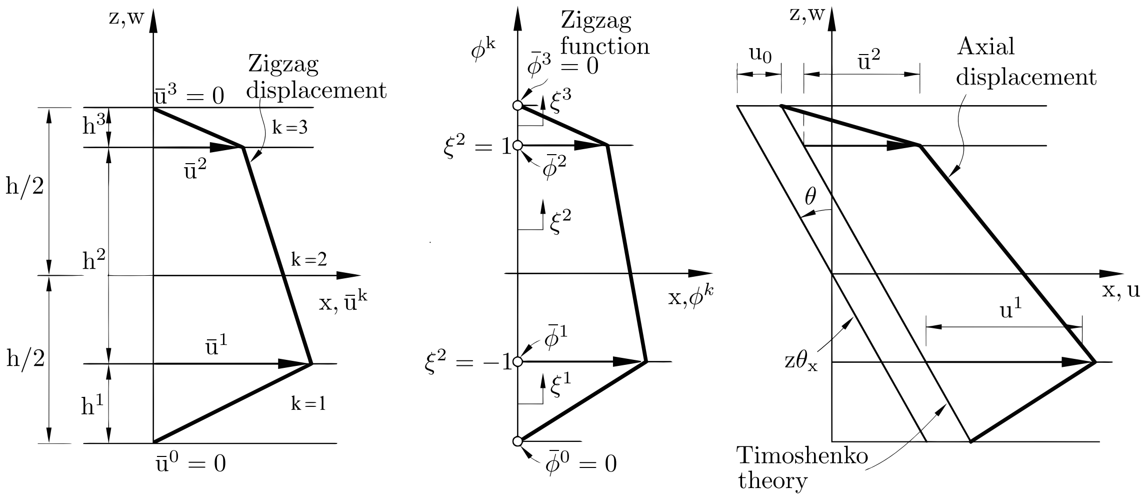

Figure 2.3: Refined zigzag theory. (a) Distribution of zigzag function ϕ^k ,(b) zigzag displacement u^k and (c) axial displacement u, for a 3 layered section [1].

of the beam, i.e. $\bar{\phi}^0 = \bar{\phi}^{nl} = 0$. The non dimensional coordinate $\xi^k = \frac{2(z-z^{k-1})}{h^k} \in (-1, 1)$ is depicted in Figure 2.3.

In a more recent work, Tessler *et al.* [16] relied on the concept of limiting homogeneity as a way to determine appropriate zigzag functions, resulting in four distinct sets of zigzag functions, including the above-mentioned zigzag function [15]. They also utilized the concept of limiting homogeneity in the analysis of homogeneous plates using zigzag kinematics. Many FEs based on the RZT were developed. Gherlone *et al.* [17] introduced two- and three-node C^0 beam elements for multilayered composite and sandwich laminates, in which they applied three different types of constraints and non-isoparametric interpolation to avoid the shear stiffening issue in slender beams. Consequently, it was found that the two-node element with constant shear-force constraint is the most accurate element among the formulations they proposed. A simpler derivation of an accurate finite element based on the RZT was developed in [18]; in this element, the shear stiffening issue was resolved using reduced integration.

2.2 Special Zigzag Theory

To address highly heterogeneous laminates with significantly differing shear stiffness properties between adjacent layers, the author recently developed the Special Zigzag theory [19]. This theory is displacement-based and models laminates consisting of alternating stiff and soft layers, assuming that cross-sectional warping is a piecewise linear function of the beam's thickness, akin to the RZT. However, unlike the RZT, the Special Zigzag theory treats the stiff layers as Euler-Bernoulli beams, neglecting their shear deformation, while the soft layers are considered to have no bending or axial stiffness. Thus, these soft layers solely facilitate shear coupling between the stiff layers. The proposed displacement field of the Special Zigzag theory is

$$u_k(x,z) = u_0(x) - z[w_0'(x) - \psi(x)] + \phi_k(z)\psi(x) \ ; \ w_k(x,z) = w_0(z)\,, \tag{2.9}$$

where the rotation $w_0'(x) = \frac{dw_0}{dx}$ is combined with the amplitude of the zigzag function $\psi(x)$ to account for average rotation due to deflection and shear. The variable $u_0(x)$ is the axial displacement of the section's centroid, and $\phi_k(z)$ is the zigzag function of the kth layer. One can note that the number of variables is similar to the number of variables in the first-order shear deformation theory.

The axial displacement of the special zigzag theory equation 2.9 can be written in a generalized form to relate to the other displacement-based theories mentioned previously:

$$u^k(x,z) = u_0^k(x) + u_1(x)z + u_2^k(x,z) \tag{2.10}$$

The Special Zigzag theory allows for analytic solutions in specific loading and boundary conditions; however, a notable drawback is its requirement for C^1 continuity in interpolating the transverse deflection $w_0(z)$. As a result, developing a plate finite element becomes a challenging endeavor.

Chapter 3

Laminated Glass Beams

3.1 Laminated Glass

Laminated glass, a type of safety glass, consists of two or more glass plies bonded together with a polymeric interlayer, typically polyvinyl butyral (PVB). This composite is manufactured by bonding the glass plies and interlayers in an autoclave under high temperature and pressure. The interlayers enhance safety by providing post-breakage bonding, which prevents large, sharp glass fragments from forming, thereby reducing injury risk and maintaining load-bearing capacity [20]. Laminated glass is widely used in architecture, glazing, automobile safety, photovoltaic applications, and UV protection, and is particularly valuable in hurricane-prone areas. Additionally, it improves sound isolation, with the interlayer contributing to sound attenuation. In the following sections, I will delve into the conceptualization of the Special Zigzag theory, which offers a simplified model for inflexed multilayered laminated glass beams based on the refined zigzag theory. This chapter includes the underlying assumptions, the development of an analytic solution for simply supported beams, the numerical implementation in a finite element framework, and an analytic solution for the effective thickness of multilayered laminated glass cantilevered balustrades.

3.2 A Simple Model For Inflexed Multilayered Laminated Glass Beams Based on Refined Zigzag Theory

Section 2.2 provided a brief presentation of the Special Zigzag theory, and here is a comprehensive exploration of the theory and its applications. The primary focus is on the unique configuration of laminated glass, consisting of stiff glass layers surrounding compliant polymeric interlayers. This discussion addresses the pre-glass-breakage phase under the assumption of linear elastic behavior for the interlayer, where its elastic modulus varies with time and environmental temperature. Our approach employs a specialized version of the refined zigzag theory [14] for composites. The bending response of a laminated glass beam is defined by this configuration, where the thin interlayer is too compliant to contribute to bending or axial stiffness, yet it effectively facilitates shear coupling between the glass plies. Consequently, the bending response in terms of strength and stiffness falls between two extremes: the *layered limit*, where the interlayer is perfectly compliant, providing no shear coupling, and the *monolithic limit*, where the interlayer is rigid, preventing relative shearing between the bonded glass surfaces. Thus, a crucial aspect of glass engineering is determining the degree of shear coupling between the glass layers due to the interlayer [21], [22].

The quantification of shear coupling depends on various factors, including the shear stiffness of the interlayer, its thickness, the type and size of the structural element, as well as the constraint and loading conditions [23]. The shear stiffness properties of the interlayer are influenced by the material's viscoelasticity, which can be modeled using the Boltzmann superposition principle. This is often achieved through an expansion of the relaxation function via Prony's series [24] or by employing fractional calculus [25]–[27]. However, in this work, the quasi-elastic approximation for the interlayer [28] is adobted, neglecting the memory effect of the polymer and treating it as a linear elastic material. The effective shear modulus is considered to depend on temperature and the duration of the applied loads.

Various models have been developed to address the problem, primarily categorized into two main approaches. The first is the *effective thickness* approach, which represents the thickness of a monolith with properties equivalent to those of the laminate in terms of stress and deflections. This concept was adapted by Bennison *et al.* [29] from arguments for composite beams by Wölfel [30]. A simple formule for calculating effective thickness was included in the ASTM guidelines [31], initially applicable only to three-layered simply supported laminates, but it has since been extended experimentally to more general cases. Another method within this category is the enhanced effective thickness developed by Galuppi *et al.* [32], which was derived variationally for three-layered beams under various static schemes and loading configurations, and further adapted for plates [33] and different laminated sections [34]. The enhanced effective thickness has also been adopted by the Eurocode for glass structures [35]. These *effective thickness* approaches often rely on tabulated coefficients for different cases [36], [37]; if the specific case of interest is not included in the tables, calculations may be required that are not always familiar to structural engineers.

The other category of solutions to this problem involves solving the governing equations either analytically or numerically. This approach is more general and can accommodate a wider range of situations. Various assumptions underpin these models, primarily the work by Newmark *et al.* [38], which has been extended to triple-layered statically determinate beams [32]. Enhanced shear-deformation theories also fall into this category [39], [40], developed initially for laminated structures and later adapted for laminated glass [41]. However, as noted in section 2.1.3 these theories assume a smooth continuous function across the beam's thickness, failing to capture the zigzag distribution of axial displacement caused by the highly heterogeneous properties of laminated glass layers.

In contrast, layer-wise theories effectively capture this zigzag distribution but are computationally expensive [42] since the number of kinematic variables increases with the number of layers. The inefficiencies of layer-wise theories were later addressed by zigzag theories [43], which incorporate a piecewise linear zigzag function, thereby decoupling the number of kinematic variables from the number of layers and allowing for more efficient numerical implementation. Nonetheless, these theories faced challenges in modeling clamped supports [43], [44], an issue resolved by the Refined Zigzag Theory (RZT) [45].

Recently, Haydar *et al.* introduced the Special Zigzag Theory (SZT), which is based on RZT assumptions and specifically tailored for laminated glass sections [19]. This theory models laminated glass beams with arbitrary section compositions and differs from RZT by treating the glass layers as Euler-Bernoulli beams while considering the polymeric interlayer to have no bending capacity, functioning solely to provide shear coupling between the glass plies. This assumption accurately represents a laminated glass section, where the shear deformation of the glass layers can be neglected due to their slenderness, and the shear stiffness of the interlayer is the primary contributor to the laminate's bending response.

The main advantage of SZT is its simplified displacement field, independent of the laminated section's composition. While several simple models for laminated glass have been developed [46], these models typically handle only triple laminates. In contrast, SZT can manage any laminated glass section and, due to its simplicity, allows for closed-form solutions for basic static configurations like simply supported and cantilevered beams. In this work, I also present the development of a finite element model capable of addressing more complex cases. The following sections will detail the development of the SZT model.

3.2.1 The Mechanical Model

The most general cross section for a multi-laminated glass beams is composed of N layers, with N odd, specifically of $(N+1)/2$ glass plies bonded by $(N-1)/2$ polymeric interlayers. The generic layer k, for $k = 1 \dots N$, of thickness h_k, is made of glass (polymer) when k is odd (even). As represented in Figure 3.1, introduce the sectional reference system (y, z), with origin in the geometric centroid G of the cross section, so that the k-th layer is comprised between z_k and z_{k+1}. Let $h = \sum_1^N h_k$ denote the total height of the laminated beam and b its width.

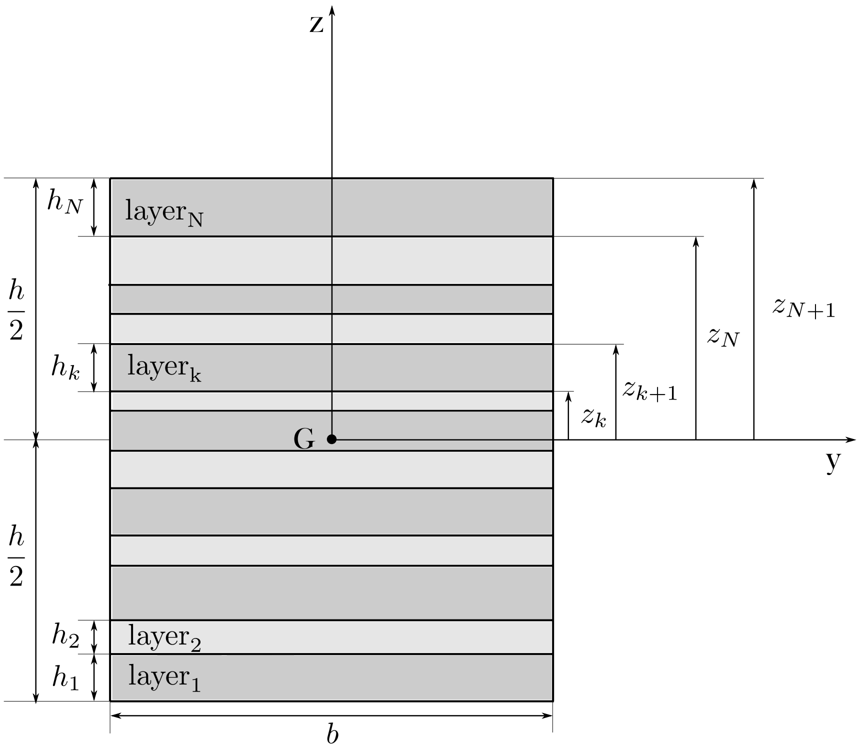

Figure 3.1: Schematics of the cross section of a multi-laminated glass beam of total height h, composed of N layers, with representation of the reference frame. The layer k of height h_k, for $k = 1 \dots N$, is made of glass for k odd, and of polymer for k even.

3.2.2 Kinematic Hypotheses

The warping of the cross-section due to bending is approximated as a piecewise linear function, dependent on the kinematic fields. Unlike the traditional approach of RZT, which treats all laminate layers as Timoshenko beams, the current model considers the glass plies as Euler-Bernoulli beams, neglecting their shear deformation. The interlayers are assumed to have no bending or axial stiffness, primarily providing shear coupling for the glass plies. This assumption is based on the fact that glass plies are generally much stiffer than the interlayer, and the ratio of glass thickness to span is typically low, leading to significant model simplifications.

The description of the section properties is introduced in a reference system where the x axis is orthogonal to the y and z axes, as shown in Figure 3.1. Here, $x \in (0, l)$ represents the straight line passing through the centroid of the undistorted beam sections. The axial displacement $u_k(x, z)$ and the transverse displacement $w_k(x, z)$ at point (x, z) of the kth layer, where $k \in (1, N)$, are defined. The kinematic description for the kth layer is derived from the vertical displacement $w_k(x, z)$ in the z direction and the horizontal displacement $u_k(x, z)$ in the x direction. Consequently, the displacement field takes the following form:

$$\begin{aligned} u_k(x, z) &= u_0(x) - z\ [w_0'(x) - \psi(x)] + \phi_k(z)\ \psi(x) \\ w_k(x, z) &= w_0(x) \end{aligned} \tag{3.1}$$

where $w_0'(x, z) = dw_0/dx$. The vertical displacement $w_0(x, z)$ is the same for all the layers, and the horizontal displacement comprise three terms: $u_0(x)$ being the displacement of the sectional centeroid; $-z[w_0'(x) - \psi(x)]$, is analogous to axial displacement of Timoshenko's beam when $\psi(x)$ is related to the average shear angle; $\phi(z)\psi(x)$ is the zigzag displacement, where $\phi(x)$ is the zigzag function and $\psi(x)$ implies the amplitude of the zigzag function.

The proposed zigzag function is similar to the one in RZT and is a continous piecewise linear, and has the following form over the layer k

$$\phi_k = \frac{\bar{\phi}_k + \bar{\phi}_{k-1}}{2} + \frac{\bar{\phi}_k - \bar{\phi}_{k-1}}{2}\,\xi\,, \tag{3.2}$$

where the non dimensional coordinate of the layer k is $\xi_k = \dfrac{2(z - z_{k-1})}{h_k} - 1$, being $\bar{\phi}_k$ and $\bar{\phi}_{k-1}$ the values at the interfaces with the neighboring layers $k+1$ and $k-1$, as per Figure 3.1. Consequently, the gradient is constant in each layer, i.e.,

$$\alpha_k = \frac{d\phi_k}{dz} = \frac{\bar{\phi}_k - \bar{\phi}_{k-1}}{h_k}\,. \tag{3.3}$$

From (3.1), the axial strain $\varepsilon_x^k(x,z)$ and the shear strain $\gamma_{xz}^k(x,z)$ in the k-th layer, take the form

$$\varepsilon_x^k(x,z) = \frac{\partial}{\partial x}u_k(x,z) = u_0'(x) - zw_0''(x) + [z + \phi(z)]\,\psi'(x), \tag{3.4a}$$

$$\gamma_{xz}^k(x,z) = w_0'(x) + \frac{\partial}{\partial z}u_k(x,z) = (1 + \alpha_k)\psi(x). \tag{3.4b}$$

Taking into consideration that the zigzag function shall vanish at the top and bottom surfaces of the beam cross-section, one can write:

$$b\int_{-h/2}^{h/2} \frac{d\phi_k}{dz}\,dz = b\int_{-h/2}^{h/2} \alpha_k\,dz = \int_A \alpha_k\,dA = 0\,. \tag{3.5}$$

Therefore, integrating (3.60b) over the cross section and using (3.5), one has

$$\psi(x) = \frac{1}{A}\int_A \gamma_{xz}^k(x)\,dA\,. \tag{3.6}$$

This confirms that $\psi(x)$ indeed represents the weighted average transverse shear strain of the cross section.

3.2.3 Computation of the Zigzag Function.

Following the RZT [14], [15], the value of the zigzag function at the top and bottom surfaces of the laminate should vanish, i.e., $\bar{\phi}_0 = 0$ and $\bar{\phi}_N = 0$ in (3.2). Additionally, the gradient of the zigzag function α_k for $k = 1 \dots N$ is obtained considering the continuity of shear stress at the interface of various layers, as known from the elasticity solution. However, in this model, the assumption is that the glass plies are behaving as Euler-Bernoulli beams with negligible shear strain; consequently, the shear stress in glass layers cannot be calculated from shear strain. The formal derivation of the gradient relies on the assumption that the shear modulus of glass plies has a finite value; then eventually, one can calculate the limit when this modulus goes to infinity.

Let G_k represent the shear modulus of the k-th layer. From (3.60b) the corresponding shear stress τ_{xz}^k reads

$$\tau_{xz}^k = G_k \gamma_{xz}^k = G_k \left[1 + \alpha_k\right] \psi(x) \,. \tag{3.7}$$

The interfacial continuity of shear stress at each cross section x requires that

$$G_k \left[1 + \alpha_k\right] = G_{k+1} \left[1 + \alpha_{k+1}\right] = \text{const.} = G \,, \quad \text{for}\, k = 1 \dots N-1 \,. \tag{3.8}$$

This implies that

$$\alpha_k = \frac{G}{G_k} - 1 \,. \tag{3.9}$$

Substituting in (3.5), one finds

$$G = \frac{A}{\displaystyle\int_A \frac{1}{G_k} dA} = \frac{h}{\displaystyle\sum_{k=1}^{N} \frac{h_k}{G_k}} \,. \tag{3.10}$$

For a glass ply, identified by k odd. Let $G_k \to \infty$ so that, from (3.9), $\alpha_k \to -1$. Moreover in (3.10) only the terms with k even survive.

Therefore, from (3.10), one can write

$$\alpha_k = \begin{cases} \dfrac{G}{G_k} - 1 = \dfrac{h/G_k}{\displaystyle\sum_{i\,\text{even}} h_i/G_i} & \text{for}\, k\, \text{even}\, (G_k \text{ finite}) \,, \\ \qquad -1 & \text{for}\, k\, \text{odd}\, (G_k \to \infty) \,. \end{cases} \tag{3.11}$$

Using (3.3) in (3.5), the following recursion relation holds:

$$\bar{\phi}_k = \sum_{i=1}^{k} h_i \alpha_i \quad \text{with} \quad \bar{\phi}_0 = 0 \text{ and } \bar{\phi}_N = 0\,. \tag{3.12}$$

The zigzag function can also be conveniently expressed as a function of the local coordinate $\xi \in (-1, 1)$, defined in (3.2), as

$$\phi_k = \frac{h_k \alpha_k}{2}(\xi_k - 1) + \sum_{i=1}^{k} h^i \alpha^i\,. \tag{3.13}$$

A noteworthy consequence is the expression for the term $[z + \phi_k(z)]$, which appears in the axial strain $\varepsilon_x^k(x, z)$ which reads:

$$z + \phi_k = \begin{cases} z + \alpha_k(z - z_{k-1}) + \bar{\phi}_{k-1} & \text{for } k \text{ even}\,, \\ z_{k-1} + \bar{\phi}_{k-1} = \text{const.} = c_{k-1} & \text{for } k \text{ odd.} \end{cases} \tag{3.14}$$

Observe that the contribution of $\psi(x)$ to the axial displacement, as per equation (3.1), is constant in the glass layers (with k odd) and equal to c_{k-1}. This constant depends on the cross-sectional geometry and shear properties of the interlayers.

3.2.4 Strain Energy

The contributions to the strain energy consist of the bending contributions from the glass layers when k is odd and the shear contributions from the interlayers when k is even. The bending energy of the interlayers is neglected by taking $E_k = 0$ when k is even, while the shear energy of the glass plies is considered to be negligible. Hence the strain energy function reads:

$$\begin{aligned} U = &\sum_{k\text{ odd}} \int_{V_k} \frac{1}{2} E_k \left[u_0'(x) - z\, w_0''(x) + c_{k-1}\, \psi'(x)\right]^2 dV_k \\ &+ \sum_{k\text{ even}} \int_{V_k} \frac{1}{2} G_k \left[(1 + \alpha_k)\, \psi(x)\right]^2 dV_k\,, \end{aligned} \tag{3.15}$$

where V_k is the volume of the k-th layer.

If one considers a multimaterial cross-section where, in general, the elastic moduli are not the same for the glass layers and polymer layers, the procedure of choosing a value for the elastic modulus as a reference and defining other values as a ratio to this reference is a common practice. Therefore, set

$$\beta_k = \frac{E_k}{E_r} \text{ for } k \text{ odd}\,, \quad \beta_k = \frac{G_k}{G_r} \text{ for } k \text{ even}\,. \tag{3.16}$$

where E_r and G_r are the reference Young's modulus and shear modulus, respectively, for the odd and even layers. The shear contribution to the strain energy (3.15), provided by the interlayers, is given by

$$\begin{aligned} &\sum_{k \text{ even}} \int_{V_k} \frac{1}{2}\, G_r\, \beta_k\, \left[(1+\alpha_k)\, \psi(x)\right]^2 dV \\ &= \frac{1}{2}\, G_r\, b \sum_{k \text{ even}} \left[(1+\alpha_k)^2\, h_k\, \beta_k\right] \int_0^l \psi^2(x)\, dx = \frac{1}{2}\, G_r\, A^* \int_0^l \psi^2(x)\, dx\,, \end{aligned} \tag{3.17}$$

where

$$A^* = b \sum_{k \text{ even}} \left[(1+\alpha_k)^2\, h_k\, \beta_k\right]\,. \tag{3.18}$$

The part of the energy associated with the normal strains takes the form:

$$\begin{aligned} &\sum_{k \text{ odd}} \int_{V_k} \frac{1}{2}\, E_r\, \beta_k \left[u_0'(x) - z\, w_0''(x) + c_{k-1}\, \psi'(x)\right]^2 dV \\ &= \frac{1}{2}\, E_r \int_0^l \left[\sum_{k \text{ odd}} \beta_k \int_{A_k} \left(u_0'(x) - z\, w_0''(x) + c_{k-1}\, \psi'(x)\right)^2 dA\right] dx \\ &= \frac{1}{2}\, E_r \int_0^l [A_g\, u_0'(x)^2 + I_g\, w_0''(x)^2 + I_{g_1}\, \psi'(x)^2 - 2Q_g\, u_0'(x)\, w_0''(x) \\ &\qquad\qquad - 2I_{g_2}\, \psi'(x)\, w_0''(x) + 2S_g\, u_0'(x)\, \psi'(x)]\, dx\,, \end{aligned} \tag{3.19}$$

with

$$\begin{aligned} &A_g = \sum_{k \text{ odd}} \beta_k\, b\, h_k\,,\ I_g = \sum_{k \text{ odd}} \beta_k \int_{A_k} z^2\, dA\,,\ I_{g_1} = \sum_{k \text{ odd}} \beta_k\,, \int_{A_k} c_{k-1}^2\, dA \\ &Q_g = \sum_{k \text{ odd}} \beta_k \int_{A_k} z\, dA\,,\ I_{g_2} = \sum_{k \text{ odd}} \beta_k \int_{A_k} z\, c_{k-1}\, dA\,,\ S_g = \sum_{k \text{ odd}} \beta_k \int_{A_k} c_{k-1}\, dA\,. \end{aligned} \tag{3.20}$$

The section properties A_g, I_g, I_{g_1}, Q_g, I_{g_2}, and S_g reduce to area, moments of inertia, and first moments of area when the cross-section is homogeneous ($\beta_k = 1$). In a laminated package, these properties correspond to the geometric characteristics of the section, homogenized with respect to the reference materials, as is classically done in layered composites.

In conclusion, the strain energy can be expressed as:

$$\begin{aligned} U =& \frac{1}{2}\, E_r \int_0^l [A_g\, u_0'(x)^2 + I_g\, w_0''(x)^2 + I_{g_1}\, \psi'(x)^2 - 2Q_g\, u_0'(x)\, w_0''(x) \\ & - 2I_{g_2}\, \psi'(x)\, w_0''(x) + 2S_g\, u_0'(x)\, \psi'(x)]dx + \frac{1}{2}\, G_r\, A^* \int_0^l \psi^2(x)\, dx\,. \end{aligned} \tag{3.21}$$

Hereafter, is the analytic solution of the corresponding Euler-Lagrange equations. The variational approach will also be used for the FEM implementation.

3.2.5 Analytic Solution

The simple case of a straight, simply supported laminated-glass beam, $x \in (0, l)$, is solved explicitly. The cross-section is composed of an arbitrary number N of layers, and the beam is loaded by a transverse distributed load $q(x)$. Generally, a solution can be obtained for other configurations of statically determinate beams, where the bending moment is calculated from static equilibrium. In the case of statically indeterminate beams, the equations can still be solved explicitly, but the numerical approach implemented in the next section is much more convenient.

From (3.21), considering the work of the external loads, the total energy functional becomes

$$\begin{aligned} \mathcal{E} =& \frac{1}{2}\, E_r \int_0^l [A_g\, u_0'(x)^2 + I_g\, w_0''(x)^2 + I_{g_1}\, \psi'(x)^2 \\ & - 2Q_g\, u_0'(x)\, w_0''(x) - 2I_{g_2}\, \psi'(x)\, w_0''(x) + 2S_g\, u_0'(x)\, \psi'(x)]dx \\ & + \frac{1}{2}\, G_r\, A^* \int_0^l \psi^2(x)\, dx - \int_0^l q(x)\, w_0(x)\, dx\,. \end{aligned} \tag{3.22}$$

The first variation with respect to u_0, provides the field equation and boundary conditions

$$-E_r\ [A_g\, u_0''(x) - Q_g\, w_0'''(x) + S_g\, \psi''(x)] = 0\,, \quad x \in (0, l)\,, \tag{3.23a}$$

$$[E_r\,(\, A_g\, u_0'(x) - Q_g\, w_0''(x) + S_g\, \psi'(x))\ \ \delta u_0(x)]_0^l = 0\,. \tag{3.23b}$$

The first variation in w_0 gives

$$E_r \left[I_g\, w_0''(x) - I_{g_2}\, \psi'(x) - Q_g\, u_0'(x)\right]'' - q(x) = 0\,, \quad x \in (0, l)\,, \tag{3.24a}$$

$$\left[E_r \left(I_g\, w_0''(x) - I_{g_2}\, \psi'(x) - Q_g\, u_0'(x)\right) \delta w_0'(x)\right]_0^l = 0\,, \tag{3.24b}$$

$$\left[-E_r \left(I_g\, w_0''(x) - I_{g_2}\, \psi'(x) - Q_g\, u_0'(x)\right)' \delta w_0(x)\right]_0^l = 0\,. \tag{3.24c}$$

Finally, the first variation in ψ implies

$$E_r \left[I_{g_2}\, w_0''(x) - I_{g_1}\, \psi'(x) - S_g\, u_0'(x)\right]' + G_r\, A^*\, \psi(x) = 0\,, \quad x \in (0, l)\,, \tag{3.25a}$$

$$\left[E_r(S_g\, u_0'(x) - I_{g_2}\, w_0''(x) + I_{g_1}\, \psi'(x))\, \delta\psi(x)\right]_0^l = 0\,. \tag{3.25b}$$

Equation (3.23) show that $E_r\,[A_g\, u_0'(x) - Q_g\, w_0''(x) + S_g\, \psi'(x)]$ represents the axial force in the beam. Equations (3.24) show that $E_r\,[I_g\, w_0''(x) - I_{g_2}\, \psi'(x) - Q_g\, u_0'(x)]$ is the bending moment in the beam, and its derivative is associated with the shear force. The amplitude of the zigzag function $\psi(x)$ incorporates the relative slip between glass plies, which occurs due to the compliance of the interlayer. Equation (3.25a) represents the equilibrium of the interlayer. A slipping constraint can be imposed by setting $\psi(x) = 0$ at either end of the beam, $x = 0$ or $x = l$. This can be achieved by gluing a rigid block of the same thickness as the interlayer, as discussed in [47]. On the same note, if slipping is allowed at the beam ends, the variation $\delta\psi(x)$ at the boundary can be non-zero, and the force $E_r(I_{g_1}\, \psi'(x) - I_{g_2}\, w_0''(x) - S_g\, u_0'(x))$ in equation (3.25b) shall vanish.

Generally, the system of equations (3.23a), (3.24a), and (3.25a) requires eight boundary conditions to be solved explicitly, considering that this system is fourth order in $w_0(x)$ and second order in both $u_0(x)$ and $\psi(x)$. In fact, although (3.24a) apparently shows a higher degree of differentiation in both $u_0(x)$ and $\psi(x)$, substitution from the other equations and manipulation can eliminate this dependence.

For the case at hand, the geometric boundary conditions are $w_0(x) = 0$ at $x = 0$ and $x = l$. When the value of $\psi(x)$ is not prescribed at the supports, the remaining boundary conditions can be derived from (3.23b), (3.24b), and (3.25b), and can be stated as

$$\begin{bmatrix} A_g & -Q_g & S_g \\ -Q_g & I_g & -I_{g_2} \\ S_g & -I_{g_2} & I_{g_1} \end{bmatrix} \begin{Bmatrix} u_0'(x) \\ w_0''(x) \\ \psi'(x) \end{Bmatrix} = \begin{Bmatrix} 0 \\ 0 \\ 0 \end{Bmatrix}\,, \quad \text{at } x = 0 \text{ and } x = l\,. \tag{3.26}$$

From the expression (3.20), one can directly verify that the determinant of the matrix is not zero. Hence, the boundary conditions $w_0''(x) = 0$, $\psi'(x) = 0$, and $u_0'(x) = 0$ hold at $x = 0$ and $x = l$. If, on the other hand, one assumes that the value of $\psi(x) = 0$ is assigned at the beam ends $x = 0$ or $x = l$, one must consider only the conditions that correspond to the first two equations of (3.26).

The equations can be easily solved when the moment equation (3.24a) can be integrated directly. This is certainly possible when the bending moment in the beam is known, as in the problem at hand. Here, the calculations are made explicit for the case of a uniformly distributed load $q(x) = p$.

Since the beam is simply supported at the ends, (3.24b) can be satisfied if, at $x = 0$ and $x = l$, $E_r\,(I_g\,w_0''(x) - I_{g_2}\,\psi'(x) - Q_g\,u_0'(x)) = 0$. This is the moment boundary condition at the simple supports, where $M(x) = 0$ at $x = 0$ and $x = l$. Consequently, (3.24a) can be integrated for $q(x) = p$ and provides

$$E_r\,(I_g\,w_0''(x) - Q_g\,u_0'(x) - I_{g_2}\,\psi'(x)) - \frac{p}{2}\,x(x-l) = 0 \quad x \in (0,l)\,. \tag{3.27}$$

Isolating $w_0''(x)$ from (3.27), and substituting it in (3.23a), and (3.25a), one obtain the system of differential equations

$$w_0''(x) = \frac{I_{g_2}}{I_g}\,\psi'(x) + \frac{Q_g}{I_g}\,u_0'(x) + \frac{p}{2\,E_r\,I_g}(x^2 - x\,l)\,, \tag{3.28a}$$

$$E_r\left(\frac{Q_g^2}{I_g} - A_g\right)u_0''(x) + E_r\left(\frac{I_{g_2}\,Q_g}{I_g} - S_g\right)\psi''(x) + \frac{Q_g\,p}{I_g}\left(x - \frac{l}{2}\right) = 0\,, \tag{3.28b}$$

$$E_r\left(\frac{I_{g_2}^2}{I_g} - I_{g_1}\right)\psi''(x) + E_r\left(\frac{I_{g_2}\,Q_g}{I_g} - S_g\right)u_0''(x) + As\,G_r\,\psi(x) + \frac{I_{g_2}\,p}{I_g}\left(x - \frac{l}{2}\right) = 0\,. \tag{3.28c}$$

One can substitute $u_0''(x)$ from (3.28b) into (3.28c), and find a second order differential equation in the sole $\psi(x)$, which can be solved because the boundary conditions are assigned. In fact, in the case in which the slip is constrained at the ends, one has $\psi(0) = \psi(l) = 0$. If this is not the case, one has from (3.26) that $\psi'(0) = \psi'(l) = 0$. Then, the so found $\psi(x)$ is substituted in (3.28b), to obtain a second order differential equation in $u_0''(x)$, which can be integrated. Finally, the so obtained expressions of $\psi(x)$ and $u_0(x)$ are used in (3.28a), to define the conclusive differential equation for $w_0(x)$, which is solved under the conditions $w_0(0) = w_0(l) = 0$.

The *layered limit* is obtained in the case $G_r = 0$. Thus, from (3.25a), one obtains

$$\psi''(x) = \frac{I_{g_2}}{I_{g_1}}\,w_0'''(x) - \frac{S_g}{I_{g_1}}u_0''(x)\,. \tag{3.29}$$

Substituting in (3.24a), one finds

$$E_r\left(I_g - \frac{I_{g2}^2}{I_{g1}}\right)w_0''''(x) - E_r\left(Q_g - \frac{I_{g2}\,S_g}{I_{g1}}\right)u_0'''(x) - q(x) = 0\,. \tag{3.30}$$

Recalling (3.20), it is readily proved that $\left(Q_g - \dfrac{I_{g2}\,S_g}{I_{g1}}\right) = 0$. This confirms that, in the layered limit, the axial displacement $u_0(x)$ is decoupled from transverse displacement $w_0(x)$, because each layer deform independently from the other layers. The bending equilibrium thus reduces to

$$E_r\left(I_g - \frac{I_{g2}^2}{I_{g1}}\right) w_0''''(x) - q(x) = 0\,. \tag{3.31}$$

Observe, from (3.20), that when all the plies are made of the same glass ($\beta_k = 1$), one has

$$I_g - \frac{I_{g_2}^2}{I_{g_1}} = I_g - \sum_{k \text{ odd}} A_k\, \bar{z_k}^2 = I_l\,, \tag{3.32}$$

where $\bar{z_k} = \frac{1}{2}(z_{k+1} + z_k)$ is the distance, measured along the z axis of Figure 3.1, of the centroid of the k-th glass layer. Therefore, I_l is the layered moment of inertia, i.e., the sum of the centroidal moments of inertia of the glass plies.

The monolithic limit is related to the value of the interlayer's shear modulus and theoretically occurs when $G_p \to +\infty$. This can be understood by observing equation (3.22), which implies that $\psi(x) = 0$, $x \in (0, l)$; otherwise, the energy function would become unbounded. The actual implication of this observation is that the value of the zigzag function goes to zero when the rigid interlayer prevents the relative sliding of the glass plies. Equation (3.20) shows that I_g is the moment of inertia of the cross-section of the glass plies, spaced by the thickness of the interlayers. This is the cross-sectional inertia to be considered in the monolithic limit [32].

It should also be remarked, from (3.20), that $Q_g = 0$ when, for example, the cross-section of the laminate is symmetric with respect to the y axis of Figure 3.1. In this case, it can be proven that the axial strain is zero, and (3.27) reduces to the classical equilibrium equation in bending. When $Q_g \neq 0$, equation (3.27) indicates that the axial strain is generally not null; this is because the x axis is not centroidal for the homogenized cross-section. In other words, the neutral axis of the cross-section does not coincide with the y axis.

In the next section, the numerical implementation of the model is presented, for which the cases analytically solved here will be used as benchmark problems.

3.2.6 Finite Element Implementation

The standard procedure in finite elements is based on the interpolation of the displacement field and substituting the corresponding strains into the energy equation (3.21). The integration of strain expressions over the cross-section gives the work conjugates, which are in this case the axial force N, the bending moment M_{w0}, the shear-induced moment M_ψ, and the shear force Q_ψ. These are, respectively, work conjugates with $\delta u_0'(x)$, $\delta w_0''(x)$, $\delta\psi'(x)$, and $\delta\psi(x)$. The generalized constitutive relationships read

$$\boldsymbol{\sigma}_\varepsilon = \begin{Bmatrix} N \\ M_{w_0} \\ M_\psi \end{Bmatrix} = \mathbf{D}_\varepsilon \boldsymbol{\varepsilon}_\varepsilon \quad , \ \sigma_t = Q_\psi = D_t \varepsilon_t \, , \tag{3.33}$$

where, from (3.21),

$$\mathbf{D}_\varepsilon = E_r \begin{bmatrix} A_g & -Q_g & S_g \\ -Q_g & I_g & -I_{g2} \\ S_g & -I_{g_2} & I_{g_1} \end{bmatrix} \quad , \ D_t = G_r \, A^* \, , \tag{3.34}$$

and

$$\boldsymbol{\varepsilon}_\varepsilon = \begin{Bmatrix} u_0'(x) \\ w_0''(x) \\ \psi'(x) \end{Bmatrix} \quad , \quad \varepsilon_t = \psi(x) \; . \tag{3.35}$$

Considering that the first variation of (3.21) is of fourth order with respect to $w_0(x)$ and of second order with respect to $u_0(x)$ and $\psi(x)$, the essential boundary conditions are $u_0(x)$, $w_0(x)$, $w_0'(x)$, and $\psi(x)$ at the first and second nodes, $x = x_i$ and $x = x_j$, respectively. These indicate the nodal degrees of freedom for the finite element. Consequently, the two-node *Refined Zigzag* (BRZ) beam FE has eight degrees of freedom, $\mathbf{a}_i^{(e)}$ and $\mathbf{a}_j^{(e)}$, at nodes i and j, as schematically indicated in Figure 3.2.

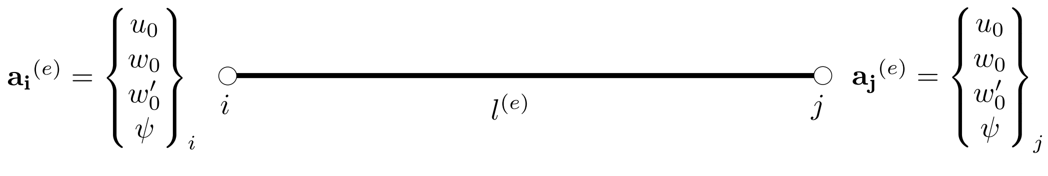

Figure 3.2: BRZ beam finite element of length $l^{(e)}$, with indication of the degrees of freedom $\mathbf{a}_i^{(e)}$ and $\mathbf{a}_j^{(e)}$ at nodes i and j, respectively.

The continuity requirements for the interpolation of the unknowns are C^1 for the deflection $w_0(x)$ and C^0 for the axial displacement $u_0(x)$ and the average shear angle $\psi(x)$. A cubic Hermite interpolation is chosen for $w_0(x)$, whereas $u_0(x)$ and $\psi(x)$ are described by a standard linear approximation. The shape functions are represented in terms of the local coordinate $\xi \in (-1, 1)$ in such a way that, denoting x_i and x_j as the nodal coordinates of the beam element of length $l^{(e)}$,

$$\xi = \frac{2}{l^{(e)}}\,(x - \frac{x_i + x_j}{2})\,, \quad \frac{\partial x}{\partial \xi} = \frac{l^{(e)}}{2}\,, \quad x \in (x_i, x_j)\,. \tag{3.36}$$

Hence, the linear and Hermite interpolations can be written as

$$N_1 = \frac{1}{2}(1-\xi)\,, \quad N_2 = \frac{1}{2}(1+\xi)\,, \tag{3.37a}$$

$$\begin{aligned} \bar{N}_1 &= \frac{1}{4}\,(2 - 3\xi + \xi^3)\,, \quad \bar{N}_2 = \frac{1}{4}\,(\xi^3 - \xi^2 - \xi + 1)\,, \\ \bar{N}_3 &= \frac{1}{4}\,(2 + 3\xi - \xi^3)\,, \quad \bar{N}_4 = \frac{1}{4}\,(\xi^3 + \xi^2 - \xi - 1)\,. \end{aligned} \tag{3.37b}$$

Consequently, one can approximate the displacement field as

$$\mathbf{u} = \begin{Bmatrix} u_0(x) \\ w_0(x) \\ \psi(x) \end{Bmatrix} = \mathbf{N}_i \mathbf{a}_i^{(e)} + \mathbf{N}_j \mathbf{a}_j^{(e)} = \begin{bmatrix} \mathbf{N}_i \ , \ \mathbf{N}_j \end{bmatrix} \begin{Bmatrix} \mathbf{a}_i^{(e)} \\ \mathbf{a}_j^{(e)} \end{Bmatrix} = \mathbf{N}\ \mathbf{a}^{(e)}\,, \tag{3.38}$$

where

$$\mathbf{N}_i = \begin{bmatrix} N_1 & 0 & 0 & 0 \\ 0 & \bar{N}_1 & \bar{N}_2 & 0 \\ 0 & 0 & 0 & N_1 \end{bmatrix} \quad , \mathbf{N}_j = \begin{bmatrix} N_2 & 0 & 0 & 0 \\ 0 & \bar{N}_3 & \bar{N}_4 & 0 \\ 0 & 0 & 0 & N_2 \end{bmatrix}\,. \tag{3.39}$$

It follows from (3.35) that

$$\boldsymbol{\varepsilon}_\varepsilon = \begin{bmatrix} \mathbf{B}_i \ , \ \mathbf{B}_j \end{bmatrix} \begin{Bmatrix} \mathbf{a}_i^{(e)} \\ \mathbf{a}_j^{(e)} \end{Bmatrix} = \mathbf{B}\ \mathbf{a}^{(e)}\,, \quad \varepsilon_t = \psi(x) = \mathbf{N}_\psi^T \mathbf{a}^{(e)}\,, \tag{3.40}$$

with

$$\mathbf{B}_i = \begin{bmatrix} \frac{dN_1}{dx} & 0 & 0 & 0 \\ 0 & \frac{d^2\bar{N}_1}{dx^2} & \frac{d^2\bar{N}_2}{dx^2} & 0 \\ 0 & 0 & 0 & \frac{dN_1}{dx} \end{bmatrix}, \quad \mathbf{B}_j = \begin{bmatrix} \frac{dN_2}{dx} & 0 & 0 & 0 \\ 0 & \frac{d^2\bar{N}_3}{dx^2} & \frac{d^2\bar{N}_4}{dx^2} & 0 \\ 0 & 0 & 0 & \frac{dN_2}{dx} \end{bmatrix}, \tag{3.41a}$$

$$\mathbf{N}_\psi^T = \begin{bmatrix} 0 & 0 & 0 & N_1 & 0 & 0 & 0 & N_2 \end{bmatrix} \begin{Bmatrix} \mathbf{a}_i \\ \mathbf{a}_j \end{Bmatrix}\,. \tag{3.41b}$$

The strain energy U of (3.21) and the work W of the external forces can be rewritten in matrix form. If the element is subjected to a distributed transverse load $q(x)$, recalling (3.34) and (3.35), the total energy reads

$$\mathcal{E} = U - W = \frac{1}{2}\int_{x_i}^{x_j} \mathbf{D}_\varepsilon\, \boldsymbol{\varepsilon}_\varepsilon^2 + D_t\, \varepsilon_t^2\, dx - \int_{x_i}^{x_j} q(x)\, w_0(x)\, dx\,. \tag{3.42}$$

From (3.40) and (3.41), the stiffness matrix at the element level takes the form

$$\mathbf{K} = \mathbf{K}_p + \mathbf{K}_t\,, \tag{3.43}$$

Where

$$\mathbf{K}_p = \begin{bmatrix} \mathbf{K}_{p_{ii}} & \mathbf{K}_{p_{ij}} \\ \mathbf{K}_{p_{ji}} & \mathbf{K}_{p_{jj}} \end{bmatrix}\,, \quad \mathbf{K}_{p_{hk}} = \int_{-1}^{+1} \mathbf{B}_h^T\, \mathbf{D}_\varepsilon\, \mathbf{B}_k\, \frac{l^{(e)}}{2}\, d\xi \quad h,k = i,j\,, \tag{3.44}$$

$$\mathbf{K}_t = \int_{-1}^{+1} \mathbf{N}_\psi^T\, D_t\, \mathbf{N}_\psi\, \frac{l^{(e)}}{2}\, d\xi\,. \tag{3.45}$$

The external work can be expressed in terms of shape functions as follows

$$W = \int_{-1}^{+1} q(\xi)\, \mathbf{N}_w^T\, \mathbf{a}^{(e)}\, \frac{l^{(e)}}{2}\, d\xi \, = \mathbf{r_q}^T\, \mathbf{a}^{(e)}\,, \tag{3.46}$$

where

$$\mathbf{N}_w^T = \begin{bmatrix} 0 & \bar{N}_1 & \bar{N}_2 & 0 & 0 & \bar{N}_3 & \bar{N}_4 & 0 \end{bmatrix}\,. \tag{3.47}$$

Consequently the energy expression reduces to

$$\mathcal{E} = \frac{1}{2}\, \mathbf{a}^{(e)^T}\, \mathbf{K}\, \mathbf{a}^{(e)} - \mathbf{r}_q^T\, \mathbf{a}^{(e)} = \mathbf{a}^{(e)^T} \left(\frac{1}{2}\, \mathbf{K}\, \mathbf{a}^{(e)} - \mathbf{r}_q\right)\,. \tag{3.48}$$

The necessary condition associated with minimizers of the potential energy provides the equations

$$\frac{\partial \mathcal{E}}{\partial \mathbf{a}^{(e)}} = \left(\frac{1}{2}\, \mathbf{K}\, \mathbf{a}^{(e)} - \mathbf{r}_q\right) + \frac{1}{2}\mathbf{K}\mathbf{a}^{(e)} = \mathbf{K}\, \mathbf{a}^{(e)} - \mathbf{r}_q = 0\,. \tag{3.49}$$

The stiffness matrix can be integrated either analytically or numerically, There is no need to reduce the integration because the assumed regularity of the shape functions rules out the possibility of shear locking. The assembly of the global stiffness matrix for a given mesh follows the standard procedure.

3.2.7 Examples

Here, the evaluation of the numerical convergence of the proposed finite element. The numerical solution is tested against a benchmark problem that has an analytical solution. Additionally, an example of an asymmetrical composite package is presented.The numerical model is based on several assumptions, including the linear elastic behavior of the materials, homogeneity and isotropy of the laminated layers, and perfect bonding between the layers. Additionally, it is assumed that the loads are applied gradually, corresponding to quasi static loading conditions.

3.2.8 Convergence of the Finite Element

The benchmark problem is that of a simply supported beam with a width of $b = 1000$ mm and a length of $l = 3000$ mm, subjected to a uniformly distributed load per unit length of $q = 2\ N/\text{mm}$. The cross-section is a laminate, symmetric with respect to the y axis of Figure 3.1, composed of $N = 5$ layers: specifically, three plies of glass with a thickness of $h_g = 6\,\text{mm}$ and Young's modulus $E_g = 70$ GPa, bonded by two interlayers of Poly Vinyl Butyral (PVB) with a thickness of $h_t = 0.76\,\text{mm}$, whose shear modulus is assumed to vary within the range $G_p = (10^{-5} - 10^{2})\,\text{MPa}$.

Regarding the boundary conditions, in addition to those corresponding to the simple support, the shear sliding between the glass layers at the beam supports is blocked, so that $\psi(0) = \psi(l) = 0$. For this problem, the analytical solution can be directly found using the procedure outlined in Section 3.2.5. Note that, for the case of a symmetric laminated package, the equations (3.28) are greatly simplified because, from (3.20) $Q_g = 0$ and $S_g = 0$. The numerical models are obtained by considering an increasing number of points for the mesh, with the shear modulus G_p within the prescribed range. The nodal values of the numerical solution were interpolated using the shape functions (3.37), as in [48].

The measure of convergence used here is the maximum relative error, defined as

$$e_r = \frac{|v_a - v_n|}{|v_a|}\,, \tag{3.50}$$

where v_a is the value of interest obtained from the analytic solution, while v_n is the corresponding value obtained with a mesh composed of n elements, with $n \in (3 - 300)$. The convergence is tested for the values of the deflection $w_0(x)$ and the average shear angle $\psi(x)$, while the value of $u_0(x)$ is not important for this example, considering that the section is symmetric.

Figure 3.3 shows that the shear modulus has little to no effect on convergence in terms of deflection. Generally, the convergence is fast, and the maximum error is less than 0.01% when the number of elements exceeds five. Considering the lowest number of elements, $n = 3$, the largest error is observed in correspondence with the lower values of the shear modulus G_p. In contrast, for high values of G_p, the error is considerably lower; for the highest values of G_p, very good convergence is achieved even for the coarsest meshes. This can be attributed to the fact that when the shear modulus is large, the structural response of the beam tends towards the monolithic limit, where $\psi(x) \to 0$. In this limit case, the composite beam behaves like an Euler-Bernoulli beam with a compact cross-section.

The relative sliding of the layers is captured by the average shear angle $\psi(x)$, which also serves as an indicator of the degree of shear coupling between the glass plies through the interlayers.

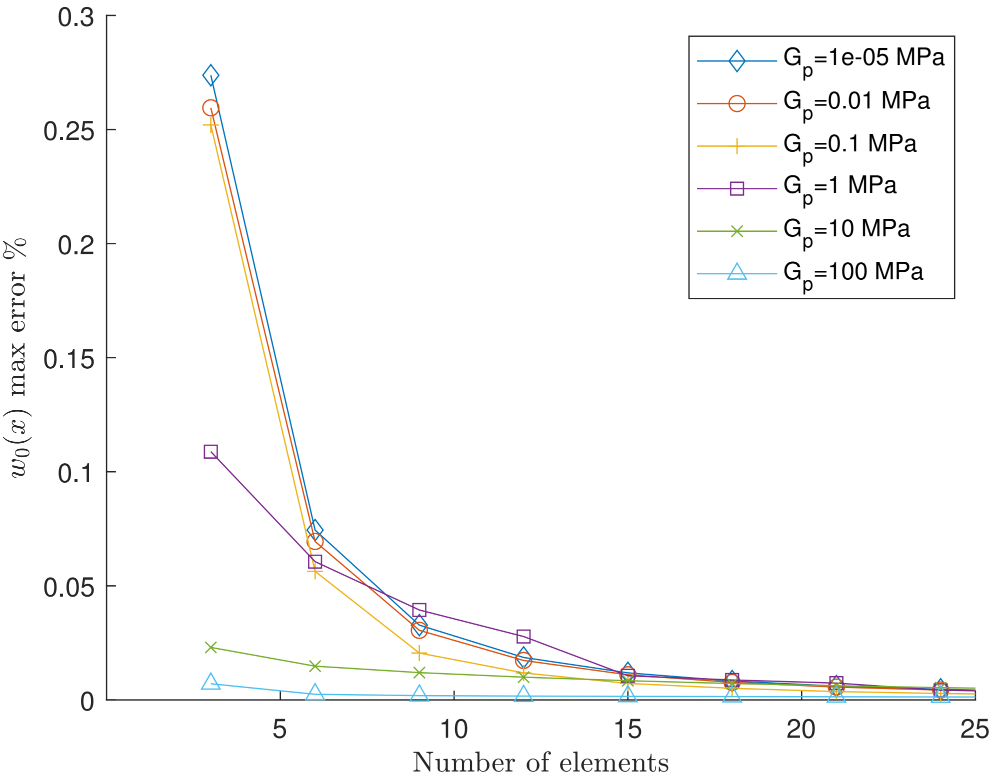

Figure 3.3: Relative error, with respect to the analytical solution, for the maximum deflection $\max_{x\in(0,l)} |w_0(x)|$, as a function of the number of elements used for the discretization, for the various values of the interlayer shear modulus G_p.

Consequently, the deflection is affected by the value of $\psi(x)$, and the state of stress in the cross-section is also dependent on this value. Figure 3.4 demonstrates the dependence of the relative error on the value of the shear modulus and the number of finite elements. As noted, the number of elements required to obtain the smallest error is much higher than in the case of deflection shown in Figure 3.3. Nonetheless, the relative error for the smallest number of elements is acceptable by the standards of numerical approximation.

The dependence of the relative error on the shear modulus is reversed compared to the case of deflection; as shown in Figure 3.4, the higher the shear modulus, the slower the convergence. This can be explained by the fact that when $G_p \to \infty$, the structural response of the cross-section tends to the monolithic limit, and the average shear angle $\psi(x)$ tends to zero. Since, in the expression (3.50) for the relative error, the denominator is close to zero, even a very small variation of the value of interest can yield noteworthy errors. Although the error is relevant in relative terms, its absolute value is limited and has a mild influence on the deflection, as can be deduced from Figure 3.3.

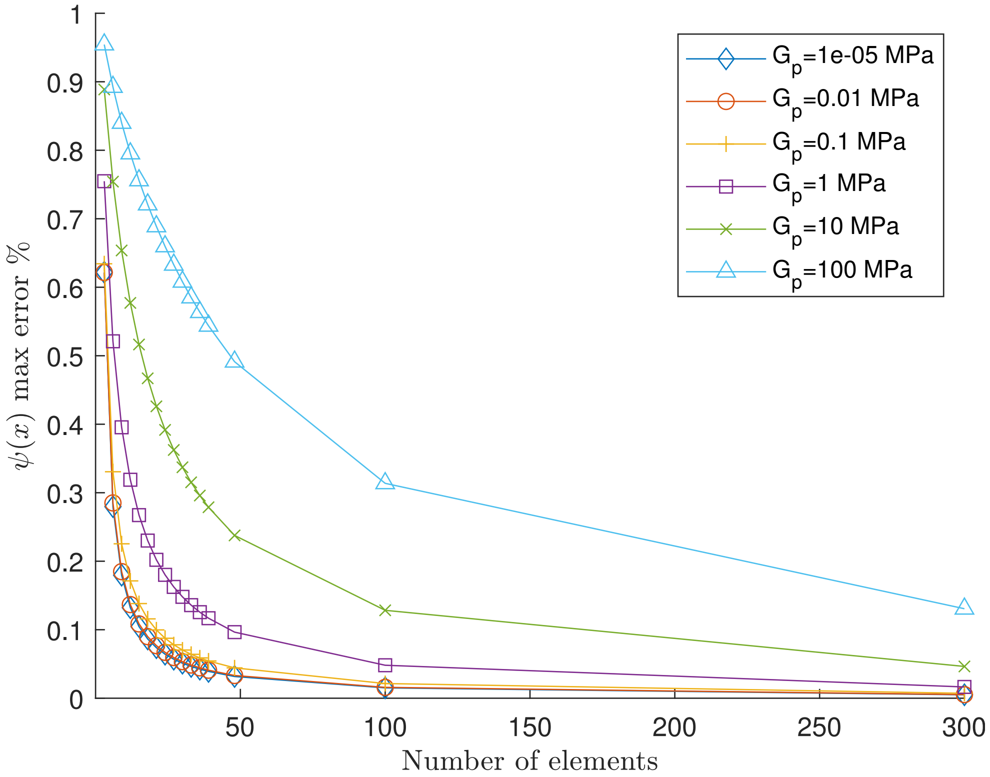

Figure 3.4: Relative error, with respect to the analytical solution, for the maximum value of the average shear angle $\max_{x\in(0,l)} |\psi(x)|$, as a function of the number of elements used for the discretization, for the various values of the interlayer shear modulus G_p.

3.2.9 A Complex Composite Package

Here is a detailed discussion of the structural response of a complex laminated package, for which the composition, with reference to the layer numbering in Figure 3.1, is reported in Table 3.1. In this configuration, glass plies are used in combination with transparent polycarbonate, while the interlayers can be made of either silicone or polymers, with representative shear modulus values of $G_p = (0.1, 1, 100)\,\text{MPa}$. The laminated beam, with a width of $b = 1000\,\text{mm}$ and a span of $l = 5000\,\text{mm}$, is again simply supported at the ends and subjected to a uniformly distributed transverse load per unit length of $q = 1\,\text{N/mm}$.

Regarding the boundary conditions related to the relative slippage between the layers, two possible scenarios are considered: i) blocked slippage at the ends, such that $\psi(x) = 0$ at $x = 0$ and $x = l$; ii) unconstrained slippage at the ends, for which the value of $\psi(x)$ is not prescribed at $x = 0$ and $x = l$. These boundary conditions will be referred to in the graph legends as "$\psi = 0$" or "$\psi \neq 0$", respectively.

Layer	h [mm]	E [GPa]	G [MPa]	Type
7	5	70	-	Glass
6	1.52	-	G_p variable	silicone/polymer
5	10	2	-	poly-carbonate
4	1.52	-	G_p variable	silicone/polymer
3	2	70	-	Glass
2	1.52	-	G_p variable	silicone/polymer
1	2	70	-	Glass

Table 3.1: Composition, with reference to the layer numbering of Figure 3.1, of the laminated package in the proposed example.

This case study demonstrates six combinations of boundary conditions and values of shear modulus G_p. As shown in Figure 3.10(a), three values of the shear modulus are combined with two possible boundary conditions in terms of the average shear angle: $\psi = 0$ and $\psi \neq 0$ at $x = 0$ and $x = l$.

Considering the boundary condition $\psi = 0$ at the beam ends, a notable stiffening of the structure occurs when the shear modulus is low ($G_p = 0.1\,\text{MPa}$). This effect is mild for an intermediate shear modulus ($G_p = 1\,\text{MPa}$), while the boundary condition has almost no effect on the response when the shear modulus is large ($G_p = 100\,\text{MPa}$). This can be attributed to the fact that when the shear modulus is large, the section's behavior tends to the monolithic limit, and the average shear angle $\psi(x)$ approaches zero everywhere, not just at the boundaries.

This phenomenon can be better appreciated from Figure 3.10(b), where the graphs of $\psi(x)$ are reported for the aforementioned combinations of boundary conditions and shear modulus values. For the case when $G_p = 100\,\text{MPa}$, the value of the average shear angle is nearly nil, indicating proximity to the monolithic limit. In the intermediate case with $G_p = 1\,\text{MPa}$, the value of $\psi(x)$ is not close to zero; nonetheless, the difference in response between $\psi = 0$ and $\psi \neq 0$ at the boundaries is negligible.

In the case when the interlayer is soft, i.e., $G_p = 0.1\,\text{MPa}$, it is evident that the boundary condition $\psi = 0$ plays a significant role in stiffening the response. This can be quantitatively appreciated by observing the change in the area under the curves when $\psi = 0$ and when $\psi \neq 0$.

Figure 3.6(a) demonstrates the normal stress σ_{xx} along the beam axis at the intrados of the beam, where the stress is always positive. When the free end condition is applied with $\psi \neq 0$, the stress value aligns with the simple support condition, where $\sigma_{xx} = 0$ at $x = 0$ and $x = l$. The stress value is negatively correlated with the interlayer's shear modulus; as the shear modulus increases, the section's response approaches the monolithic limit, resulting in a higher resistance moment of the cross-section and lower stress values.

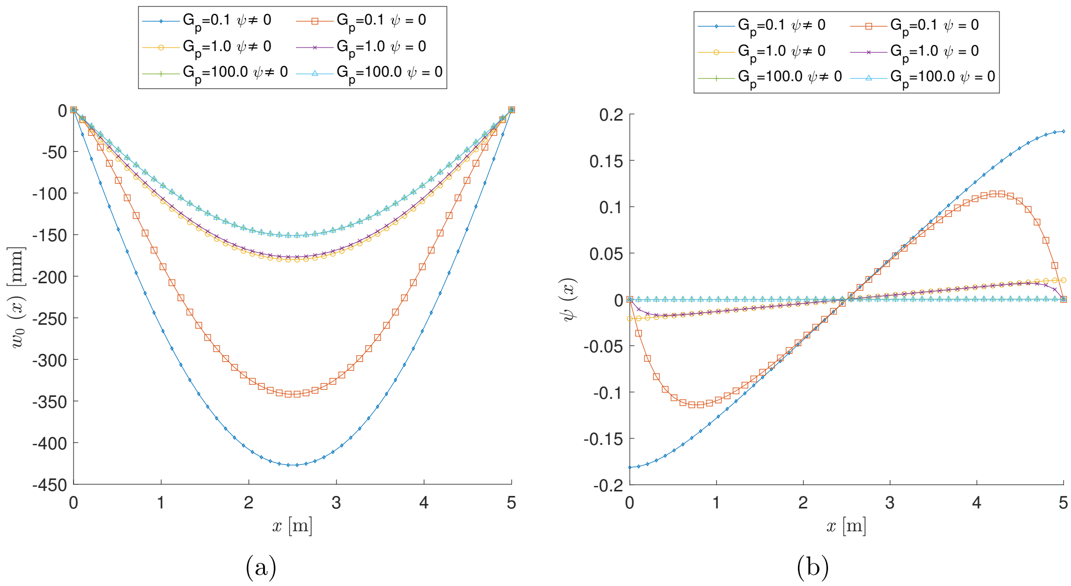

Figure 3.5: (a) Graph of the transversal displacement $w_0(x)$, for $x \in (0, l)$, of beam axis in the six considered cases $Gp = (0.1, 1, 100)$ MPa with constrained ($\psi = 0$) or unconstrained ($\psi \neq 0$) slip of the plies at the ends. (b) Corresponding plots of the average shear angle $\psi(x)$, for $x \in (0, l)$.

When $\psi = 0$, the beam is no longer simply supported, and the axial stress is different from zero. This occurs because this constraint induces a concentrated shear reaction between the glass plies, leading to stress at the beam ends. This effect corresponds with expected results, as discussed in [47]. The impact of the constrained boundary condition $\psi = 0$ is more pronounced for low values of the shear modulus, while it becomes negligible for high values.

These deductions also apply to Figure 3.6(b), which represents the normal stress at the beam's extrados. Notably, the shear constraint $\psi = 0$ has an unexpected effect on the stress at the extrados; this stress remains positive along a portion of the beam near the constraints. This is again due to the internal reactions of the slip constraint, which stresses the ends of the plies. Specifically, referring to the numbering in Table 3.1, one finds that plies 1 and 7 are subjected to tensile end-forces, while plies 3 and 5 are under compression. Indeed, the resultant of the normal forces in the plies must be zero to maintain equilibrium with the external actions.

Graphs of the distribution of normal stress in the thickness direction, corresponding to the z axis of Figure 3.1, are demonstrated in Figure 3.7(a) for $\psi = 0$ and Figure 3.7(b) for $\psi \neq 0$. The stress distribution is piecewise linear in the glass plies, consistent with the zigzag wrapping of the cross-section. The axial stress is null in the interlayers, aligning with the assumptions made in the theory regarding the lack of axial stiffness of the interlayer. The axial stress in layer 5 is significantly lower than that in the glass plies, considering that this layer has a low elastic modulus as per Table 3.1. Qualitatively, there are no obvious differences in the axial stress between the cases with $\psi = 0$ and $\psi \neq 0$; however, the stress values are lower for $\psi = 0$, as the slip constraint at the beam ends encourages behavior closer to the

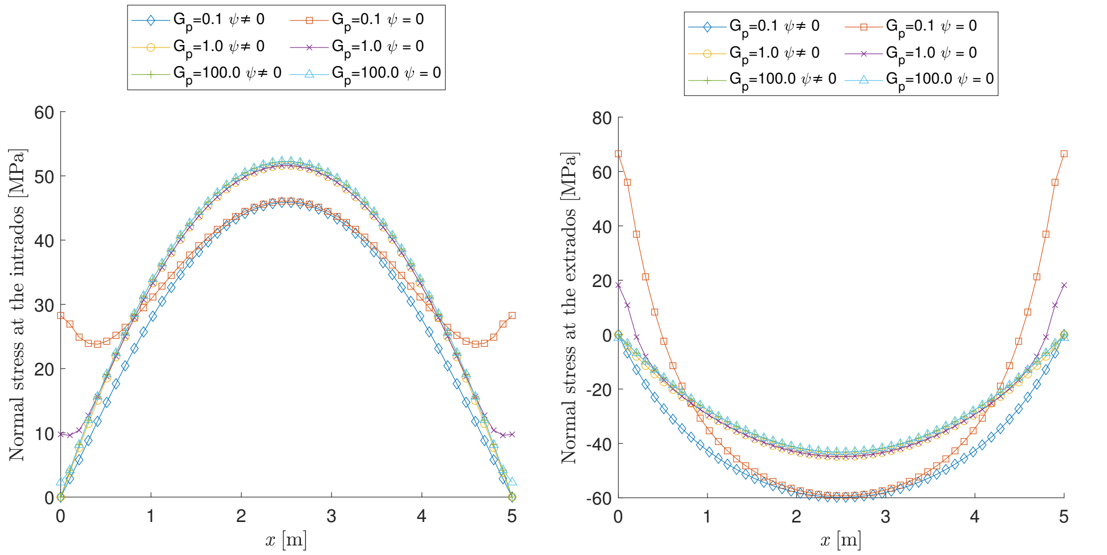

(a) (b)

Figure 3.6: Normal stress at (a) the intrados and (b) the extrados at the various sections $x \in (0, l)$ of the beam, in the six considered cases $Gp = (0.1, 1, 100)$ MPa with constrained $(\psi = 0)$ or unconstrained $(\psi \neq 0)$ slip of the plies at the ends.

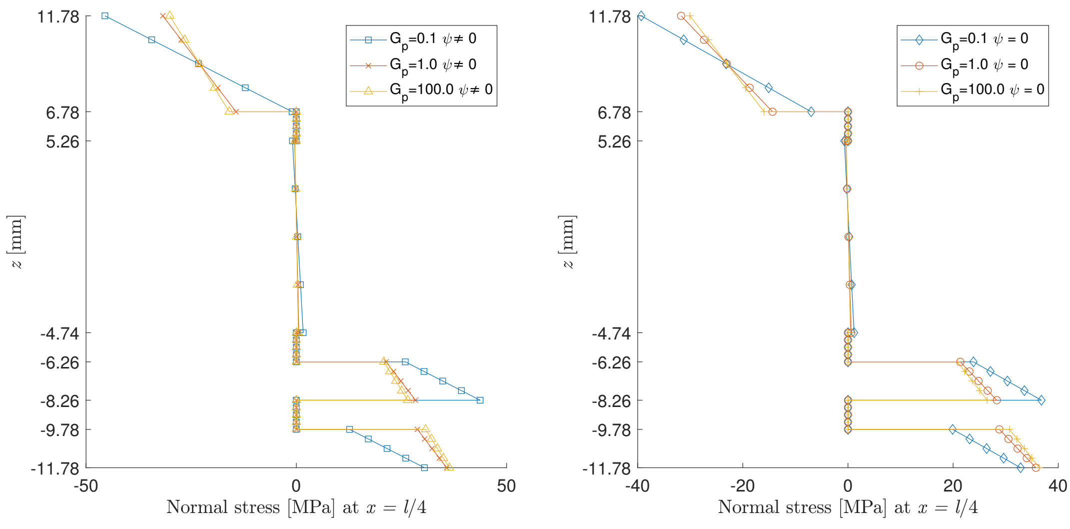

(a) (b)

Figure 3.7: Distribution of the normal stress in the thickness of the beam at the cross section $x = l/4$, for $Gp = (0.1, 1, 100)$ and slip condition (a) $\psi \neq 0$ and (b) $\psi = 0$ at ends.

monolithic limit.

In the following section, the solution of a multilayered laminated glass cantilevered balustrade based on the SZT is presented.

3.3 Analytical Solution and Exact Effective Thickness of Multilayered Laminated Glass Cantilevered Balustrade

The alternation of stiff and soft layers in laminated glass causes a variety of effects on its structural response: (i) the transverse shear strain is primarily constant in the thickness and concentrated in the soft layers, while the stiff layers do not experience any shear strain; (ii) the thickness of the soft layers remains constant under bending or shear deformation, consequently maintaining a constant distance between the stiff layers; (iii) the rotation of the stiff layers is largely identical, while the shear strain in the soft layers is independent. A comprehensive review of mathematical models used to study this specific case of laminated structures was presented in Section 3.2. In this section, the particular case of cantilevered laminated glass, often used as balustrades in prestigious buildings is presented. The deformation of a glass balustrade under design actions (barrier load, wind) is cylindrical, thus the structure can be modeled as a one-dimensional cantilevered beam.

In addition to the aforementioned peculiarities of laminated glass, a major difficulty consists in the assessment of the proper boundary conditions at the clamped edge. The boundary conditions in this case are not only limited to fixed rotation and zero displacement; these conditions should also include the warping of the cross-section, i.e., the relative end displacement of the glass plies. The clamped support for glass balustrades usually consists of inserting the glass plate inside U-profile base shoes for a depth of a few inches [49]. This kind of configuration does not prevent the relative sliding between the glass plies; consequently, the resulting warping of the end cross-section has a major influence on the structural response of the entire cantilever. Methods reported in standards, like the enhanced effective thickness (EET) method, lack the required accuracy to model such conditions, especially because shear coupling through the interlayer is highly variable along the beam axis and strongly influenced by the warping of the end cross-section.

Other methods have been developed to address these limitations; namely, the conjugate beam effective thickness (CBET) [50] was developed as an extension of the EET method. The improved accuracy of the CBET was demonstrated in [50] by comparing paradigmatic examples. Nonetheless, the CBET method is limited to a three-layered cross-section. This section introduces an application of the SPT, where the problem of cantilevered glass balustrades discussed in [50] is solved analytically. This work has been developed by Haydar *et al.* [51] for multilaminates with an arbitrary number and thicknesses of glass and polymer plies. This work is based on the SPT developed in [19], in which the glass (stiff) plies are considered to behave as Euler-Bernoulli beams, while the polymer interlayers (soft) are treated as Timoshenko beams with no bending or axial stiffness.

This work assumes equal rotation of the stiff plies and a constant shear strain through the thickness in the soft layers, which provides fairly simple governing equations that can be solved analytically for the case of a statically determinate beam. The case under consideration has significant practical relevance for the design and verification of laminated glass structures. The theoretical model is based on the SPT [19]; however, the solution of this problem requires variational determination of specific boundary conditions and matching conditions at points where the solution is not regular. The novel aspect of this work also includes the definition of geometric and elastic parameters that provide a tool for understanding the analytic solution. The simplicity of the solution allows it to be implemented in a straightforward `EXCEL™` spreadsheet.

The explicit solution provided here enables the derivation of effective thickness formulas for stress and deflection, although these formulas are not the primary focus here, as the analytic solution contains all the required information necessary for design. Nonetheless, the effective thickness formulas are useful for comparing the current approach with other methods reported in the literature. Due to the limitations inherent in the triple laminate solution [50], the comparison with this solution had to be conducted for a three-layered laminate; nonetheless, the proposed solution is applicable to multilayer laminated packages.

3.3.1 The Model

The laminated package and geometric parameters are presented in Figure 3.1 and Section 3.2.1, while the zigzag function considered for this case is the one introduced in the SZT, as presented in Equations (3.11), (3.12), and (3.13). The geometrical properties of the cross-section are reported in Equation (3.20), where $Q_g = S_g = 0$ when the cross-section is symmetric.

3.3.2 Static Schemes and Governing Equations

As illustrated in Figure 3.8(a), the laminated glass balustrade under consideration consists of vertical glass panels supported at the bottom by a base shoe, typically a U-shaped cross-section channel made of aluminum. The portion of the glass ply inside the channel varies from 2% to 10% of the cantilever's free length.

The cantilever is usually subjected to the barrier load, a distributed force applied at the top of the cantilever, as well as the wind load, which is a distributed pressure uniformly acting over the exposed area. As shown in Figure 3.8(b), due to the nature of the support, the contact between the glass and the U-shaped support can be considered point-wise. Generally, this constraint does not prevent the warping of the end cross-section.

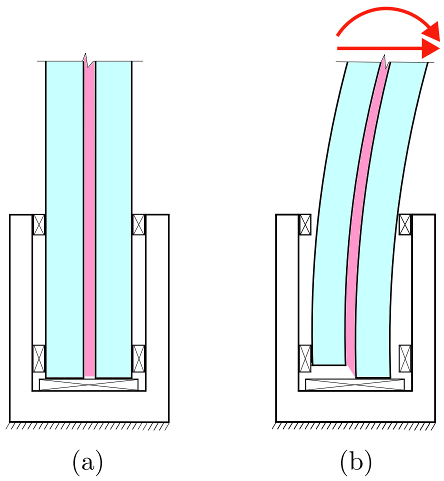

Figure 3.8: Schematic representation of cantilevered laminated-glass balustrade inserted in an U-shaped base-shoe: (a) undistorted configuration and (b) point-wise contact under the applied load, with evidence of the warping of the end cross section.

The static scheme commonly adapted to represent this type of U-shaped support [50] is presented in Figure 3.9. The distributed load represents the wind pressure, while the concentrated force represents the barrier load; both loads are multiplied by the width of the balustrade.

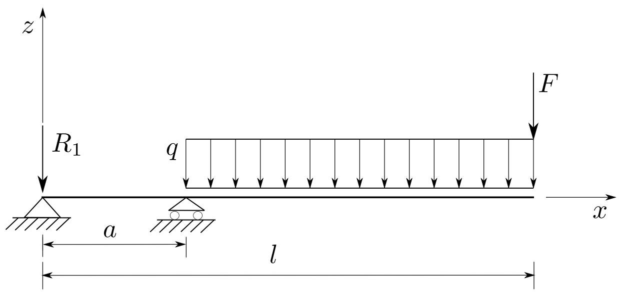

Figure 3.9: Static scheme for cantilevered LG balustrades, made of glass panes continuously supported at one edge by U-profile base-shoes.

The solution is obtained separately for each load case, and then the principle of superposition can be applied to obtain the structural response under the combined action of these loads, considering that the deformation is in the linear elastic regime. Following the SZT, the kinematic variables are the deflection $w_0(x)$ of the beam axis and the function $\psi(x)$, which is related to the average shear angle and represents the amplitude of the zigzag function along the beam axis. Here, is a presentation of the solution for a symmetric package, as it is the case of interest for design practice. The case of an asymmetrical section can be treated similarly, although the resulting expressions are much more lengthy.

Let Er be the Young's modulus of glass, and Gp the elastic shear modulus of the polymer forming the interlayer. The energy functional takes the following form:

$$
\begin{aligned}
\mathcal{E} = & \frac{1}{2}\mathrm{Er}\int_0^l \Big[\mathrm{Ig}\ \left(w_0''(x)\right)^2 + \mathrm{Ig}_1\ \left(\psi'(x)\right)^2 - 2\,\mathrm{Ig}_2\, w_0''(x)\,\psi'(x)\Big]\,dx \\
& + \frac{1}{2}\int_0^l \mathrm{As}\,\mathrm{Gp}\,\psi\,(x)^2 dx + \int_a^l q\,w_0\,(x)\,dx + F\,w_0\,(l)\ ,
\end{aligned}
\tag{3.51}
$$

where $'$ denotes differentiation with respect to the variable x. Observe that the positive direction of deflection $w_0(x)$ is along the axis z, whereas both q and F are positive in the opposite direction.

The first variation of the energy functional with respect to $w_0(x)$ and $\psi(x)$ provides the Euler-Lagrange equations:

$$
\mathrm{Er}\,\mathrm{Ig}\,w_0''''(x) - \mathrm{Er}\,\mathrm{Ig}_2\,\psi'''(x) + q\,\mathcal{H}\,(x-a) = 0\,, \tag{3.52a}
$$

$$
\mathrm{Er}\,\mathrm{Ig}_2\,w_0'''(x) - \mathrm{Er}\,\mathrm{Ig}_1\,\psi''(x) + \mathrm{As}\,\mathrm{Gp}\,\psi(x) = 0\,, \tag{3.52b}
$$

where $\mathcal{H}(\cdot)$ is the Heaviside unit step function.

The system (3.52) has to be distinctly integrated in the domains $0 < x < a$ and $a < x < l$, and the solution is found by using boundary conditions at $x = 0$ and $x = l$, as well as matching conditions at $x = a^-$ and $x = a^+$. These can be either of geometric or natural type. Observe that the warping of the cross section is not assigned at $x = 0$ and $x = l$: this implies that the variations $\delta\psi(x)_{x=0}$ and $\delta\psi(x)_{x=l}$ are arbitrary. Obviously, also $\delta w_0'(x)_{x=0}$, $\delta w_0(x)_{x=l}$, and $\delta w_0'(x)_{x=l}$ are not assigned.

In conclusion, one has two geometric boundary conditions, i.e.,

$$
w_0(0) = 0\,, \tag{3.53a}
$$

$$
w_0(a) = 0\,, \tag{3.53b}
$$

and, five natural boundary conditions of the form

$$
\mathrm{Er}\,[\mathrm{Ig}\,w_0''(0) - \mathrm{Ig}_2\,\psi'(0)] = 0\,, \tag{3.54a}
$$

$$
\mathrm{Er}\,[\mathrm{Ig}\,w_0''(l) - \mathrm{Ig}_2\,\psi'(l)] = 0\,, \tag{3.54b}
$$

$$
\mathrm{Er}\,[\mathrm{Ig}\,w_0'''(l) - \mathrm{Ig}_2\,\psi''(l)] = F\,, \tag{3.54c}
$$

$$
\mathrm{Er}\,[\mathrm{Ig}_2\,w_0''(0) - \mathrm{Ig}_1\,\psi'(0)] = 0\,, \tag{3.54d}
$$

$$
\mathrm{Er}\,[\mathrm{Ig}_2\,w_0''(l) - \mathrm{Ig}_1\,\psi'(l)] = 0\,. \tag{3.54e}
$$

The geometric matching conditions at the interface point $x = a$ involve, apart from the continuity of the displacement field $w_0(x)$ and its first derivative $w_0'(x)$, the continuity of the shear function $\psi(x)$. In fact, this is associated with the warping of the cross sections: if $\psi(x)$ were not continuous, there would be a mismatch in the cross-sectional deformation at the interface point. In conclusion, the geometric matching conditions read

$$w_0(a^-) = w_0(a^+)\,, \tag{3.55a}$$
$$w_0'(a^-) = w_0'(a^+)\,, \tag{3.55b}$$
$$\psi(a^-) = \psi(a^+)\,, \tag{3.55c}$$

and the corresponding natural matching conditions

$$\mathrm{Ig}_2\, w_0''(a^-) - \mathrm{Ig}_1\psi'(a^-) = \mathrm{Ig}_2\, w_0''(a^+) - \mathrm{Ig}_1\psi'(a^+)\,, \tag{3.56a}$$
$$\mathrm{Ig}\, w_0''(a^-) - \mathrm{Ig}_2\psi'(a^-) = \mathrm{Ig}\, w_0''(a^+) - \mathrm{Ig}_2\, \psi'(a^+)\,. \tag{3.56b}$$

Consequently, in total, one has 12 conditions. The system of differential equations (3.52) is of the fourth order in $w_0(x)$ and of the second order in $\psi(x)$. In fact, one can differentiate (3.52b), find from this $\psi'''(x)$, and substitute it in (3.52a) to eliminate the third-order dependence in $\psi(x)$. Therefore, the number of conditions matches the order of the equations, which are to be integrated in two distinct domains.

The matching conditions (3.56), since $\mathrm{Ig}\,\mathrm{Ig}_1 - \mathrm{Ig}_2^2 \neq 0$, as detailed in the 3.4, can be restated as

$$w_0''\left(a^-\right) = w_0''\left(a^+\right)\,, \tag{3.57a}$$
$$\psi'\left(a^-\right) = \psi'\left(a^+\right)\,. \tag{3.57b}$$

Furthermore, one can conclude from (3.54a) and (3.54d) that

$$w_0''(0) = 0\,, \tag{3.58a}$$
$$\psi'(0) = 0\,, \tag{3.58b}$$

and from (3.54b) and (3.54e) that

$$w_0''(l) = 0\,, \tag{3.59a}$$
$$\psi'(l) = 0\,. \tag{3.59b}$$

It is useful to recall, from [19], the expressions for normal stress in the k-th glass ply (k odd) and shear stresses in the k-th interlayer (k even), which take the form

$$\sigma_x^k(x,z) = \mathrm{Er}\left[-z\, w_0''(x) + (z+\phi_k(z))\ \psi'(x)\right] , \tag{3.60a}$$

$$\tau_{xz}^k(x) = \mathrm{Gp}\, \gamma_{xz}^k(x) = \mathrm{Gp}\,(1+\alpha_k)\ \psi(x)\,, \tag{3.60b}$$

where $\phi_k(z)$ is the zigzag function defined in (3.13).

3.3.3 Solution of the Differential Equations

The analytic solution of the governing equations presented in Section 3.3.2 is now illustrated. This will be successively used to derive exact expressions for the effective thickness of the cantilevered laminate. The solution is produced separately for each load configuration of Figure 3.9, associated with either q (Case 1) or F (Case 2).

Case 1: uniformaly distributed load

Let $F = 0$ and $q \neq 0$. Equation (3.52a) can be integrated twice on the domain $x \in (0,a)$ and $x \in (a,l)$, obtaining four constants that can be determined by using the boundary conditions (3.54c), (3.58), (3.59), and the matching condition (3.57). Hence, one obtains

$$\mathrm{Er}\,[\,\mathrm{Ig}\, w_0''(x) -\ \mathrm{Ig}_2\, \psi'(x)] + \frac{q\,(l-a)^2}{2\,a}\, x\ = 0\,, \quad x \in (0,a)\,, \tag{3.61a}$$

$$\mathrm{Er}\,[\,\mathrm{Ig}\, w_0''(x) -\ \mathrm{Ig}_2\, \psi'(x)] + \frac{q\,(l-x)^2}{2} = 0\,, \quad x \in (a,l)\,, \tag{3.61b}$$

Observe that

$$R_1 = \frac{q\,(l-a)^2}{2a}\,, \tag{3.62}$$

represents the constrain reaction at the l.h.s. support, as indicated in Figure (3.9).

Substituting $w_0'''(x)$ from (3.61) in (3.52b), provides

$$\mathrm{Er}\,\left(\frac{\mathrm{Ig_2}^2}{\mathrm{Ig}} - \mathrm{Ig}_1\right)\psi''(x) + \mathrm{As}\,\mathrm{Gp}\,\psi\,(x) - \frac{\mathrm{Ig}_2}{\mathrm{Ig}}\,R_1 = 0\,, \quad x \in (0,a)\,, \tag{3.63a}$$

$$\mathrm{Er}\,\left(\frac{\mathrm{Ig_2}^2}{\mathrm{Ig}} - \mathrm{Ig}_1\right)\psi''(x) + \mathrm{As}\,\mathrm{Gp}\,\psi\,(x) + \frac{\mathrm{Ig}_2}{\mathrm{Ig}}\,q\,(l-x) = 0\,, \quad x \in (a,l)\,. \tag{3.63b}$$

Since, as shown in the 3.4, it can the proved that $\left(\mathrm{Ig}\,\mathrm{Ig}_1 - {\mathrm{Ig}_2}^2\right) > 0$, one can define the length scale $\lambda > 0$ such that

$$\lambda^2 = \frac{\mathrm{Er}\left(\mathrm{Ig}\,\mathrm{Ig}_1 - {\mathrm{Ig}_2}^2\right)}{\mathrm{Gp}\,\mathrm{As}\,\mathrm{Ig}}\,. \tag{3.64a}$$

It is also convenient to introduce the force R_0 in the form

$$R_0 = \frac{\mathrm{As}\,\mathrm{Gp}\,\mathrm{Ig}}{\mathrm{Ig}_2}\,, \tag{3.64b}$$

so that (3.63) becomes

$$\psi(x) - \lambda^2\,\psi''(x) - \frac{R_1}{R_0} = 0\,, \quad x \in (0,a)\,, \tag{3.65a}$$

$$\psi(x) - \lambda^2\,\psi''(x) + \frac{q\,(l-x)}{R_0} = 0\,, \quad x \in (a,l)\,. \tag{3.65b}$$

Applying the boundary conditions (3.58b) and (3.59b), one obtains an expression for $\psi(x)$ that contains one integration constant for each domain, i.e.,

$$\psi(x) = C_1\left(\mathrm{e}^{x/\lambda} + \mathrm{e}^{-x/\lambda}\right) + \frac{R_1}{R_0}\,, \quad x \in (0,a)\,, \tag{3.66a}$$

$$\psi(x) = C_2\left(\mathrm{e}^{x/\lambda} + \mathrm{e}^{\frac{2\,l-x}{\lambda}}\right) - \frac{q}{R_0}\left(l - x - \lambda\,\mathrm{e}^{\frac{l-x}{\lambda}}\right)\,, \quad x \in (a,l)\,. \tag{3.66b}$$

The constants C_1, C_2 can be found with the matching conditions(3.55c), and (3.57b), as

$$C_1 = \frac{\left((l-a+\lambda)\,\mathrm{e}^{\frac{2\,a}{\lambda}} - (l-a-\lambda)\,\mathrm{e}^{\frac{2\,l}{\lambda}} - 2\,\lambda\,\mathrm{e}^{\frac{l+a}{\lambda}}\right) q + \left(\mathrm{e}^{\frac{2\,a}{\lambda}} - \mathrm{e}^{\frac{2\,l}{\lambda}}\right) R_1}{2\,R_0\,\mathrm{e}^{a/\lambda}\left(\mathrm{e}^{\frac{2\,l}{\lambda}} - 1\right)}\,, \tag{3.67a}$$

$$C_2 = \frac{\left((l-a+\lambda)\,\mathrm{e}^{\frac{2\,a}{\lambda}} - (l-a-\lambda) - 2\,\lambda\,\mathrm{e}^{\frac{l+a}{\lambda}}\right) q + \left(\mathrm{e}^{\frac{2\,a}{\lambda}} - 1\right) R_1}{2\,R_0\,\mathrm{e}^{a/\lambda}\left(1 - \mathrm{e}^{\frac{2\,l}{\lambda}}\right)}\,. \tag{3.67b}$$

Now that $\psi(x)$ is known on both domains, it can be substituted in (3.61), so to find

$$w_0''(x) = \frac{\mathrm{Ig}_2\,C_1}{\mathrm{Ig}\,\lambda}\left(\mathrm{e}^{x/\lambda} - \mathrm{e}^{-\frac{x}{\lambda}}\right) - \frac{R_1\,x}{\mathrm{Er}\,\mathrm{Ig}}\,, \quad x \in (0,a)\,, \tag{3.68a}$$

$$w_0''(x) = \frac{\mathrm{Ig}_2\, q}{\mathrm{Ig}\, R_0}\left(1 - \mathrm{e}^{\frac{l-x}{\lambda}}\right) + \frac{C_2\, \mathrm{Ig}_2}{\mathrm{Ig}\, \lambda}\, \mathrm{e}^{x/\lambda}\left(1 - \mathrm{e}^{\frac{2\,(l-x)}{\lambda}}\right) - \frac{q\,(l-x)^2}{2\, \mathrm{Er}\, \mathrm{Ig}}\,, \quad x \in (a, l)\,. \tag{3.68b}$$

Integrating (3.68a) twice and considering the boundary conditions (3.53), one finds

$$w_0\,(x) = \frac{2\, \mathrm{Ig}_2}{\mathrm{Ig}}\, C_1\, \lambda\left[\sinh\left(\frac{x}{\lambda}\right) - \sinh\left(\frac{a}{\lambda}\right)\frac{x}{a}\right] - \frac{R_1\, x}{6\, \mathrm{Er}\, \mathrm{Ig}}(x^2 - a^2)\,, \quad x \in (0, a)\,. \tag{3.69}$$

On the other hand, from integration of (3.68b) one obtains

$$\begin{aligned} w_0\,(x) = {} & \frac{C_2\, \mathrm{Ig}_2\, \lambda}{\mathrm{Ig}}\, \mathrm{e}^{x/\lambda}\left(1 - \mathrm{e}^{\frac{2\,(l-x)}{\lambda}}\right) + \frac{\mathrm{Ig}_2\, q}{\mathrm{Ig}\, R_0}\left(\frac{x^2}{2} - \lambda^2\, \mathrm{e}^{\frac{l-x}{\lambda}}\right) - \frac{q\, x^2\,(x^2 - 4\, l\, x + 6\, l^2)}{24\, \mathrm{Er}\, \mathrm{Ig}} \\ & + C_3\, x + C_4\,, \quad x \in (a, l)\,. \end{aligned} \tag{3.70}$$

From the matching condition (3.55b) one can calculate the constant C_3, i.e.

$$\begin{aligned} C_3 = {} & \frac{2\, C_1\, \mathrm{Ig}_2}{\mathrm{Ig}}\left(\cosh\left(\frac{a}{\lambda}\right) - \frac{\lambda}{a}\sinh\left(\frac{a}{\lambda}\right)\right) - \frac{C_2\, \mathrm{Ig}_2}{\mathrm{Ig}}\mathrm{e}^{a/\lambda}\left(\mathrm{e}^{\frac{2\,(l-a)}{\lambda}} + 1\right) \\ & - \frac{\mathrm{Ig}_2\, q}{\mathrm{Ig}\, R_0}\left(a + \lambda\, \mathrm{e}^{\frac{l-a}{\lambda}}\right) + \frac{a\, q\,(a^2 - 3\, a\, l + 3\, l^2)}{6\, \mathrm{Er}\, \mathrm{Ig}} - \frac{R_1\, a^2}{3\, \mathrm{Er}\, \mathrm{Ig}}\,. \end{aligned} \tag{3.71}$$

Finally, from (3.53b), one obtains that C_4 reads

$$C_4 = \frac{\mathrm{Ig}_2\, q}{\mathrm{Ig}\, R_0}\left(\lambda^2\, \mathrm{e}^{\frac{l-a}{\lambda}} - \frac{a^2}{2}\right) - \frac{C_2\, \mathrm{Ig}_2\, \lambda}{\mathrm{Ig}}\, \mathrm{e}^{a/\lambda}\left(1 - \mathrm{e}^{\frac{2\,(l-a)}{\lambda}}\right) + \frac{q\, a^2\,(a^2 - 4\, l\, a + 6\, l^2)}{24\, \mathrm{Er}\, \mathrm{Ig}} - C_3\, a\,. \tag{3.72}$$

The resulting expressions are quite lengthy, but can be easily calculated with an Excel spreadsheet as functions of the geometric and elastic parameters.

Case 2: concentrated tip force

Let now $q = 0$ and $F \neq 0$. The integration of the system (3.52) follows the same procedure detailed above.

The expression of $\psi(x)$ for $x \in (0,a)$ takes the same form (3.66a) provided that the value of R_1 is substituted with

$$R_1 = \frac{F(l-a)}{a} \,, \tag{3.73}$$

and the constant C_1 with

$$C_1 = \frac{(F+R_1)\left(\mathrm{e}^{\frac{a}{\lambda}} - \mathrm{e}^{\frac{2\,l-a}{\lambda}}\right)}{2\,R_0\left(\mathrm{e}^{\frac{2\,l}{\lambda}}-1\right)} \,. \tag{3.74}$$

On the other hand, the expression for $\psi(x)$ for $x \in (a,l)$ will change because this portion of the beam has a different load. One obtains

$$\psi(x) = C_2\left(\mathrm{e}^{x/\lambda} + \mathrm{e}^{\frac{2\,l-x}{\lambda}}\right) - \frac{F}{R_0} \,, \quad x \in (a,l)\,, \tag{3.75}$$

where

$$C_2 = \frac{(F+R_1)\,\sinh(\frac{a}{\lambda})}{R_0\left(\mathrm{e}^{\frac{2\,l}{\lambda}}-1\right)} \,. \tag{3.76}$$

Similarly, the expression for $w_0(x)$ for $x \in (0,a)$ is the same of (3.69), provided that the new value (3.73) is substituted for R_1. Instead, for $x \in (a,l)$, the displacement $w_0(x)$ takes the form

$$w_0(x) = \frac{C_2\,\mathrm{Ig}_2\,\lambda}{\mathrm{Ig}}\,\mathrm{e}^{x/\lambda}\left(1-\mathrm{e}^{\frac{2\,(l-x)}{\lambda}}\right) + \frac{F\,x^2\,(x-3\,l)}{6\,\mathrm{Er}\,\mathrm{Ig}} + C_3\,x + C_4, \quad x \in (a,l), \tag{3.77}$$

where

$$\begin{aligned} C_3 = & \frac{2\,C_1\,\mathrm{Ig}_2}{\mathrm{Ig}}\left(\cosh\left(\frac{a}{\lambda}\right) - \frac{\lambda}{a}\sinh\left(\frac{a}{\lambda}\right)\right) - \frac{C_2\,\mathrm{Ig}_2}{\mathrm{Ig}}\,\mathrm{e}^{a/\lambda}\left(\mathrm{e}^{\frac{2\,(l-a)}{\lambda}}+1\right) \\ & - \frac{F\,a\,(a-2\,l)}{2\,\mathrm{Er}\,\mathrm{Ig}} - \frac{R_1\,a^2}{3\,\mathrm{Er}\,\mathrm{Ig}} \,. \end{aligned} \tag{3.78}$$

and

$$C_4 = \frac{C_2 \,\mathrm{Ig}_2 \,\lambda}{\mathrm{Ig}} \,\mathrm{e}^{a/\lambda} \left(\mathrm{e}^{\frac{2\,(l-a)}{\lambda}} - 1 \right) - \frac{F\,a^2\,(\,a - 3\,l)}{6\,\mathrm{Er}\,\mathrm{Ig}} - C_3\,a\,. \tag{3.79}$$

It is logical that the form of the solutions coincides for $x \in (0, a)$ because, here, the shape of the shear and bending moment diagrams is the same for the two load conditions. This is not true for $x \in (a, l)$.

3.3.4 Exact Effective Thickness

The expressions for deflection effective thickness and stress effective thickness are now obtained from the analytic solution.

Deflection effective thickness

The deflection effective thickness is calculated by comparing the *maximum* deflection δ_{max} of a beam with a laminated cross section with that of a beam with a monolithic cross section. Considering the beam represented in Figure 3.9, the maximum displacement occurs at the tip of the cantilevered portion $x = l$.

Let I_m be the moment of inertia of a monolithic cross section; thus, the maximum deflection of a beam with this section is given by

$$\delta_m = \frac{Fl^3}{3E_mI_m},$$

where F is the applied concentrated force at the tip, E_m is the Young's modulus of the monolithic material, and l is the length of the cantilever.

$$\delta_{max} = \frac{q\,(l-a)^3\,(3\,l + a)}{24\,\mathrm{Er}\,\mathrm{I_m}}\,. \tag{3.80}$$

Comparing with the value of the maximum deflection of a laminated beam from (3.70), one can find that the two values coincide provided that

$$\mathrm{I_m} = \frac{\mathrm{Ig}\,R_0\,(l-a)^3\,(3\,l+a)}{R_0\,\left(a^4 - 2\,a^2\,l^2 - 3\,l^4\right) + 24\,\mathrm{Er}\,\mathrm{Ig}_2\,l^2 + 24\,\dfrac{C_3}{q}\,\mathrm{Er}\,\mathrm{Ig}\,R_0\,l}\,, \tag{3.81}$$

Observe that $\mathrm{I_m}$ is not a function of the external load because C_3/q does not depend on q, as per (3.71).

Under the concentrated load F, one obtains for the monolith

$$\delta_{max} = \frac{F\,(l-a)^2\,l}{3\,\mathrm{Er}\,\mathrm{I_m}}\,, \tag{3.82}$$

whereas the deflection of the laminate is given by (3.77) for $x = l$. Equating the two values, one finds

$$\mathrm{I_m} = \frac{2\,\mathrm{Ig}\,R_0\,(l-a)^2}{6\,\mathrm{Er}\,\mathrm{Ig}_2 - R_0\,(2\,l^2+a^2) + 6\,\dfrac{C_3}{F}\,\mathrm{Er}\,\mathrm{Ig}\,R_0}\,, \tag{3.83}$$

Observe that also here $\mathrm{I_m}$ is independent of F because so is C_3/F, as per (3.78).

Once $\mathrm{I_m}$ has been calculated, the effective thickness h_w for deflection can be expressed as

$$h_w = \left(\frac{12}{b}\mathrm{I_m}\right)^{1/3}\,. \tag{3.84}$$

These formulae can be readily used in the design process.

Stress effective thickness

The thickness of a beam with a homogeneous section that undergoes the same maximum tensile stress of a beam with an inhomogeneous cross section, under the same static configuration, is the stress effective thickness, denoted as h_s. Considering the static scheme of Figure 3.9, the maximum tensile stress occurs at $x = a$, at the extrados of the laminated beam.

Let M_{max} be the bending moment at the critical section of a beam with a homogeneous section; the maximum stress is given by

$$\sigma_{max} = \frac{6\,M_{max}}{b\,h_s^2}\,. \tag{3.85}$$

From (3.60a), one can calculate the maximum stress in a beam with an inhomogeneous cross section. This stress occurs at $x = a$; consequently, one can equivalently use the solution from either of the domains $x \in (0,a)$ or $x \in (a,l)$.

For the case with distributed load q, the effective thickness h_s is

$$h_s^2 = \frac{12\,\lambda\,\mathrm{Ig}\,(l-a)^2}{b\,h\left(\lambda\,(l^2+a^2-2\,a\,l) + 4\,\dfrac{C_1}{q}\,\mathrm{Er}\;\sinh\left(\frac{a}{\lambda}\right)(\mathrm{Ig}-\mathrm{Ig}_2)\right)}\,. \tag{3.86}$$

And for the case with concentrated load F it becomes

$$h_s^2 = \frac{12\,\lambda\,\mathrm{Ig}\,(l-a)}{b\,h\left(\lambda\,(l-a) + 2\,\dfrac{C_1}{F}\,\mathrm{Er}\;\sinh\left(\frac{a}{\lambda}\right)(\mathrm{Ig}-\mathrm{Ig}_2)\right)}\,. \tag{3.87}$$

Again, observe from (3.67a) and (3.74) that, since C_1/q and C_1/F are independent of q and F, respectively, the stress effective thickness does not depend on the value of the applied load.

3.3.5 Examples

The analytic solution obtained in previous sections is applied here to a particular geometry under two loading conditions. Consider the static scheme in Figure 3.9, where $a = 0.1\,\mathrm{m}$ and $l = 1.1\,\mathrm{m}$. The laminated beam, of width $b = 1\,\mathrm{m}$, is made of two external glass plies with a thickness of $h_g = 12\,\mathrm{mm}$ and Young's modulus $\mathrm{Er} = 70\,\mathrm{GPa}$, while the interlayer has a thickness of $t = 1.52\,\mathrm{mm}$ and varying shear modulus $\mathrm{Gp} = 0.1,\ 1,\ 10,\ 100\,\mathrm{MPa}$.

Beam under uniformly distributed load

Here the beam is subject to a uniformly distributed load $q = 1\,\mathrm{kN/m}$. Figures 3.10(a) and 3.10(b) respectively show the graphs of the transverse displacement $w_0(x)$ and the average shear angle $\psi(x)$ at $x \in (0, l)$ for different values of Gp. When the value of the interlayer's shear modulus Gp is high, the monolithic limit is reached and the average shear angle $\psi(x)$ approaches zero. From Figure 3.10(b), one can see that when $\mathrm{Gp} = 100\,\mathrm{MPa}$, the monolithic limit is achieved for $x \in (a, l)$, whereas in the simply supported portion of the beam, $x \in (0, a)$, where the maximum shear force is present, even when the value of Gp is high, the monolithic limit is not reached and the warping of the cross section is still evident. Considering the curve with the minimum value of shear modulus $\mathrm{Gp} = 0.1\,\mathrm{MPa}$, the response of the laminated section approaches the layered limit. In this case, the relative in-plane displacement of the glass surfaces is evident in the trend of $\psi(x)$. The highest value of $\psi(x)$ occurs at $x = 0$, where the cross section experiences maximum warping. It is clear that the warping of the cross section has a dominant effect on the entire structural response. The asymmetric distribution of $\psi(x)$ presents the main reason why the EET approach [52] cannot accurately represent a laminated balustrade, considering that the assumed shape function in the EET cannot accommodate such strong shearing of the interlayers.

Figure 3.11 shows the maximum tensile stress $\sigma(x)$ present at the extrados of the upper glass ply of the cross-section. The shape of these graphs deviates slightly from that of the bending moment. This is because the warping of the cross-section

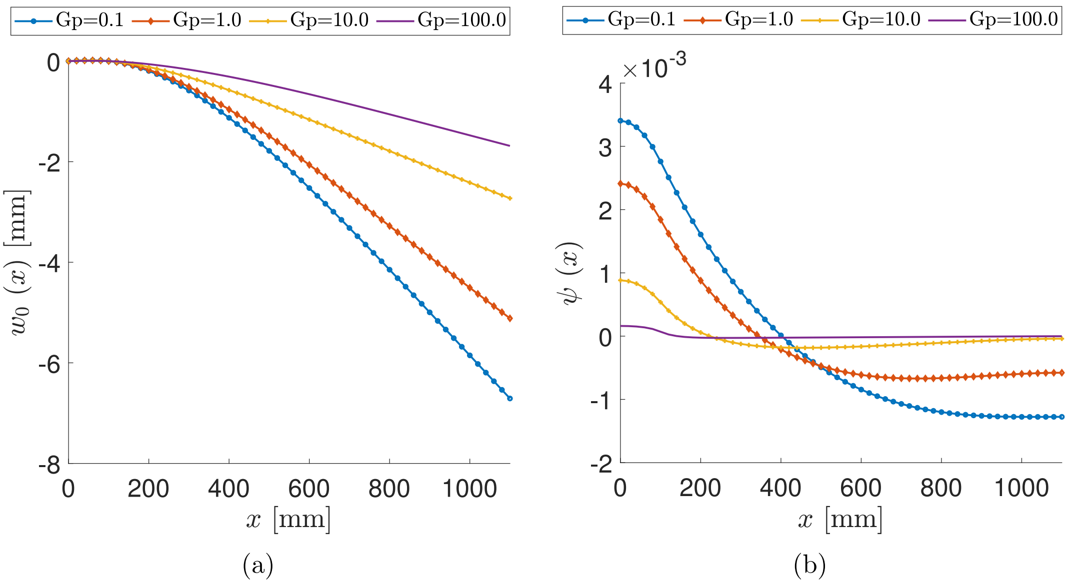

Figure 3.10: Laminated beam under distributed load $q = 1\,\mathrm{KN/m}$. Graphs of (a) the transversal displacement $w_0(x)$ and (b) the average shear angle $\psi(x)$, for $x \in (0, l)$ ($a = 0.1\,\mathrm{m}$, and $l = 1.1\,\mathrm{m}$) and for Gp $= 0.1$, 1, 10, 100 MPa.

is variable along the beam axis, making this response equivalent to that of a beam with a variable cross-section. When the shear modulus Gp $= 1$, 10 MPa, one can notice that the stress value at the extrados can take negative values near the free end $x = l$. This is an expected result, justified by the straining of the interlayer, which causes compression in both glass plies when the curvature vanishes in the proximity of the free end.

Section 3.3.4 demonstrated the calculation of the exact effective thickness, and the corresponding results for this particular static scheme are reported as semi-logarithmic plots in Figure 3.12. The stress- and deflection-effective thicknesses are denoted as h_s and h_w, respectively. From this figure, one can note that the monolithic limit is not reached even for high values of the shear modulus (Gp $\simeq 10^2$ MPa). This is due to the peculiar static scheme, where the high shear stress in the interlayer is concentrated in the simply supported portion of the beam $x \in (0, a)$, causing relative sliding of the glass plies. Similarly, even for low values of the shear modulus, it is observed that the interlayer provides a modest degree of shear coupling; hence, the layered limit is not completely reached.

A comparison between the effective thickness calculated using the proposed model, labeled SZ (Special Zigzag), and other approaches reported in the literature is presented in Figure 3.13. The SZ solution is compared to the CBET approach [53], the W-B method [54], and the EET method [52]. Despite the differences in the analytic expressions, a perfect agreement between the SZ and the CBET is found. In fact, the CBET method is based on an approximate solution, while the SZ relies on an exact solution. Moreover, the SZ framework is much more general, as it applies to multi-laminates of arbitrary composition. However, the example presented here is a three-layered laminate to permit comparison with the only case that the CBET method can handle. It should also be mentioned that the CBET method has

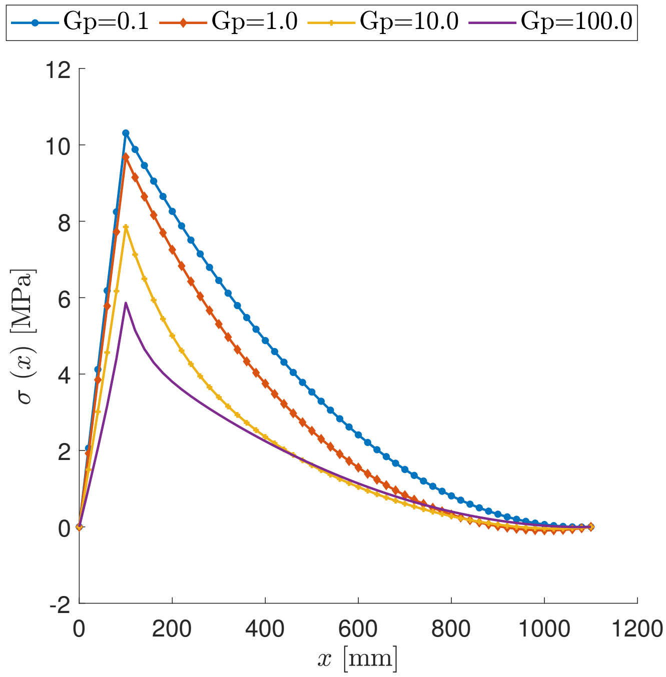

Figure 3.11: Laminated beam under distributed load q. Graphs of the maximum stress at the extrados as a function of $x \in (0, l)$, for Gp = 0.1, 1, 10, 100 MPa.

been corroborated [53] by numerical simulations with Strand7 (2015); therefore, the excellent fit also provides further proof of the validity of the SZ approach.

One can see that both the EET and the W-B approaches overestimated the effective thickness, resulting in an underestimation of deflection and stress. This can be explained by the fact that these approaches cannot properly consider the strong effect of the asymmetrical deformation of the beam on the warping of the cross section at the supported end.

Beam under concentrated tip force

The beam in Figure 3.9 is subject to a concentrated force $F = 2\,\text{kN}$ at the tip $x = l$. The graphs of $w_0(x)$ and $\psi(x)$ are presented in Figures 3.14(a) and 3.14(b), respectively. While the deflection under the concentrated load is considerably higher than in the distributed load case shown in Figure 3.10(a), there are no appreciable differences at the qualitative level. Concerning the average shear angle trend in the case of distributed load in Figure 3.10(b), the graph now shows higher absolute values. The ratio $|\psi(l)/\psi(0)|$ is much higher than under distributed loads, evidently because the overall shear force in the beam is now constant in $x \in (a, l)$. In contrast, it was linearly decreasing in the previous case.

In Figure 3.15, the graphs for the stress at the extrados of the upper glass ply are reported. It is found that in this case, the deviation of these graphs from the graph of bending moment is much more evident than in the case with the distributed load

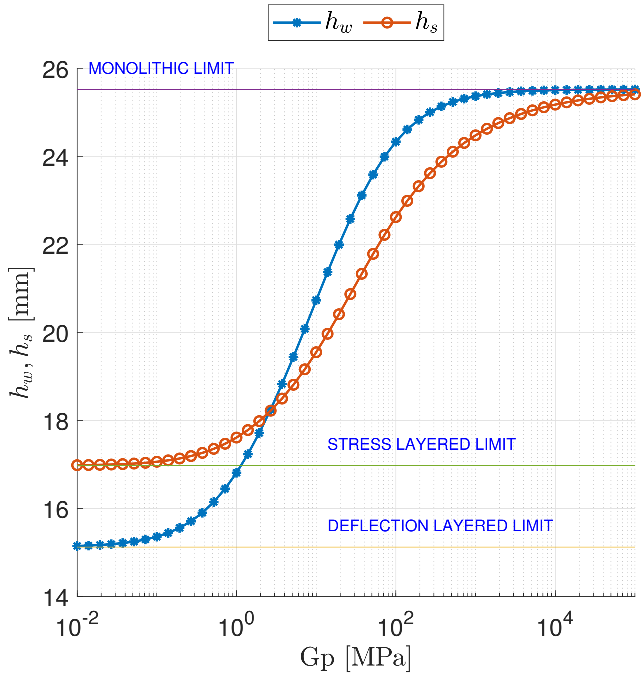

Figure 3.12: Laminated beam under distributed load q. Graph of deflection-effective-thickness h_w and stress-effective-thickness h_s as a function of the shear modulus Gp of the interlayer (semi-log plot).

shown in Figure 3.11, especially for high values of the shear modulus G_p, particularly in the proximity of the middle support $x = a$. Contrary to the case with distributed load in Figure 3.11, the graphs do not show any negative values of stress, because the effect of beam curvature is always dominant in comparison to the axial force induced by the straining of the interlayer.

The deflection-effective thickness h_w and the stress-effective thickness h_s are shown in Figure 3.16. With respect to their counterparts in Figure 3.12 for the distributed load, there are no appreciable differences. The same conclusions from the previous section hold.

Figure 3.17 is the counterpart of Figure 3.13 for the case of a concentrated tip force. Again, one can notice the perfect agreement of the proposed SZ with the CBET model. Similarly to the distributed load case, the effective thicknesses calculated using the W-B and EET methods are overestimated.

3.4 Demonstration of the Inequality $\mathrm{Ig}\,\mathrm{Ig}_1 > \mathrm{Ig}_2{}^2$

Hereafter we prove that the constant λ^2, defined in (3.64a), is positive, because $\mathrm{Ig}\,\mathrm{Ig}_1 > \mathrm{Ig}_2{}^2$. We use an argument similar to that often used to demontrate the Cauchy-Schwarz-Bunyakovsky inequality.

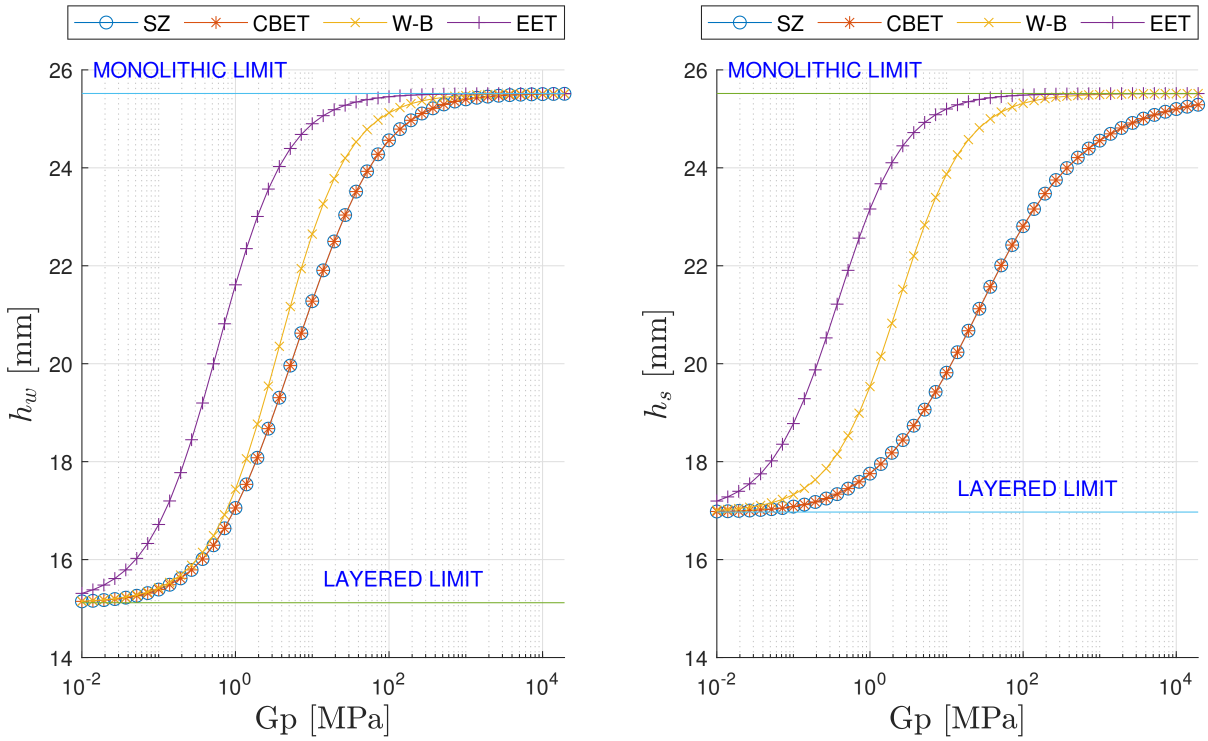

Figure 3.13: Deflection effective thickness h_w and stress effective thickness h_s of the laminated beam under distributed load q. Graphs of comparison between the proposed approach (SZ) and other methods (CBET, W-B, ETT).

Clearly

$$\forall\, s \in \mathbb{R} : \quad \left(s\, z + (z_k + \bar{\phi}_{k-1})\right)^2 \geq 0\,. \tag{3.88}$$

However, assigned any $s \in \mathbb{R}$, one has that

$$\sum_{k=1}^{N} \int_{A_k} \left(s\, z + (z_k + \bar{\phi}_{k-1})\right)^2 dA > 0\,, \tag{3.89}$$

where the strict sign of inequality is due to the fact that $z_k + \bar{\phi}_{k-1}$ is a constant that cannot vanish in all the domains A_k, whereas z is the variable, so that the integrand cannot be identically zero everywhere.

Expanding, one obtains

$$s^2 \left[\sum_{k=1}^{N} \int_{A_k} z^2\, dA\right] + 2\, s \left[\sum_{k=1}^{N} \int_{A_k} z\, (z_k + \bar{\phi}_{k-1})\, dA\right] + \left[\sum_{k=1}^{N} \int_{A_k} (z_k + \bar{\phi}_{k-1})^2 dA\right] > 0\,. \tag{3.90}$$

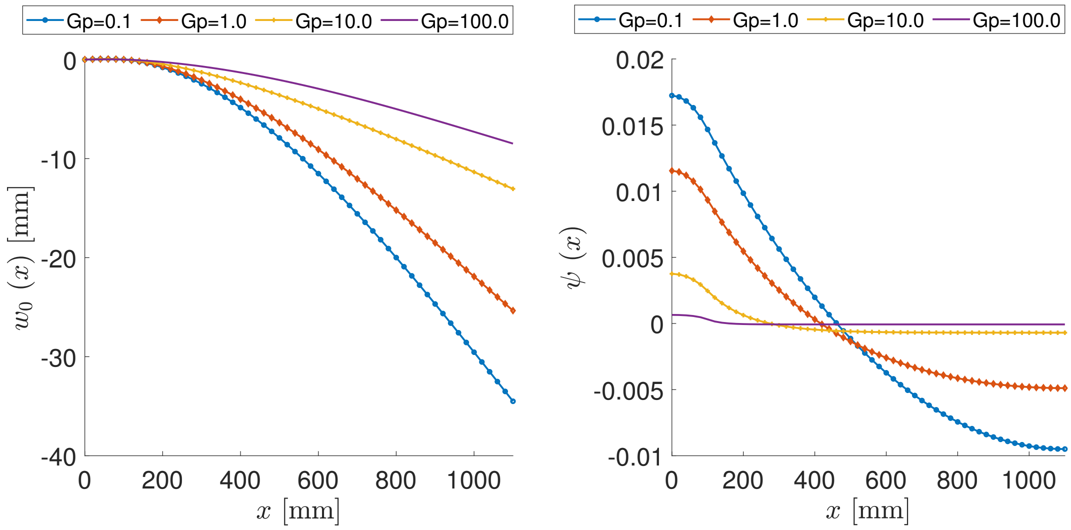

(a) (b)

Figure 3.14: Laminated beam under concentrated tip force $F = 2\,\mathrm{KN}$. Graphs of (a) the transversal displacement $w_0(x)$ and (b) the average shear angle $\psi(x)$, for $x \in (0, l)$ ($a = 0.1\,\mathrm{m}$, and $l = 1.1\,\mathrm{m}$) and for $\mathrm{Gp} = 0.1,\ 1,\ 10,\ 100\,\mathrm{MPa}$.

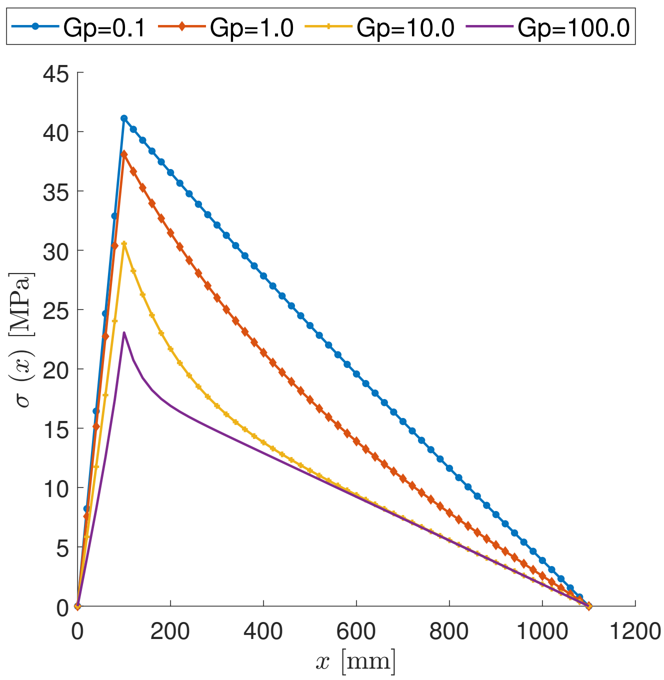

Figure 3.15: Laminated beam under concentrated tip force F. Graphs of the maximum stress at the extrados as a function of $x \in (0, l)$, for $\mathrm{Gp} = 0.1,\ 1,\ 10,\ 100\,\mathrm{MPa}$.

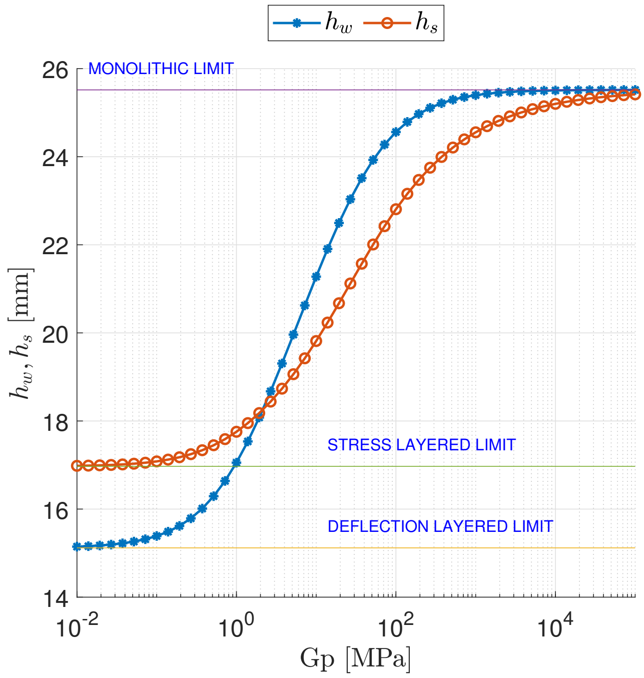

Figure 3.16: Laminated beam under concentrated tip force F. Graph of deflection-effective-thickness h_w and stress-effective-thickness h_s as a function of the shear modulus Gp of the interlayer (semi-log plot).

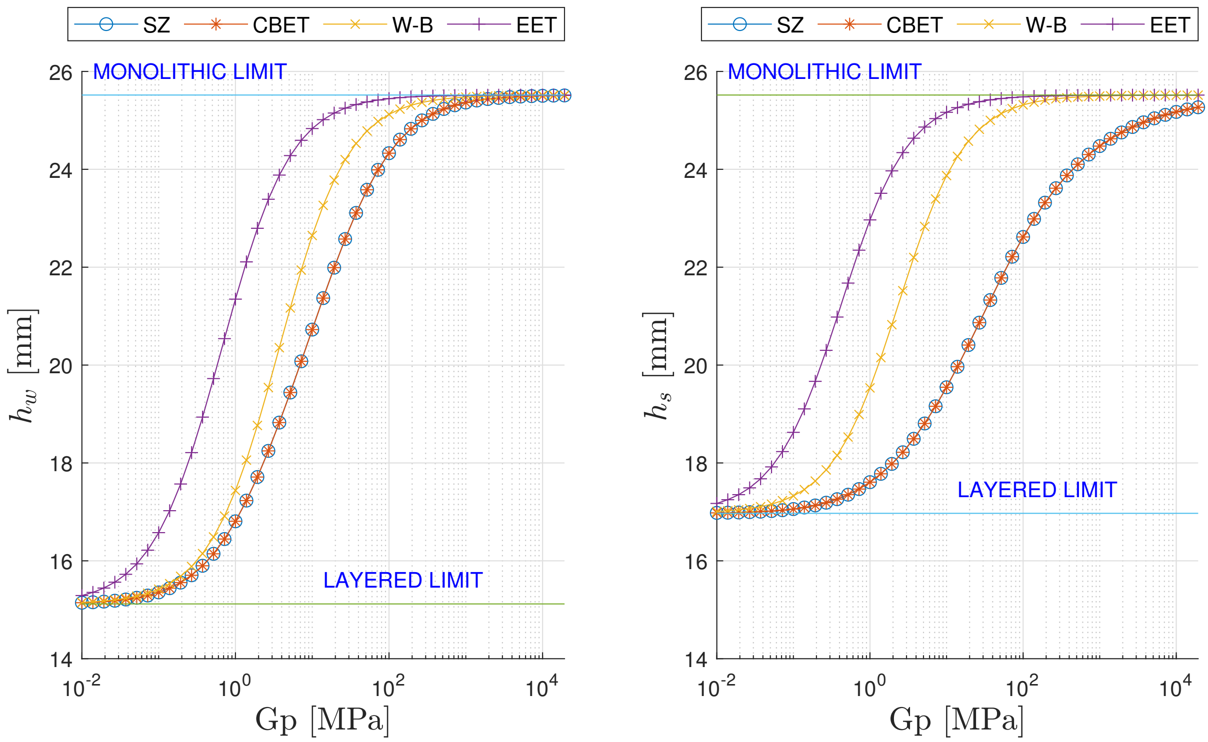

Figure 3.17: Deflection effective thickness h_w and stress effective thickness h_s of the laminated beam under concentrated tip force F. Graphs of comparison between the proposed approach (SZ), and other methods (CBET, W-B, ETT).

Recalling (3.20), this relationship is equivalent to

$$s^2\,\mathrm{Ig} + 2\,s\,\mathrm{Ig}_2 + \mathrm{Ig}_1 > 0\,, \quad \forall\, s \in \mathbb{R}\,. \tag{3.91}$$

Since $\mathrm{Ig} > 0$, this condition is satisfied for any given $s \in \mathbb{R}$ provided that the discriminant of the second-order algebraic equation in the variable s is negative, i.e.,

$$(2\,\mathrm{Ig}_2)^2 - 4\,\mathrm{Ig}\,\mathrm{Ig}_1 \; < \; 0\,, \tag{3.92}$$

which is the sought inequality $\mathrm{Ig}\,\mathrm{Ig}_1 > \; {\mathrm{Ig}_2}^2$.

Chapter 4

Thermal Analysis via Variational Principles

The interest in the thermal analysis of solids arises from the importance of thermally induced strain and stress in the structural and mechanical response of a given structure or structural element. When a structure is subject to "thermal loads" inducing temperature variations and consequent thermal strain, if the strains are incompatible with the constraints, the structure might undergo stress that is well beyond the material strength. Additionally, thermal stresses can arise due to uneven temperature distributions (thermal gradients) or differences in thermal expansion coefficients within a composite structure, causing differential expansion or contraction between its constituent components. This can produce an eigenstress state that might cause raptures, delamination, and cracking.

Understanding and managing thermal stress is important to ensure the structural integrity and longevity of materials subjected to varying thermal conditions, particularly in designing composites for applications that face thermal cycling or extreme temperatures, such as aerospace, automotive, and electronics industries, where durability and performance are key aspects. In this chapter, a review of methods and solutions utilized for the determination of temperature distribution in solids, with a specific concentration on the variational principles, will be presented.

4.1 Introduction

In the sequel, the thermoelastic problem is treated as an uncoupled problem [55], [56], where the thermal distribution in the body is considered independent of the stress and displacement fields. The stress and strain fields, which depend on the temperature distribution, may be determined *a posteriori* by treating the thermal strain as a (possibly time-dependent) applied action. Nevertheless, a fully coupled analysis of the thermoelastic problem is necessary when the thermal properties of the materials considered are less precise, as in geological materials; thus, the semicoupled approach is not guaranteed to be adequate, according to Carter *et al.* [56]. In this introduction, the general theory of heat conduction and its governing equations, as well as a brief review of thermal analysis via variational principles, are presented.

4.1.1 The Heat Conduction Equation

In this section, a summary of the mathematical foundation of heat conduction is presented, following the seminal book "Conduction of Heat in Solids" by Carslaw and Jaeger [57].

Heat flow occurs between parts of a body that have different temperatures, via three different mechanisms: conduction, convection, and radiation. Conduction is the process by which heat energy is transmitted through collisions between neighboring atoms or molecules, and mainly occurs in solids and liquids. In convection, heat is transferred by the relative motion of parts of the heated body, which primarily occurs in gases and liquids. In radiation, heat is transferred remotely by electromagnetic waves.

To illustrate, consider an isotropic plate bounded by two infinite planes, with a thickness d. The upper and lower surfaces are maintained at temperatures θ_0 and θ_1, with $\theta_0 > \theta_1$. If this condition is maintained long enough to reach a steady state, the quantity of heat flowing through the plate, Q, is proportional to the temperature difference across it. A mathematical expression for Q can be derived by imagining a cylinder with a cross-sectional area S, bounded by the plate surfaces and with its axis perpendicular to them. By assuming that the cylinder is located in the center of the plate, so that it may be assumed no heat is flowing across its lateral surface, the heat flowing through S during a time period t is equal to

$$Q = -\lambda \frac{(\theta_1 - \theta_0)St}{d}\,, \tag{4.1}$$

where λ is the thermal conductivity of the material from which the plate is made. In general, thermal conductivity is a function of temperature. Nonetheless, if the temperature variation is small, λ can be considered constant.

Define a coordinate system with axis x perpendicular to the surface of the plate and directed from the bottom surface to the upper surface, so that these are identified by $x = 0$ and $x = d$, respectively. Let, again, the bounding surfaces of the plate be isothermal surfaces, consequently, at steady state other isothermal surfaces will constitute parallel planes to the bounding surfaces, the problem can be modeled as 1-D. By considering the limit for $d \to 0$ and S to be a unit area, the heat flow per unit area q, i.e., the heat flux in the direction of increasing x, is defined as follows:

$$q = -\lambda \frac{d\theta}{dx}. \tag{4.2}$$

This may be generalized for any isothermal surface in a 3-D space, where the heat flux through a surface with outward normal $\mathbf{n}$ is

$$q = -\lambda \frac{\partial \theta}{\partial \mathbf{n}} . \tag{4.3}$$

In a solid body, the heat flux q is continuous. This may be easily demonstrated, following again [57], by considering, again, an infinitesimal cylinder with length d and cross-sectional area S. By denoting by q_1 and q_2 the heat flux across the plain surfaces of this cylinder, the heat flow into the cylinder is equal to $S(q_1 - q_2)$. By denoting by c the specific heat per unit volume of the considered material, and by θ the average temperature of the cylinder, the rate at which the infinitesimal cylinder gains heat is

$$c\, S d\dot{\theta} = S(q_1 - q_2) \,, \tag{4.4}$$

where Sd is the volume of the cylinder, and $\dot{()}$ indicates time differentiation. This corresponds to the *energy conservation* in the considered cylinder. As the thickness $d \to 0$, the fluxes $q_1 \to q_2$, *ergo*, the flux is continuous. Notice that discontinuous thermal properties in the body do not invalidate this argument: the only requirement is that these properties have finite values. Consequently, the heat flux is also continuous at the surface of separation between two media.

Furthermore, by setting now $d = \Delta x$, so that $q_1 = q(x)$ and $q_2 = q(x + \Delta x)$, and by taking the limit for $\Delta x \to 0$, eq. 4.4 may be rewritten as

$$c\dot{\theta} = -\lim_{\Delta x \to 0} \frac{q(x + \Delta x) - q(x)}{\Delta x} = -\frac{d\, q(x)}{d\, x} \,. \tag{4.5}$$

Consider, now, the full 3-D problem, and denote by $\mathbf{x} = (x, y, z)$ the position of the generic point P. Traditionally, the "elementary tetrahedron argument" [56] is used to demonstrate that knowing the values of heat fluxes at three mutually perpendicular planes meeting at a point is sufficient to calculate the flux passing through an arbitrarily oriented plane that intersects this point. From this, the heat flux through any surface, even if it is not isothermal, can be calculated. Denoting the heat flux vector by $\mathbf{q}(\mathbf{x}, t)$, whose components are the fluxes through surfaces parallel to the coordinate axes (x, y, z), the relationship between the rate of change of temperature $\theta(\mathbf{x}, t)$ along the coordinate axes and the flux vector is expressed by

$$\lambda \nabla \theta(\mathbf{x}, t) + \mathbf{q}(\mathbf{x}, t) = 0 \,, \tag{4.6}$$

that may be regarded ad the 3-D generalization of eq. (4.2). This is the *law of heat conduction*, also known as Fourier's law [58], stating that the rate of heat transfer through a material is proportional to the negative gradient in the temperature, and to the material thermal conductivity.

The mathematical derivation of the heat conduction equation follows from considering the energy balance in an infinitesimal parallelepiped, part of a solid, where no heat is generated nor dissipated. It may be demonstrated that this provides

$$\nabla \cdot \mathbf{q}(\mathbf{x}, t) + c\dot{\theta}(\mathbf{x}, t) = 0\,, \tag{4.7}$$

that is the 3-D counterpart of (4.5).

In the case of a homogeneous isotropic body, by substituting (4.6) in (4.7), one obtains the equation of heat conduction in a 3-D solid body

$$-\lambda\Delta\theta(\mathbf{x}, t) + c\dot{\theta}(\mathbf{x}, t) = 0\,, \tag{4.8}$$

that is a parabolic partial differential equation, relating the time dependence and the spatial distribution of the temperature field.

In some particular conditions, a *steady state* condition can be reached, where the temperature at any given point remains constant over time, and the amount of heat entering any region of the system is exactly balanced by the amount of heat leaving, i.e., no accumulation of heat occurs. In this case, eq. (4.8) reduces to the Laplace's equation

$$\Delta\theta(\mathbf{x}, t) = 0. \tag{4.9}$$

Consider now the case where heat is generated or absorbed in the solid, at a given rate $q^\sharp(\mathbf{x}, t)$ per unit volume. This might be the result of chemical or nuclear reaction, of electrical resistance heating, of external radiation into the region, or of still other causes [59]. In this case, the heat generated (or consumed) in the considered infinitesimal volume must be added (or subtracted) to the total heat flow into the volume to get the overall rate of heat addition. Consequently, the heat conduction equation becomes

$$-\lambda\Delta\theta(\mathbf{x}, t) + c\dot{\theta}(\mathbf{x}, t) = q^\sharp(\mathbf{x}, t). \tag{4.10}$$

At the steady state, i.e., when the time variation of temperature is nil, this equation reduces to the Poisson's equation

$$-\lambda\Delta\theta(\mathbf{x}, t) = q^\sharp(\mathbf{x}, t)\,. \tag{4.11}$$

In summary, the 3-D thermal problem in solids is governed by the heat conduction equation (4.10), which combines the conservation of energy (4.7) and Fourier's heat conduction equation (4.6). Any solution of these equations must satisfy the initial and boundary conditions. The initial condition on temperature can be an arbitrary spatial distribution at $t = 0$, defined as

$$\theta(\mathbf{x}, 0) = \bar{\theta}(\mathbf{x}). \tag{4.12}$$

On the other hand, the boundary conditions for the temperature field can be of different types [57], summarized as follows:

A. *Prescribed surface temperature (Dirichlet boundary condition)*: In this case, the temperature is specified at a portion of the domain's boundary $\partial\Omega$ or at the entire boundary. The prescribed temperature, denoted as $\bar{\theta}(\mathbf{x}, t)$, can be time-dependent.

$$\theta(\mathbf{x}, t) = \bar{\theta}(\mathbf{x}, t), \quad \forall \mathbf{x} \in \partial\Omega, \forall t. \tag{4.13}$$

This corresponds to a Dirichlet boundary condition for the heat conduction equation (4.10).

B. *Prescribed heat flux at the boundary (Neumann boundary condition)*: A heat flux $\bar{q}(\mathbf{x}, t)$, possibly time-dependent, is specified on (a portion of) the domain boundary. In this case, accounting for (4.3), the boundary condition is

$$-\lambda \frac{\partial \theta(\mathbf{x}, t)}{\partial \mathbf{n}} = \bar{q}(\mathbf{x}, t), \quad \forall \mathbf{x} \in \partial\Omega, \forall t\,, \tag{4.14}$$

where, again, $\mathbf{n}$ denotes the normal to the boundary surface. Condition (4.14) corresponds to a Neumann boundary condition for the heat conduction equation (4.10). This includes, as a particular case, the case of an insulated boundary, preventing the heat flux, so that $\bar{q}(\mathbf{x}, t) = 0$.

C. *Linear convective heat transfer (Robin boundary condition)*: In this condition, the flux across a surface is proportional to the temperature difference between the boundary and the surrounding medium. This is the most common boundary condition for thermal problems, also known as *Newton's law of cooling* [60]. This occurs when forced convection is present, i.e., a fluid at a temperature θ_e is forced to flow quickly on the boundary of the solid, or when a layer of poor heat conductor, like scale, grease, or oxide, is present on the surface of the solid. The boundary condition is expressed as

$$-\lambda \frac{\partial \theta(\mathbf{x}, t)}{\partial \mathbf{n}} = h[\theta(\mathbf{x}, t) - \theta_e(\mathbf{x}, t)], \quad \forall \mathbf{x} \in \partial\Omega, \forall t\,. \tag{4.15}$$

Here, $\theta_e(\mathbf{x}, t)$ is the temperature of the surrounding medium, and h is the convective surface heat transfer coefficient, so that the right-hand side of (4.15) represents the convective heat exchange at the domain boundary.

If an additional heat flux $\bar{q}(\mathbf{x}, t)$ is prescribed at the boundary, (4.15) becomes

$$-\lambda \frac{\partial \theta(\mathbf{x},t)}{\partial \mathbf{n}} = h[\theta(\mathbf{x},t) - \theta_e(\mathbf{x},t)] + \bar{q}(\mathbf{x},t), \quad \forall \mathbf{x} \in \partial\Omega, \forall t. \tag{4.16}$$

This boundary condition reduces to a boundary condition of type B when $h \to 0$, and to a condition of type A when $h \to \infty$.

D. *Non-linear heat transfer*: This boundary condition comprises the case of black body radiation, where the heat flux from the boundary at absolute temperature $\theta(\mathbf{x},t)$ to a black body at temperature θ_0 is

$$-\lambda \frac{\partial \theta(\mathbf{x},t)}{\partial \mathbf{n}} = \sigma\varepsilon[\theta(\mathbf{x},t)^4 - \theta_0(t)^4], \quad \forall \mathbf{x} \in \partial\Omega, \forall t\,, \tag{4.17}$$

where σ is the Stefan-Boltzmann constant, and ε is the material's emissivity. If the difference between $\theta(\mathbf{x},t)$ and $\theta_0(t)$ is small compared to their mean value, condition (4.17) may be approximated as a condition of type C.

Non-linear heat transfer also occurs when a body is surrounded by a fluid undergoing natural convection, caused by the heating of the fluid near the body, which makes the warmer portion rise and be replaced by a cooler portion. The heat flux due to natural convection from a boundary to a fluid at a temperature θ_0 is

$$-\lambda \frac{\partial \theta(\mathbf{x},t)}{\partial \mathbf{n}} = k\,[\theta(\mathbf{x},t) - \theta_0]^{5/4}, \quad \forall \mathbf{x} \in \partial\Omega, \forall t, , \tag{4.18}$$

where k is a constant that depends on the nature of the fluid.

E. *Interface between two media with different thermal conductivities*: The continuity of heat flux has been proven based on the energy conservation argument (4.4). Consequently, at the interface $\partial\Omega_s$ between two materials with different thermal conductivities $\lambda_1 \neq \lambda_2$, at temperatures $\theta_1(\mathbf{x},t)$ and $\theta_2(\mathbf{x},t)$, respectively, the following condition holds

$$\lambda_1\, \frac{\partial \theta_1(\mathbf{x},t)}{\partial \mathbf{n}} = \lambda_2\, \frac{\partial \theta_2(\mathbf{x},t)}{\partial \mathbf{n}}, \quad \forall \mathbf{x} \in \partial\Omega_s, \forall t. \tag{4.19}$$

Note that the continuity of temperature at the interface can be assumed in the case of perfect contact, as in soldered joints or laminated glass (where strong bonding between the glass and polymer layers is achieved in an autoclave, due to the chemical affinity between the hydroxyl groups of the polymer and the silanol groups on the glass surface). In such cases, in addition to the condition (4.19), the temperature is continuous at the bi-material interface, i.e.,

$$\theta_1(\mathbf{x},t) = \theta_2(\mathbf{x},t), \quad \forall \mathbf{x} \in \partial\Omega_s, \forall t. \tag{4.20}$$

On the contrary, when the bonding between the two materials cannot be considered perfect, the condition at the interface should be of type C or type D. For the case where the heat transfer at the interface is approximated by a linear relationship one gets

$$-\lambda_1 \frac{\partial \theta_1(\mathbf{x},t)}{\partial \mathbf{n}} = -\lambda_2 \frac{\partial \theta_2(\mathbf{x},t)}{\partial \mathbf{n}} = \tilde{h}(\theta_1(\mathbf{x},t) - \theta_2(\mathbf{x},t)), \quad \forall \mathbf{x} \in \partial\Omega_s, \forall t\,, \tag{4.21}$$

where $\tilde{h}$ is a measure of the interfacial thermal impedance, representing the constant of proportionality between the heat flux and the temperature jump at the interface, and it depends on the nature of the materials in contact and on the amount of pressure applied to achieve the contact. However, regardless of what is the condition on temperature, the continuity of heat flux at the interface (4.19) holds.

F. *Interfacial thermal resistance (ITR), i.e., Kapitza resistance*: Interfacial thermal resistance was discovered by P. L. Kapitza in the 1940s [61], while studying the capillary flow of Helium II. This phenomenon involves a thermal impedance at the surface of contact between two materials, arising from the combination of poor mechanical or chemical adherence at the interface and/or thermal expansion mismatch—phenomena that can be encountered in composite materials [62]–[64]. Contrary to the phenomena described in conditions of type E, this impedance occurs even when a perfect bonding between the materials is present. ITR is generally more significant for solid-gas and solid-liquid interfaces than for solid-solid interfaces [65].

Many models have been proposed to interpret the ITR, such as the acoustic mismatch model [66], which attributes this phenomenon to an increased probability of phonon reflection at the interface due to the acoustic mismatch between the solid and the surrounding fluid. The ITR has also been observed at the interface between dissimilar solids at low temperatures [67], concluding that this phenomenon does not significantly affect heat transfer unless the densities or acoustic velocities in the considered media are highly different.

The result is a jump in the temperature profile, proportional to the heat flux normal to the interface, providing an interface condition whose mathematical expression is formally similar to the condition of type F (4.21).

$$-\lambda_1 \frac{\partial \theta_1(\mathbf{x},t)}{\partial \mathbf{n}} = -\lambda_2 \frac{\partial \theta_2(\mathbf{x},t)}{\partial \mathbf{n}} = \frac{1}{R}(\theta_1(\mathbf{x},t) - \theta_2(\mathbf{x},t)), \quad \forall \mathbf{x} \in \partial\Omega_s, \forall t. \tag{4.22}$$

where R is the thermal impedance coefficient, dependent on the properties of the media in contact.

4.1.2 Thermal Analysis Via Variational Principles

After having gone through the foundations of the mathematical theory of heat conduction, a brief review of variational methods in heat conduction is presented hereafter. Due to the large number and broad scope of variational principles in heat conduction, this review cannot be considered exhaustive: the aim is to illustrate the historical context in which the author's contribution to variational principles in heat conduction is situated.

Based on the principle of microscopic reversibility applied to fluctuations, Onsager [68], [69] derived a set of reciprocal relationships for heat conduction in an anisotropic medium. These relationships can be expressed in terms of a potential, allowing for the formulation of the minimum dissipation variational principle, in which this potential is a generalization of the dissipation function introduced by Rayleigh [70]. The dissipation function equals half the rate of production of irreversible entropy generated in a volume due to heat flow across that volume.

Another variational principle for heat conduction was suggested by Rosen [71], where a new dissipation function was introduced, resulting in a simple variational principle for unsteady heat flow in isotropic media. In this work, the variation of the dissipation function with respect to heat flux, under the constraint of energy conservation, resulted in the Fourier equation. Subsequently, the temperature was varied while keeping the heat flux constant, allowing the formulation of a variational principle where temperature is the only quantity subjected to variations. On the other hand, Chambers [72] has proven the existence of a variational principle in heat conduction, where only the time derivative of temperature is varied.

Biot developed an ingenious variational approach to heat conduction [73], based on the original concept of a *heat displacement* field. An extension to Biot's variational principle was developed by Nigam and Agrawal [74], by considering the transient heat transfer in fluids under forced flow, including the heat generated by viscous dissipation. A more general variational principle was developed by Sparrow *et al.* [75] for steady-state laminar heat transfer in ducts. A variety of variational principles were derived for heat conduction with temperature-dependent material properties [60], [76], [77]. In the next section, a detailed presentation of Biot's variational principle is provided to illustrate the foundations on which the novel variational principle is built.

4.2 The Approach by Biot

The ingenious approach by Biot [73] relies on the introduction of the *heat displacement* vector field, whose time derivative is the heat flux field. This allows for the definition of a fundamental variational principle, in which the temperature and the heat displacement field are work-conjugated, similarly to force and displacement in mechanics.

Biot's variational principle corresponds to the weak form of Fourier's equation (4.6), where the energy conservation law (4.7) serves as a constraint . This means that the heat conduction law is verified approximately, while energy conservation is rigorously satisfied at each time and each point. In particular, the conservation of energy is identically verified by the choice of generalized coordinates, analogous to holonomic constraints in mechanics.

This variational principle extends the principles of virtual works and generalized forces to thermodynamics. Notably, the fundamental variational principle does not contain the spatial derivatives of temperature field; this enhances the accuracy of approximate solutions, particularly in scenarios with significant temperature gradients. By representing the heat displacement field with generalized coordinates, one can derive Lagrangian-type equations analogous to those in mechanics, utilizing potentials, generalized forces, and a Rayleigh-type dissipation function. It is important to highlight that, in the context of anisotropic thermal properties, the definition of the dissipation function is grounded in the reciprocity relations introduced by Onsager [69].

4.2.1 The Classical Variational Principle

The heat displacement field $\mathbf{H}(\mathbf{x}, t)$ is defined such that its time derivative $\dot{\mathbf{H}}(\mathbf{x}, t)$ corresponds to the local rate of heat flow per unit area $\mathbf{q}(\mathbf{x}, t)$. By recalling (4.6), the heat displacement field is defined, as a function of the temperature field $\theta(\mathbf{x}, t)$ and the thermal conductivity λ, by

$$\mathbf{H}(\mathbf{x}, t) = -\int_0^t \lambda \, \nabla\theta(\mathbf{x}, t) \,, \tag{4.23}$$

Denoting, again, by c the heat capacity per unit volume, the energy conservation (4.7) can be written in terms of the "excess temperature" $\theta(\mathbf{x}, t)$, over an equilibrium temperature $\theta_0(\mathbf{x})$ giving:

$$c\theta(\mathbf{x}, t) = -\nabla \cdot \mathbf{H}(\mathbf{x}, t) \,. \tag{4.24}$$

Notice that this relation does not involve any time derivative and may be regarded as a holonomic constraint in the sense of classical mechanics. Furthermore, the heat displacements will be defined up to an additive time-independent solenoidal vector field; however, this indeterminacy is inessential in the solution of the thermal problem. This form of energy conservation is also verified by the variation of the heat displacement $\delta\mathbf{H}(\mathbf{x}, t)$ and the variation of temperature $\delta\theta(\mathbf{x}, t)$, i.e.,

$$c \; \delta\theta(\mathbf{x}, t) = -\nabla \cdot \delta\mathbf{H}(\mathbf{x}, t). \tag{4.25}$$

Based on the definition of the heat displacement field, and denoting again the (constant and uniform) thermal conductivity by λ, the law of heat conduction (4.6) can be written as

$$\lambda\nabla\theta(\mathbf{x}, t) + \dot{\mathbf{H}}(\mathbf{x}, t) = 0. \tag{4.26}$$

The Biot's variational principle corresponds to the weak form of the heat conduction equation (4.26), i.e., it is obtained by multiplying (4.26) by δH, and by integrating by parts over the volume Ω, accounting for (4.25). Notice that, in such a way, the contribution of $\theta_0(\mathbf{x}, t)$ is lost. By omitting, hereafter, the dependence of the variables on space and time, for the sake of brevity, this reads

$$\int_\Omega c\,\theta\,\delta\theta dV + \int_\Omega \frac{1}{\lambda}\,\dot{\mathbf{H}}\cdot\delta\mathbf{H}dV = -\int_{\partial\Omega}\theta\,\delta\mathbf{H}\cdot\mathbf{n}\,ds\,, \tag{4.27}$$

where, again, $\mathbf{n}$ is the outward normal to the surface.

Biot then defined the *thermal potential* $\mathcal{V}$ as

$$\mathcal{V} = \frac{1}{2}\int_\Omega c\theta^2\,dV\,, \tag{4.28}$$

and the variational invariant $\delta\mathcal{D}$, related to the concept of *dissipation function*, as

$$\delta\mathcal{D} = \int_\Omega \frac{1}{\lambda}\,\dot{\mathbf{H}}\cdot\delta\mathbf{H}\,dV. \tag{4.29}$$

The relationship between the invariant $\delta\mathcal{D}$ to the dissipation function will be clarified later on, when introducing the generalized coordinates.

The right-hand side of (4.27) is interpreted as *thermal driving forces*

$$\delta\mathcal{Q} = -\int_{\partial\Omega}\theta\delta\mathbf{H}\cdot\mathbf{n}\,ds\,. \tag{4.30}$$

The contribution (4.30) was interpreted by Biot as the equivalent of the virtual work done by a pressure θ on a volume inflow of fluid $\mathbf{n}\cdot\delta\mathbf{H}$. After substituting (4.32) into the variational principle (4.27), it may be rewritten as

$$\delta\mathcal{V} + \delta\mathcal{D} = \delta\mathcal{Q}\,. \tag{4.31}$$

As highlighted in [78], a major drawback of the variational principle (4.27) is the coexistence of variations of the temperature and the displacement field.

The displacement field $\mathbf{H}(\mathbf{x}, t)$ can be linearly represented as a sum of a number n of "fixed configurations" $\mathbf{N}(\mathbf{x})$, with a variable amplitude identified by a set of n time-dependent *generalized coordinates* $\mathbf{f}(t)$, in the form

$$\mathbf{H}(\mathbf{x}, t) = \mathbf{N}(\mathbf{x})\cdot\mathbf{f}(t)\,. \tag{4.32}$$

In the more general case, these coordinates need not be related linearly to $\mathbf{H}(\mathbf{x}, t)$, i.e., $\mathbf{N}(\mathbf{x})$ may depend on time. This representation (4.32) includes, as a particular case, the Fourier series and expansions in orthogonal functions. It can be readily deduced from this representation that

$$\frac{\partial \dot{\mathbf{H}}}{\partial \dot{f}_i} = \frac{\partial \mathbf{H}}{\partial f_i} \,. \tag{4.33}$$

Consequently, the variational invariant (4.29) can be interpreted as a variation of a *dissipation function*, defined as

$$\mathcal{D} = \frac{1}{2} \int_{\Omega} \frac{1}{\lambda} \, \dot{\mathbf{H}}^2 \, dV. \tag{4.34}$$

The representation (4.32) allows to rewrite the variational principle (4.27) as a set of n Lagrangian equations in the form

$$\frac{\partial \mathcal{V}}{\partial f_i} + \frac{\partial \mathcal{D}}{\partial \dot{f}_i} = \mathcal{Q}_i \,, \tag{4.35}$$

where $\mathcal{Q}_i = -\int_{\partial\Omega} \theta \; \mathbf{n} \cdot (\partial \mathbf{H}/\partial f_i) \, ds$.

These equations are analogous to the Lagrangian equations for the slow motion of dissipative systems with negligible inertia forces. Any solution of (4.35) that satisfies the boundary conditions will yield the temperature distribution. The heat displacement can be determined up to an additive function, which depends upon the boundary conditions. This indeterminacy, though inessential, is congenital in Biot's variational principle.

4.2.2 Heat Sources

In the classical approach by Biot, the rate of heat generation $q^\sharp(\mathbf{x}, t)$ (see eq. (4.10)) in the generic volume Ω is represented using a *fictitious* heat displacement field $\mathbf{H}^*$, defined by

$$\nabla \cdot \mathbf{H}^* = \int_0^t q^\sharp dt \,. \tag{4.36}$$

Notice that $\mathbf{H}^*$, which can be considered as a given function of time and coordinates, is defined up to an additive time-independent solenoidal vector field. Nonetheless, this indeterminacy has no effect on the solution.

Define a new heat displacement field $\mathbf{H}$, represented by the superposition of two separate fields

$$\mathbf{H} = \mathbf{H}^{+} + \mathbf{H}^{*}\,, \tag{4.37}$$

where $\mathbf{H}^{+}$ is the part of the heat displacement related to the temperature field by the energy conservation law (4.24), i.e.,

$$-\nabla \cdot \mathbf{H}^{+} = c\theta\,, \tag{4.38}$$

while Fourier's law is written as

$$\lambda \nabla \theta + \dot{\mathbf{H}}^{+} + \dot{\mathbf{H}}^{*} = 0\,. \tag{4.39}$$

This allows to generalize the variational principle (4.27) to the case of bodies with the presence of heat generation, in the form

$$\int_{\Omega} \theta\ \delta\theta dV + \int_{\Omega} \frac{1}{\lambda}\ \dot{\mathbf{H}}^{+}\ \delta\mathbf{H}^{+} = -\int_{\Omega} \frac{1}{\lambda}\ \dot{\mathbf{H}}^{*}\ \delta\mathbf{H}^{+} - \int_{\partial\Omega} \theta\ \delta\mathbf{H}^{+} \cdot \mathbf{n} ds\,, \tag{4.40}$$

where the right-hand side accounts for the thermal driving force and the generated heat.

Notice that the field $\mathbf{H}^{+}$ is a fictitious field, not directly correlated to the heat flux. For this reason, a better definition that preserves the physical meaning of the heat displacement field related to heat generation will be presented in Sect. 4.3, describing the novel variational principle suggested by the author.

4.2.3 Boundary Conditions

The boundary conditions for the thermal problem are listed in section 4.1.1. Here, a brief description of how these may be considered in the framework of the classical variational principle by Biot is presented.

- *Boundary conditions of type A* (eq. (4.13)) are accounted for as natural boundary conditions simply by substituting the known temperature on the boundary in the thermal driving force term (4.30). Similar to the mechanical problem, when a natural boundary condition is specified on the boundary, the displacement $\delta\mathbf{H} \cdot \mathbf{n}$ is not constrained at the boundary.
- *Boundary conditions of type B*: in this case, a normal heat flux $\dot{\bar{\mathbf{H}}}_n$ is assigned on the boundary. Boundary condition (4.14) may be written as

$$-\lambda \frac{\partial \theta}{\partial \mathbf{n}} = \dot{\bar{\mathbf{H}}}_n = \bar{q}\,, \forall \mathbf{x} \in \partial\Omega, \forall t\,. \tag{4.41}$$

This condition can be integrated in time to get the geometrical boundary condition $\mathbf{H} \cdot \mathbf{n} = \bar{\mathbf{H}}_n$, which can be enforced in a variety of ways, depending on the solution procedure. For instance, if the equations are solved by means of a finite element approximation, where degrees of freedom correspond to the nodal heat displacements, (4.61) can be represented by substituting the prescribed values of heat displacement in the corresponding degrees of freedom, or by using Lagrange multipliers in the case of miscellaneous constraints.

- *Boundary conditions of type C.* For this common case, an analytical treatment allowing for the incorporation of this condition into the classical variational principle was proposed by Biot [79]. This may be done by expressing the boundary temperature θ equation(4.15) as a function of the normal heat flux $\dot{\mathbf{H}}$ and of the temperature of the surrounding medium θ_e, as

$$\theta = \frac{1}{h}\dot{\mathbf{H}}_n + \theta_e. \tag{4.42}$$

By substituting (4.42) in (4.30), the expression for the thermal driving force term can be rewritten as

$$\delta\mathcal{Q} = -\int_{\partial\Omega} \frac{1}{h}\dot{\mathbf{H}}\delta\mathbf{H} \cdot \mathbf{n} ds - \int_{\partial\Omega} \theta_e \; \mathbf{n} \cdot \delta\mathbf{H} ds\,. \tag{4.43}$$

By considering the linear representation of the displacement field $\mathbf{H}$ as in (4.32), and the related expression for the variational principle (4.35), the vector of the thermal driving forces may be split into two different terms, in the form

$$\mathcal{Q}_i = -\int_{\partial\Omega} \frac{1}{h}\; \dot{\mathbf{H}}\frac{\partial \mathbf{H}}{\partial f_i}\; ds \; - \int_{\partial\Omega} \theta_e \; \mathbf{n} \cdot \frac{\partial \mathbf{H}}{\partial f_i} ds\,. \tag{4.44}$$

The first contribution may be regarded as the variation of a *boundary dissipation function* $\mathcal{D}_b$, accounting for the boundary heat transfer, defined as

$$\mathcal{D}_b = \frac{1}{2}\int_{\partial\Omega} \frac{1}{h}\; \dot{\mathbf{H}}_n^2 ds\,, \tag{4.45}$$

while the second contribution in (4.44) represents a *boundary thermal driving force*, denoted as $\delta\mathcal{Q}_{ib} = \int_{\partial\Omega} \theta_e \; \mathbf{n} \cdot (\partial\mathbf{H}/\partial f_i)\; ds$.

The variational principle, with embedded boundary condition of type C, can hence be written in the following form:

$$\frac{\partial \mathcal{V}}{\partial f_i} + \frac{\partial \mathcal{D}_b}{\partial \dot{f}_i} + \frac{\partial \mathcal{D}}{\partial \dot{f}_i} = \mathcal{Q}_{ib}\,. \tag{4.46}$$

From the point of view of the variational principle, there is no difference between this boundary condition and the one of type F.

The classical variational principle by Biot didn't address the non-linear boundary conditions of type D; nonetheless, they were incorporated later on by Lardner [60].

4.3 A Novel Neat Flux-Based Weak Formulation

Relying on Biot's concept of the heat displacement field, the author has proposed a novel variational principle [78]. The main difference with respect to the classical Biot's principle presented in Sect. 4.2 lies in the role of the governing equations. Indeed, here the energy conservation is used as a field equation, and Fourier's law is incorporated as a holonomic constraint in the weak form of energy conservation, where the displacement field is the only varied quantity. Hence, the name "neat".

In contrast to the classical Biot's approach described in the previous section, this will not consider an "excess temperature", but the initial, arbitrary, temperature field $\theta_0(\mathbf{x}) = \theta(\mathbf{x}, t = 0)$ is directly included in the variational formulation. The fact that only the heat displacement is varied enables the development of an approximate method, based on the description of the field through generalized coordinates, allowing for the development of a numerical approach entailing the use of a simple isoparametric linear finite element.

4.3.1 The Neat Variational Approach

Here, the notation and the governing equations of the neat variational principle are presented. Consider the general case of a body with thermal conductivity λ and specific heat c, with generated/absorbed heat per unit volume and unit time denoted again by $q^\sharp(\mathbf{x}, t)$. Define, in this general case, the *total* heat displacement $\mathbf{H}(\mathbf{x}, t)$ through Fourier's law, as

$$\lambda \nabla\theta + \dot{\mathbf{H}} = 0 \quad \Rightarrow \quad \mathbf{H} = -\int_0^t \lambda \, \nabla\theta \; dt \,, \tag{4.47}$$

for which the value at $t = 0$ can be assumed to be null, without loss of generality. Again, the dependence of the variables on space and time is here omitted, for the sake of brevity. Energy conservation provides, for a sub-body $\mathcal{B} \in \Omega$ with outer normal $\mathbf{n}$,

$$-\int_{\partial\mathcal{B}} \dot{\mathbf{H}} \cdot \mathbf{n} \; ds + \int_{\mathcal{B}} q^\sharp \; dV = \int_{\mathcal{B}} c\dot{\theta} \; dV \,. \tag{4.48}$$

Integrating (4.48) by parts, since the sub-body $\mathcal{B} \in \Omega$ is arbitrary, the local form of energy conservation can be written as

$$-\nabla \cdot \dot{\mathbf{H}} + q^\sharp = c\,\dot{\theta} \,. \tag{4.49}$$

Following Biot, a fictitious heat flux $\dot{\mathbf{H}}^\sharp(\mathbf{x}, t)$ associated to $q^\sharp(\mathbf{x}, t)$, is defined as

$$\int_{\mathcal{B}} q^\sharp dV = -\int_{\partial\mathcal{B}} \dot{\mathbf{H}}^\sharp \cdot \mathbf{n}\, ds \quad \Rightarrow \quad \nabla \cdot \dot{\mathbf{H}}^\sharp = -q^\sharp\,, \tag{4.50}$$

and the related heat displacement field, hence defined as

$$\nabla \cdot \mathbf{H}^\sharp = -\int_0^t q^\sharp\; dt\,. \tag{4.51}$$

By integrating (4.49) in time, and accounting for definition (4.51), the integral and local form of the energy conservation, not containing any time derivative, is obtained

$$-\nabla \cdot \left[\mathbf{H} + \mathbf{H}^\sharp\right] = c\,[\theta - \theta_0]\;, \tag{4.52}$$

The neat variational principle corresponds to the weak form of the energy conservation (4.52), i.e., it is obtained by multiplying (4.52) by the variation $\nabla \cdot \delta\mathbf{H}$, and by integrating it over the domain Ω:

$$\int_\Omega \;[\theta - \theta_0]\,\nabla \cdot \delta\mathbf{H}\; dV + \int_\Omega \frac{1}{c}\;\nabla \cdot \left[\mathbf{H} + \mathbf{H}^\sharp\right]\;\nabla \cdot \delta\mathbf{H}\; dV = 0\,. \tag{4.53}$$

By using the divergence theorem on the first term, and by accounting for Fourier's law (4.47), the weak form (4.53) may be rearranged in the form

$$\begin{aligned}\int_\Omega \frac{1}{c}\;\nabla \cdot \mathbf{H}\;\nabla \cdot \delta\mathbf{H}\; dV + \int_\Omega \frac{1}{\lambda}\;\dot{\mathbf{H}} \cdot \delta\mathbf{H}\; dV = \\ -\int_{\partial\Omega} \theta\delta\mathbf{H} \cdot \mathbf{n}\; ds + \int_\Omega \theta_0 \nabla \cdot \delta\mathbf{H}\; dV - \int_\Omega \frac{1}{c}\;\nabla \cdot \mathbf{H}^\sharp\;\nabla \cdot \delta\mathbf{H}\; dV\,.\end{aligned} \tag{4.54}$$

The terms appearing on the right-hand side of (4.54) represent the thermal driving forces. In particular, the first accounts for the effect of the temperature distribution at the domain boundaries, the second indicates the contribution due to the initial temperature distribution, while the latter is related to the energy generated in the volume.

The field $\mathbf{H}$ is required to be at least C^0 continuous, and its variation $\delta\mathbf{H}$ must satisfy the geometrical boundary conditions. Notice that, in (4.54), only the divergence of $\mathbf{H}^\sharp$ appears, indicating the quantity of heat generated or absorbed up to the current moment (4.51). The variational principle can be expressed in a clearer way by applying the divergence theorem to (4.54), providing

$$\int_{\Omega} \left\{ -\frac{1}{c}\nabla \left[\nabla \cdot \left[\mathbf{H} + \mathbf{H}^{\sharp}\right]\right] + \frac{1}{\lambda}\dot{\mathbf{H}} + \nabla\theta_0 \right\} \cdot \delta\mathbf{H} \; dV \\ + \int_{\partial\Omega} \left\{ \theta - \theta_0 + \frac{1}{c}\nabla \cdot \left[\mathbf{H} + \mathbf{H}^{\sharp}\right] \right\} \delta\mathbf{H} \cdot \mathbf{n} \; ds = 0\,. \quad (4.55)$$

Remarkably, only the variation of heat displacement is present, and the temperature is included only in the boundary term. The variation $\delta\mathbf{H}$ is arbitrary; therefore, the strong form of the governing equation is

$$\frac{1}{\lambda}\,\dot{\mathbf{H}} = \nabla \left[\frac{1}{c}\nabla \cdot \left[\mathbf{H} + \mathbf{H}^{\sharp}\right] - \theta_0 \right]\,. \quad (4.56)$$

Once the heat displacement field is found by solving the governing equation with appropriate boundary conditions, the temperature field can be obtained *a posteriori* from the holonomic constraint (4.47). Therefore, any heat displacement and temperature fields must satisfy

$$-\nabla\theta = \nabla \left[\frac{1}{c}\nabla \cdot \left[\mathbf{H} + \mathbf{H}^{\sharp}\right] - \theta_0 \right]\,. \quad (4.57)$$

This implies that the quantity

$$\theta - \theta_0 + \frac{1}{c}\nabla \cdot \left[\mathbf{H} + \mathbf{H}^{\sharp}\right] = F(t) \quad (4.58)$$

is a function of time only, because its gradient is null in the whole domain.

When the variation $\delta\mathbf{H} \cdot \mathbf{n}$ is not zero on a part $\partial_p\Omega$ of the boundary $\partial\Omega$, the natural boundary condition provided by the boundary term of (4.55) readily implies that

$$\theta - \theta_0 + \frac{1}{c}\nabla \cdot \left[\mathbf{H} + \mathbf{H}^{\sharp}\right] = F(t) = 0\,. \quad (4.59)$$

Therefore, one obtains $F(t) = 0$ in the whole domain Ω and, consequently,

$$\theta - \theta_0 + \frac{1}{c}\nabla \cdot \left[\mathbf{H} + \mathbf{H}^{\sharp}\right] = 0\,. \quad (4.60)$$

This is the energy conservation law (4.52). The case in which $\delta\mathbf{H} \cdot \mathbf{n} = 0$ on the whole boundary $\partial\Omega$ deserves a particular attention, because it entails an intrinsic indeterminacy in the temperature field $\theta - \theta_0$.

4.3.2 Boundary Conditions in the "Neat" Principle

Boundary conditions of type A, B, and C may be managed, in the neat variational principle, in a manner analogous to that described in Sect. 4.2.3 for the classical Biot's principle. In particular, for conditions of type C, the linear heat transfer between the body and the surrounding medium with assigned temperature was incorporated using a boundary dissipation function [78]. However, there are two exceptions, that deserve a particular attention:

- Where *boundary conditions of type B are prescribed on the whole boundary*, i.e.,

  $$\dot{\mathbf{H}}_n = \bar{q}\,, \forall \mathbf{x} \in \partial\Omega, \forall t\,, \tag{4.61}$$

  and $\delta\mathbf{H}\cdot\mathbf{n} = 0$ on the whole boundary $\partial\Omega$.

  In this case, the whole heat displacement field is found by solving the variational problem. However, there is an intrinsic indeterminacy in the temperature field: a uniform temperature field can be added to the solution without invalidating the constraint. The only way to resolve this indeterminacy is by using the conservation of energy on a part of the boundary, even if it is not the natural boundary condition in the variational principle.

- *Boundary conditions of type E or type F* may be treated in a manner similar to type C. In particular, from the analytical point of view, the only difference between the condition of type C and types E and F is that the temperature on both sides of the interface is unknown. Here, the incorporation of these kinds of conditions in the neat variational principle is presented.

  Consider a smooth surface of separation $\partial\Omega_s$. Introduce a local orthogonal curvilinear system of coordinates (ξ, η, ζ), with arc-length parametrization, such that $\partial\Omega_s$ corresponds to $\zeta = 0$, the axis ζ is orthogonal to $\partial\Omega_s$, whereas the axes associated with ξ and η are tangent to $\partial\Omega_s$. The heat flux across the interface in the direction of ζ is

  $$\dot{H}_\zeta(\xi, \eta, 0, t) = -\Gamma\left[\theta(\xi, \eta, 0^+, t) - \theta(\xi, \eta, 0^-, t)\right]\,, \tag{4.62}$$

  where Γ can be either equal to $\tilde{h}$ from equation (4.21) or to $1/R$ from equation (4.22), while $\theta(\xi, \eta, 0^\pm, t)$ represents the temperatures on the two sides of the interface.

  In the proposed approach, this contribution affects the dissipation term in (4.54), i.e., the one where the coefficient $1/\lambda$ appears. One can interpret the resistant interface as a thermally *anisotropic* ply, as per [79], of very small thickness $\Delta\zeta$, i.e., $\zeta \in (-\Delta\zeta/2, \Delta\zeta/2)$, and very low thermal conductivity λ_ζ in the ζ direction. There are no internal heat sources; no heat is stored[1], so that the heat fluxes, assuming that $\Delta\zeta$ is very small, are uniform in the ζ

[1] This is equivalent [80] to assuming that $c = 0$ in (4.49).

direction. Consequently, from (4.47), the temperature is linearly distributed in the thickness.

Consider now the limit for $\Delta\zeta \to 0$ and $\lambda_\zeta \to 0$, while $\Delta\zeta/\lambda_\zeta \to \frac{1}{\Gamma}$. Therefore, the contribution in the dissipative term of (4.54) reads

$$\lim_{\Delta\zeta\to 0} \frac{1}{\lambda_\zeta} \int_{\partial\Omega_s} \int_{-\Delta\zeta/2}^{\Delta\zeta/2} \dot{H}_\zeta(\xi,\eta,\zeta,t)\,\delta H_\zeta \;d\zeta\;dA = \frac{1}{\Gamma} \int_{\partial\Omega_s} \dot{H}_\zeta(\xi,\eta,0,t)\,\delta H_\zeta \;dA\,. \tag{4.63}$$

The numerical implementation of this type of interface conditions will be reported later on.

4.3.3 Comparison with Biot's Approach

Here, the similarities and differences between the neat, and the classical variational principle by Biot, presented in Sect. 4.2, are discussed.

Mechanical interpretation of the neat principle

The variational principle (4.54) can be expressed in compact form as

$$\delta\mathcal{V}_H + \delta\mathcal{D} = \delta\mathcal{Q} + \delta\mathcal{Q}_0 + \delta\mathcal{Q}^\sharp\,, \tag{4.64}$$

where, in analogy with the Biot's definitions of thermal potential (4.28) and variation of dissipation function (4.29), $\mathcal{V}_H$ and $\delta\mathcal{D}$ are defined as

$$\delta\mathcal{V}_H := \int_\Omega \frac{1}{c}\;\nabla\cdot\mathbf{H}\;\nabla\cdot\delta\mathbf{H}\;dV\,, \tag{4.65a}$$

$$\delta\mathcal{D} = \int_\Omega \frac{1}{\lambda}\;\dot{\mathbf{H}}\;\delta\mathbf{H}\;dV\,. \tag{4.65b}$$

On the other hand, the thermal driving forces appearing on the right-hand side of (4.64) are given by

$$\delta\mathcal{Q} := -\int_{\partial\Omega} \theta\;\delta\mathbf{H}\cdot\mathbf{n}\;ds\,, \tag{4.66a}$$

$$\delta\mathcal{Q}_0 := \int_\Omega \theta_0\nabla\cdot\delta\mathbf{H}\;dV\,, \tag{4.66b}$$

$$\delta\mathcal{Q}^\sharp := -\int_\Omega \frac{1}{c}\;\nabla\cdot\mathbf{H}^\sharp\;\nabla\cdot\delta\mathbf{H}\;dV\,. \tag{4.66c}$$

These account for the effects of initial temperature distribution ($\delta\mathcal{Q}_0$), the energy generated in the volume ($\delta\mathcal{Q}^\sharp$), and the effect of the temperature distribution at the domain's boundaries ($\delta\mathcal{Q}$).

Equation (4.64) is analogous to that governing the mechanics of an elastic system with viscous dissipation and negligible inertia force. The main difference with respect to the classical principle is the definition of the thermal potential and the definition of the displacement field that represents energy generation. This latter point will be explained thoroughly later on.

Displacement field for energy generation/absorption

As discussed before, the heat generation in the volume is considered in the classical principle by means of the fictitious $\mathbf{H}^*$ displacement field of (4.36), while in the neat variational principle, it is described through the field $\mathbf{H}^\sharp$, (4.51). It is easy to verify that

$$\mathbf{H}^* = -\mathbf{H}^\sharp\,. \tag{4.67}$$

Recall that, in the Biot's principle, energy conservation (4.38) and Fourier's law (4.39) are respectively expressed as

$$c\,[\theta - \theta_0] = -\nabla\cdot\mathbf{H}^+\,, \quad \lambda\nabla\theta + \dot{\mathbf{H}}^+ + \dot{\mathbf{H}}^* = 0\,, \tag{4.68}$$

while in the neat variational principle they are given by (4.52) and (4.47), respectively, i.e.,

$$c\,[\theta - \theta_0] = -\nabla\cdot\left[\mathbf{H} + \mathbf{H}^\sharp\right]\,, \quad \lambda\nabla\theta + \dot{\mathbf{H}} = 0\,. \tag{4.69}$$

By comparing these expressions, it is evident that $\mathbf{H}^+ = \mathbf{H} + \mathbf{H}^\sharp$, and $\mathbf{H}^+ + \mathbf{H}^* = \mathbf{H}$. Furthermore, by comparing the two variational principles (4.40) and (4.53), it is evident that they coincide when $\mathbf{H}^* = \mathbf{H}^\sharp = 0$, so that $\mathbf{H}^+ = \mathbf{H}$. Anyway, the definition of heat generation in the neat principle preserves the physical meaning of the heat displacement field.

The "Neat" variational principle in Biot's notation

The neat variational principle can be expressed in the classical Biot's notation by multiplying the energy conservation equation (4.38) by the variation $\nabla\cdot\delta\mathbf{H}^+$ giving

$$\int_\Omega [\theta - \theta_0]\,\nabla\cdot\delta\mathbf{H}^+\,dV + \int_\Omega \frac{1}{c}\,\nabla\cdot\mathbf{H}^+\nabla\cdot\delta\mathbf{H}\,dV = 0\,. \tag{4.70}$$

Considering the weak form of the Fourier's equation (4.39), and integrating by parts, the variational principle can be stated as

$$\begin{aligned}\int_\Omega \frac{1}{c}\ \nabla\cdot\mathbf{H}^+\ \nabla\cdot\delta\mathbf{H}^+\ dV + \int_\Omega \frac{1}{\lambda}\dot{\mathbf{H}}^+\cdot\ \delta\mathbf{H}^+\ dV = \\ -\int_{\partial\Omega}\theta\delta\mathbf{H}\cdot\mathbf{n}\ ds + \int_\Omega \theta_0(\mathbf{x})\nabla\cdot\delta\mathbf{H}\ dV - \int_\Omega \frac{1}{\lambda}\dot{\mathbf{H}}^*\cdot\ \delta\mathbf{H}^+\ dV\,. \end{aligned} \tag{4.71}$$

Hence, the neat variational principle is not *complementary* to the classical one, but it may be considered *dual*, because the roles of the governing equations is reversed. Roughly speaking, in the neat principle energy conservation (4.52) is the "Euler-Lagrange equation", while Fourier's law (4.39) is the "constraint", while the viceversa holds for the Biot's principle.

4.3.4 A Mechanical Analogy for the One-Dimensional Case

Considering the neat variational principle in the simple 1-D case suggests an interesting mechanical analogy that also serves as an illustration in the mechanical language. Considering, as a reference configuration, the 1-D domain Ω of length s, defined by $z \in [0, s]$. The heat flux $\dot{H}(z,t)$ and the temperature field $\theta(z,t)$ are related by the 1-D Fourier equation

$$\lambda\ \theta' + \dot{H} = 0\,, \tag{4.72}$$

where ($'$) denotes the derivative with respect to z. The energy conservation equation in 1-D becomes

$$-[H' + H^{\sharp\prime}] = c[\theta - \theta_0]\,. \tag{4.73}$$

Following the same procedure for deriving the neat principle explained in section 4.3.1 one gets

$$\begin{aligned}\int_0^s \frac{1}{c}\ H'\delta H'\ dz + \int_0^s \frac{1}{\lambda}\ \dot{H}\delta H\ dz = \\ -\ [\theta\delta H]_0^s + \int_0^s \theta_0\delta H'\ dz - \int_0^s \frac{1}{c}\ H^{\sharp\prime}\delta H'\ dz\,.\end{aligned} \tag{4.74}$$

Consider now a linear elastic bar $z \in [0, s]$, with Young's modulus E and cross sectional area A. Figure 4.1 shows that each infinitesimal section between z and $z + dz$, is grounded by a dashpot with viscous constant ηdz. Suppose that each point z where the dashpot is anchored undergoes the displacement $u^\sharp(z,t)$, positive if in the direction of positive z, and let $u(z,t)$ denote the elongation of the end points

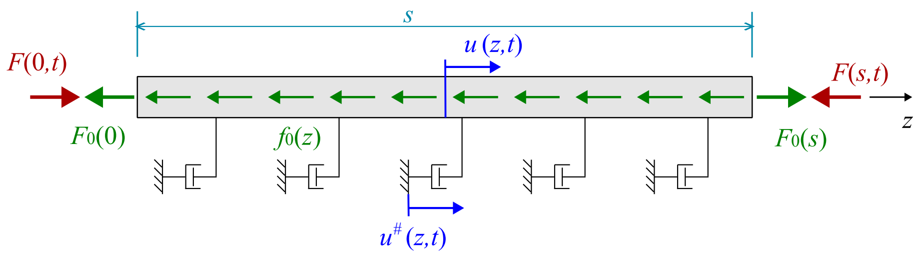

Figure 4.1: Mechanical analogy for the one dimensional thermal problem: linear elastic bar connected to the ground by an array of dashpots.

of the dashpot, so that $u^\sharp(z,t) + u(z,t)$ is the total displacement of the point z of the bar.

In the initial reference configuration, at $t = 0$, the bar is subjected to distributed forces per unit length $f_0(z)$. Define

$$F_0(z) := \int_0^z f_0(\zeta)\, d\zeta + N_0\,, \tag{4.75}$$

such that $F_0(0) = N_0$ and $F_0(s) = \int_0^s f_0(\zeta)\, d\zeta + F_0(0)$ are the normal forces acting at the bar ends at $t = 0$. Furthermore, as shown in Figure 4.1, time-dependent *compression* forces $F(0,t)$ and $F(s,t)$ are applied at the bar ends.

The equilibrium equation for an infinitesimal segment comprised between the generic section z and $z + dz$ reads

$$EA\left[u''(z,t) + u^{\sharp\,\prime\prime}(z,t)\right] - \eta\dot{u}(z,t) - F_0'(z) = 0\,, \tag{4.76}$$

with boundary conditions

$$\begin{aligned} EA\left[u'(0,t) + u^{\sharp\,\prime}(0,t)\right] &= -F(0,t) + F_0(0)\,,\\ EA\left[u'(s,t) + u^{\sharp\,\prime}(s,t)\right] &= -F(s,t) + F_0(s)\,. \end{aligned} \tag{4.77}$$

To state the equivalence with the thermal problem, in which the temperature is prescribed at the boundary $z = 0$ and $z = s$, it is sufficient to set

$$EA = \frac{1}{c}\,, \quad \eta = \frac{1}{\lambda}\,. \tag{4.78}$$

From the analogy, it is evident that the displacement fields $u(z,t)$ and $u^\sharp(z,t)$ correspond to $H(z,t)$ and $H^\sharp(z,t)$, respectively, while $F_0(z)$ is the counterpart of the initial temperature $\theta_0(z)$.

More in particular, denoting with $N(z,t) = F(z,t) - F_0(z)$ the axial force in the bar, assumed positive if compressive, the constitutive law is in the form

$$N(z,t) = F(z,t) - F_0(z) = -EA\left[u'(z,t) + u^{\sharp\prime}(z,t)\right] , \tag{4.79}$$

corresponding to the energy conservation law (4.73), while the axial equilibrium equation is

$$\eta\dot{u}(z,t) = -F'(z,t) , \tag{4.80}$$

which is the counterpart of the Fourier's equation (4.72). Clearly, $F(z,t)$ corresponds to the temperature field $\theta(z,t)$. Hence, the compression forces $F(0,t)$ and $F(s,t)$ applied at the bar ends play the role of the boundary temperatures.

The condition (4.80) implies that any solution for which $\dot{u}(z,t) = 0$, such that $u(z,t) = u(z)$, shall be characterized by $F'(z,t) = 0$. This means that the heat flux is null: when the steady state condition is reached the temperature field is uniform. More generally, the analogy between the equations for the elastic and the thermal cases suggests that, in a finite element implementation of the thermoelastic problem, the same shape functions can be considered to approximate both the elastic and the heat displacements.

4.3.5 Numerical Implementation

The one-dimensional classical form of the variational principle was recently implemented by Galuppi *et al.* [81]. Due to the presence of the temperature field in the classical principle (4.40), the Finite Element (FE) implementation required C^1 continuous shape functions. This FE solution was applied to multilayered plates, consisting of an arbitrary number of plies having different physical and thermal properties. The method was later extended to the three-dimensional case of a homogeneous plate subjected to time-dependent, non-uniform thermal loads [82], [83].

However, this implementation faced significant challenges, primarily due to the need to approximate both the temperature field and the heat displacement field. In contrast, in the "neat" variational principle, only the heat displacement field requires approximation, leading to a simpler and more efficient FE implementation. Furthermore, the variational principle (4.53) involves only first-order differentiation of the heat displacement field $\mathbf{H}$, meaning that it needs to be only C^0 continuous. As a result, the degrees of freedom are simply the time-dependent values of the heat displacement field components at the nodes.

The finite element used here is the standard 8-node, 24-degree-of-freedom hexahedral linear element. Denoting by $\tilde{\mathbf{H}}_e(t)$ the (24×1) vector containing the element's degrees of freedom, and by $\phi(\mathbf{x})$ the (3×24) matrix collecting the tri-linear

Lagrangian shape functions, the heat displacement field and its time derivative can be expressed as

$$\mathbf{H}_e(\mathbf{x},t) = \boldsymbol{\phi}(\mathbf{x})\,\tilde{\mathbf{H}}_e(t)\ ,\ \dot{\mathbf{H}}_e(\mathbf{x},t) = \boldsymbol{\phi}(\mathbf{x})\,\dot{\tilde{\mathbf{H}}}_e(t)\,. \tag{4.81}$$

This approximation is also valid for describing the variation of the displacement field, in the form

$$\delta\mathbf{H}_e(\mathbf{x},t) = \boldsymbol{\phi}(\mathbf{x})\,\delta\tilde{\mathbf{H}}_e(t)\,. \tag{4.82}$$

By substituting (4.81) and (4.82) in (4.54), the variational principle in the finite element may be written as

$$\mathbf{K}_e\,\tilde{\mathbf{H}}_e(t) + \mathbf{C}_e\,\dot{\tilde{\mathbf{H}}}_e(t) = \mathbf{q}_e(t) + \mathbf{q}_{0,e} + \mathbf{q}_e^\sharp(t)\,, \tag{4.83}$$

where, by denoting by c_e and λ_e the heat capacity and the thermal conductivity of the element, $\mathbf{K}_e$ and $\mathbf{C}_e$ are the stiffness and damping matrices at the element level, i.e.

$$\mathbf{K}_e = \frac{1}{c_e}\int_{\Omega_e}\left[\nabla^T\boldsymbol{\phi}(\mathbf{x})\right]^T\ \nabla^T\boldsymbol{\phi}(\mathbf{x})\ dV\,,\quad \mathbf{C}_e = \frac{1}{\lambda_e}\int_{\Omega_e}\boldsymbol{\phi}^T(\mathbf{x})\ \boldsymbol{\phi}(\mathbf{x})\ dV\,. \tag{4.84}$$

Furthermore, $\mathbf{q}_e(t)$, $\mathbf{q}_{0,e}(t)$ and $\mathbf{q}_e^\sharp(t)$ are the counterpart of the thermal driving forces defined by (4.66), i.e.

$$\begin{aligned}
\mathbf{q}_e(t) &= -\int_{\partial\Omega_e}\theta(\mathbf{x},t)\ \boldsymbol{\phi}(\mathbf{x})\cdot\mathbf{n}\ ds\,,\quad \mathbf{q}_{0,e}(t) = \int_{\Omega_e}\theta_0(\mathbf{x})\nabla^T\boldsymbol{\phi}(\mathbf{x})\ dV\,,\\
\mathbf{q}_e^\sharp(t) &= -\frac{1}{c_e}\int_{\Omega_e}\nabla\cdot\mathbf{H}^\sharp(\mathbf{x},t)\ \nabla^T\boldsymbol{\phi}(\mathbf{x})\ dV\,,
\end{aligned} \tag{4.85}$$

Notice that the term $\mathbf{q}_e(t)$ in (4.85) accounts for the temperatures at the element boundaries.

Unless a matching condition of type E or type F (see Sect. 4.1.1) is present, the matching conditions of the variational principle, derived from the continuity of the heat displacement and its variation, imply that the temperature field is continuous. Thanks to this, all the terms cancel out after assembling the $\mathbf{q}_e(t)$ vectors, except on the external domain boundary $\partial\Omega$.

By following the standard procedure in finite element analysis [84], the element matrices and load vectors are assembled to arrive at the equations of the entire body

$$\mathbf{K}\,\tilde{\mathbf{H}}(t) + \mathbf{C}\,\dot{\tilde{\mathbf{H}}}(t) = \mathbf{q}(t) + \mathbf{q}_0 + \mathbf{q}^\sharp(t)\,, \tag{4.86}$$

where $\tilde{\mathbf{H}}(t)$ is the vector collecting all the nodal degrees of freedom, while $\mathbf{K}$, and $\mathbf{C}$ are the global stiffness and damping square matrices, respectively, while $\mathbf{q}(t)$, $\mathbf{q}_0$ and $\mathbf{q}^\sharp(t)$ are the global vectors containing the thermal driving forces. Once $\tilde{\mathbf{H}}(t)$ is found by solving (4.86) with proper boundary conditions, the temperature field can be evaluated by integrating Fourier's equation (4.47). The integration constants in space can be found from the boundary conditions, while the time integration constant comes from the initial conditions on the temperature field.

Regarding the matching conditions of types E and F, explained in Sect. 4.3.2, the interface condition resulting in a discontinuous temperature field is considered, in the numerical implementation, by placing nodes in correspondence of the interface, so to represent the interface and its properties. In this case, the matrix form (4.86) of the variational principle becomes

$$\mathbf{K}\,\tilde{\mathbf{H}}(t) + [\mathbf{C} + \mathbf{C}_s]\;\dot{\tilde{\mathbf{H}}}(t) = \mathbf{q}(t) + \mathbf{q}_0 + \mathbf{q}^\sharp(t)\,, \tag{4.87}$$

where $\mathbf{C}_s$ is a square matrix, where the only non-zero terms are those corresponding to the degrees of freedom associated with $\dot{H}_\zeta(\xi, \eta, 0, t)$ of the interfacial nodes (see eq. (4.62)), in the direction normal to the interface, which are set equal to $1/\Gamma$.

When boundary temperatures are given functions of the environmental temperatures and of the heat flux (boundary conditions of type C, see Sect. 4.3.2), one can substitute the value of the temperature as a function of $\dot{H}_n$ and the external temperature in the boundary term of (4.55). To make the calculation explicit, consider the boundary conditions in the form (4.15). Solving for $\theta(\mathbf{x}, t)$ and substituting in the boundary term of (4.55), using the discretization (4.81), one finds that (4.86) becomes

$$\mathbf{K}\,\tilde{\mathbf{H}}(t) + [\mathbf{C} + \mathbf{C}_b]\;\dot{\tilde{\mathbf{H}}}(t) = \mathbf{q}_b(t) + \mathbf{q}_0 + \mathbf{q}^\sharp(t)\,, \tag{4.88}$$

where

$$\mathbf{C}_b := \frac{1}{h}\int_{\partial\Omega} \boldsymbol{\phi}^T(\mathbf{x})\;\boldsymbol{\phi}(\mathbf{x})\cdot\mathbf{n}\;ds\,, \tag{4.89a}$$

$$\mathbf{q}_b(t) = -\int_{\partial\Omega} \theta_e(\mathbf{x}, t)\;\boldsymbol{\phi}(\mathbf{x})\cdot\mathbf{n}\;ds\,. \tag{4.89b}$$

Observe that the term associated with $\mathbf{C}_b$ accounts for *boundary dissipation* [79].

The proposed FE approach can be particularized to two- and one-dimensional problems by reducing the number of degrees of freedom associated to each node. In the simplest one-dimensional case, the finite element is a 1-D bar, with two nodes and two degrees of freedom. After solving the problem, one obtains the time history of the heat displacement field in the body. To compute the temperature field, the 1-D version of the Fourier's law (4.8) must be integrated, with the constant of integration determined from the boundary conditions. Alternatively, the temperature at the nodes can be calculated using the element equations, as the temperature in this case is analogous to the internal force in a similar mechanical problem.

A group of examples is presented in the next Chapter 5, to serve as validation for an in-house made FE code, implementing the neat variational principle.

Chapter 5

Validation and Numerical Examples

Here, four different examples and case studies are solved by means of an in-house-made code implementing the neat variational principle of Sect. 4.3, through the procedure detailed in Sect. 4.3.5. First, two simple one-dimensional examples, previously solved in the literature using other methods, are presented with the aim of validating the neat variational principle. Then, a few more examples are considered to demonstrate the application of the neat variational principle to laminated glass [78], [85], with particular reference to uneven heating conditions. The main assumptions of the model include the isotropy of the thermal properties within each material and their independence from temperature variations.

5.1 Example 1: *Plate with Prescribed Temperature at One Face, Insulated at the Other*

Consider a homogeneous pane of thickness $s = 50\,\mathrm{mm}$, initially at the uniform temperature $\theta_0(z) = 0\,°\mathrm{C}$. No heat sources are present. At $t = 0$, the face $z = 0$ is suddenly brought to the temperature $80\,°\mathrm{C}$, while the face $z = s$ is thermally insulated. These correspond to boundary conditions of types A and B, respectively, as explained in Sect. 4.1.1.

$$\theta(0,t) = \overline{\theta} = 80\ °\mathrm{C}\,, \qquad \dot{H}(s,t) = 0\,, \quad \forall t\,. \tag{5.1}$$

Biot solved the problem [79] by approximating the temperature field with a parabolic function, and by dividing the heating process into two phases. First, heat penetrates up to a depth $z = \bar{s}$, called the *penetration depth*. This phase ends at $t = \bar{t}$, when the penetration depth equals the plate thickness ($\bar{s} = s$). In the second phase, for $t > \bar{t}$, the temperature rises at the insulated boundary.

In our numerical solution, the mesh is refined in the neighborhood of $z = 0$ since the temperature presents a discontinuity here at $t = 0$: 20 elements, 0.5 mm thick, are used for $0 < z < 10$ mm, while 8 elements, 5 mm thick, compose the remaining part. The obtained results in terms of the temperature profile $\theta(z, t)$ at different t, evaluated by setting $\lambda = 200$ W/(m K) and $c = 2.7 \cdot 10^6$ J/(m^3 K), are plotted in Figure 5.1. For the sake of comparison, the same figure shows Biot's solution [79] and the results obtained by solving the differential form of the heat conduction equations via Fourier series expansion (first 30 terms of the series), as in [57]. The results show excellent agreement.

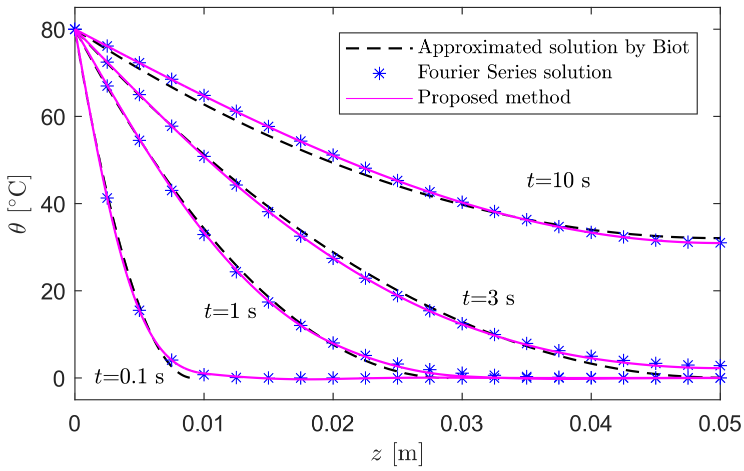

Figure 5.1: Example 1. Temperature profile at different times evaluated with the proposed approach, compared with Biot's solutions [79], and with the solution of the differential form of the thermal problem obtained in Fourier series expansion [57].

5.2 Example 2: *Element with Interfacial Thermal Resistance*

This example considers the matching condition of type F, where the temperature profile is discontinuous at the interface between two different materials due to the effect of an ITR. Here, the results obtained through the proposed method are compared with a solution proposed by Yuan *et al.* in [80].

The considered example is a composite plate made of two layers of thickness $s_1 = s_2 = 0.5$ m, with $\lambda_1 = 200$ W/(m K), $\lambda_2 = 100$ W/(m K), and $c_1 = c_2 = 2.7 \cdot 10^6$ J/(m^3 K), with an Interfacial Thermal Resistance $R = 1/500$ m^2 K/W. The initial temperature is assumed uniform and equal to 20 °C. At $t = 0$, the temperature is suddenly raised to 480 °C on the side $z = 0$, whereas it is kept fixed at 20 °C at $z = s_1 + s_2 = s$.

In [80], different 1D modeling strategies, solved with finite differences, were developed to account for the ITR: *i)* numerically implementing the ITR relation (4.62) in terms of the temperature derivative; *ii)* creating a "virtual layer" with a very small thermal conductivity λ_ζ (compare eq. (4.63)) at the interface to represent the ITR; *iii)* using a local "artificial layer" surrounding the interface with modified thermal properties to reflect the influence of the ITR on the heat transfer through the interface. These approaches are reliable but require a very fine mesh: by changing the mesh size, the temperature profile does change. Convergence is reached using 500 elements, 2 mm thick, with a time step of 0.001 h.

In the proposed variational approach, it may be verified that convergence is reached with only 20 elements, 50 mm thick, with a time step of 0.01 h. Accurate results may also be obtained with only four elements, but this mesh is not accurate for the evaluation of the interfacial temperatures in the first minutes of the "loading" history, when the temperature profile presents a high slope in proximity to the surface $z = 0$, where the temperature jump is instantaneous. Therefore, at the beginning of the transient state, a finer mesh is required to correctly reproduce the temperature profile. When the temperature profile smooths out as a consequence of heat conduction, a coarse mesh is sufficient for good accuracy.

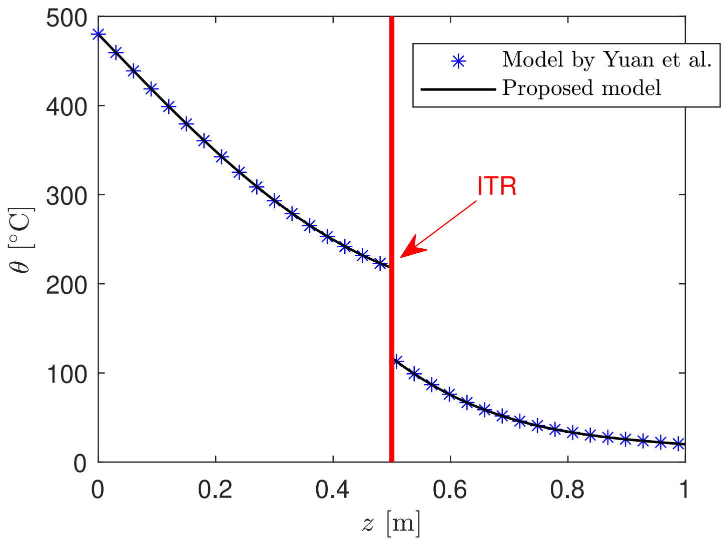

Figure 5.2: Example 2. Comparison between the solution obtained with the proposed approach and that proposed by Yuan et al [80]. Temperature profile at $t = 1500\,\mathrm{s}$

Figure 5.2 shows a comparison of the temperature profiles at $t = 1500$ s, also recorded in [80], with evidence of the temperature jump at the ITR surface. Figure 5.3 shows the time evolution of the temperatures on the two faces of the ITR, i.e., $\theta_{ITR,l}(t) = \theta(s_1^-, t)$ and $\theta_{ITR,r}(t) = \theta(s_1^+, t)$. The difference with the solution proposed in [80] is of the order of 0.5 °C.

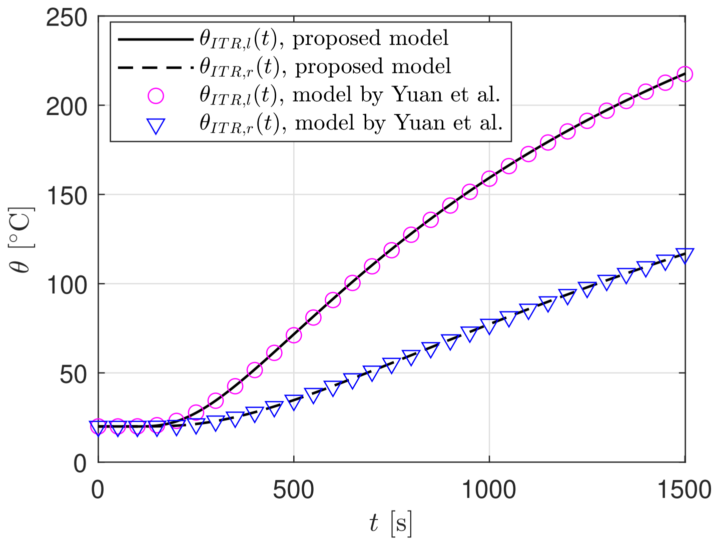

Figure 5.3: Example 2. Comparison between the solution obtained with the proposed approach and that proposed by Yuan et al [80]. time evolution of the temperatures on the two faces of the ITR.

5.3 Example 3: *Partially Shaded Laminated Glass Pane*

The third, 3-D example is representative of a window glass pane, unevenly irradiated by the sun due to cast shadows on its surface, which separates environments at different temperatures. At $t = 0$, the temperature of the pane is assumed to be uniform; at $t = 0^+$, the body is put in contact with the environments and is (unevenly) irradiated by the sun. The solution provides the transient thermal state until the steady-state condition is reached. The model could also account for seasonal or daily varying boundary conditions, but this analysis is not conducted here.

Consider the $1\,\mathrm{m} \times 1.5\,\mathrm{m}$ rectangular laminated glass pane represented in Figure 5.4, composed of alternating glass plies with a PVB polymeric interlayer, with very different physical and thermal properties [81], [86], as indicated in Table 5.1. It is assumed that the interfacial thermal resistance at the glass-PVB interface is negligible. This practice is followed in most technical articles, even if the presence of an ITR cannot a priori be ruled out. According to [87], the ITR is low in the case of a "good" mechanical and chemical bonding between constituent phases, as for well-made laminated glass. There are cases, however, in which partial delamination occurs, either because of poor manufacturing or exposure to an aggressive environment. In such cases, the ITR comes into play.

A reference system is introduced, such that x, y are the in-plane directions and z is along the thickness. The panel is defined by $0 \leq x \leq 1.0\,\mathrm{m}$, $0 \leq y \leq 1.5\,\mathrm{m}$. The laminate is made of one glass ply ($0 < z < s_1$) of thickness $s_1 = 12\,\mathrm{mm}$, the PVB interlayer ($s_1 < z < s_1 + s_2$) of thickness $s_2 = 1.5\,\mathrm{mm}$, and the third glass ply ($s_1 + s_2 < z < s_1 + s_2 + s_3 = s$) of thickness $s_3 = 6\,\mathrm{mm}$. The shaded region is rectangular and identified by the domain $0 < x < 0.5\,\mathrm{m}$ and $0 < y < 0.5\,\mathrm{m}$.

Table 5.1: Values of physical and thermal properties for the materials considered in Example 3.

Material	Reference	c [J/(m^3 K)]	λ [W/(m K)]	α [−]	τ [−]
glass	[88], [89]	$1800\ \ 10^3$	1	0.23	0.67
PVB	[86], [90]	$1478.3\ \ 10^3$	0.236	0.01	0.99

As shown in Figure 5.4, the panel is discretized by using one element in the thickness for each layer (three elements in total) and by dividing the surface into 30 and 50 elements, respectively, in the x and y directions (resulting in 4500 elements and 6324 nodes). The mesh is refined in the neighborhood of the interface between shaded and unshaded regions, where conduction heat exchange occurs. Tri-linear shape functions have been used.

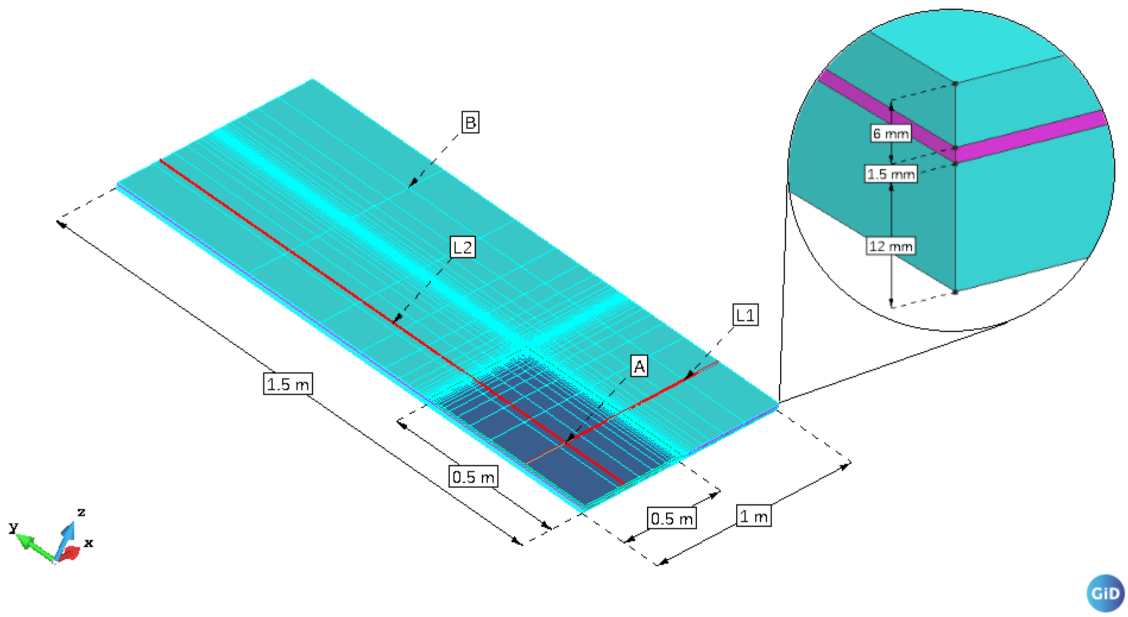

Figure 5.4: Example 3. Laminated glass pane with unshaded and shaded portions: geometry and mesh used in the FEM implementation, plotted with the GiD pre-processor.

The panel exchanges heat via convection (with the external and internal air) and radiation (with the sky vault and external surfaces [91], and with other internal surfaces [92] assumed to be at the same temperature $\theta_i(t)$ of the internal air [93]), possibly time-dependent. Although the radiant energy exchange is proportional to the fourth power of the absolute temperatures [60], since the temperature difference between the panel and the environment is small, the expressions can be linearized [59]. The conclusion is that all the heat-exchange contributions at the panel surfaces provide boundary conditions of the Robin kind, (4.15). This can be written in the form

$$\dot{H}_z(x,y,0,t) = h_e\left[\theta_e(t) - \theta(x,y,0,t)\right] \ , \quad \dot{H}_z(x,y,s,t) = h_e\left[\theta(x,y,s,t) - \theta_i(t)\right] \ , \quad \forall t \, , \tag{5.2}$$

where h_e and h_i are the *total* heat transfer coefficients on the external and internal surfaces, respectively, simultaneously accounting for both convection and radiation, while θ_e is the "nominal" external temperature, accounting for both convection and radiation, defined to provide formal equivalence according to [81].

The solar radiation, here denoted as $G(t)$, can be modeled as an internal heat source [59], [81], possibly time-dependent. The total density of heat flow rate depends on several factors, such as season, time of day, panel orientation, and inclination [94], [95]. A commonly used approach [96] consists of assuming that the heat flux varies linearly in the thickness of each layer [82]. In our notation, this represents a heat source $q^\sharp(z,t)$ of uniform magnitude in each layer, independent of x, y. This also justifies the use of linear shape functions for approximating $H^\sharp_z(\mathbf{x},t)$, while setting $H^\sharp_x(\mathbf{x},t) = H^\sharp_y(\mathbf{x},t) = 0$. The assumption here, following [81], is that part of the energy hitting the external ply at $z = 0$ is absorbed, another part is reflected, and the remaining part is transmitted to the second layer. Similarly, the energy hitting layer 2 splits into an absorbed part, a reflected part, and a part transmitted to layer 3. Denoting with α_i and τ_i the absorptivity and transmissivity with respect to the solar radiation of the ith ply, the heat it absorbs is

$$q^\sharp_i(\mathbf{x},t) = \dot{H}^{\sharp\,\prime}_{z;i}(\mathbf{x},t) = \frac{\alpha_i \ \gamma_i}{s_i}\phi_i(t)\ G(t) \, , \qquad \text{where } \gamma_i := \begin{cases} 1 \ \text{ for } i = 1 \, , \\ \prod_{k=1}^{i-1} \tau_k \ \text{ for } i = 2, 3 \, . \end{cases} \tag{5.3}$$

where $\phi_i(t)$ is a coefficient accounting for the possible presence of shadows. Indeed, the presence of shadows is considered by assigning to elements belonging to different-in-type regions (fully irradiated, shaded, regions shielded by the frame) different values for $\phi_i(t)$. The flux-based FEM can readily consider the mobility of the shadows, simply by imposing a time-varying coefficient $\phi_i(t)$.

However, due to thermal inertia, mobile shadows are considered less critical than static shadows [97], [98], which can generate a cooler area in the glass and, consequently, higher thermal stresses. Here, static shadows are considered and, according to the French standard NF DTU 39 P3 2006 [99], ϕ_i has been set equal to 0.1 for the regions where there are projected shadows.

Equation (5.3) allows to define the heat displacement field $\dot{H}^\sharp_z(\mathbf{x})$ through its nodal values. Here, it has been set to be zero at the external surface $z = 0$, while $\tilde{H}^\sharp_z(x,y,s_1) = \alpha_1\gamma_1 \int_0^t G(t)dt$, $\tilde{H}^\sharp_z(x,y,s_1+s_2) = (\alpha_1\gamma_1 + \alpha_2\gamma_2)\int_0^t G(t)dt$, $\tilde{H}^\sharp_z(x,y,s) = (\alpha_1\gamma_1 + \alpha_2\gamma_2 + \alpha_3\gamma_3)\int_0^t G(t)dt$. An arbitrary additive constant could be added to this field (for example, so to have $\tilde{H}^\sharp_z(z,t) = 0$ at the internal surface $z = s$), without affecting the final results.

First, the case of constant environmental parameters is considered, i.e., $\theta_i(t) = \theta_i$,

$\theta_e(t) = \theta_e$, $G(t) = G$, for which realistic values for a winter scenario have been considered: $G = 800$ W/m^2, $\theta_e =$ -12 °C and $\theta_i =$25°C. The total external and internal heat transfer coefficients, respectively $h_e = 11.926$ W/(m^{2}K) and $h_i = 8.375$ W/(m^{2}K), have been calculated following [81]. The initial temperature is assumed to be $\theta_0 = 0$ °C.

The heat displacement field has been evaluated by solving the matrix problem (4.88), accounting for the Robin boundary conditions at the two panel surfaces. The panel edges have been assumed to be perfectly insulated, i.e., the normal heat flux is zero on the panel borders. Once the heat displacement field is known, the temperature distribution has been recovered by integrating the internal constrain (4.47) (Fourier's law), calculating the integration constants from the boundary conditions.

Figure 5.5 shows the qualitative temperature distribution at the steady state, at the external ($z = s$) and internal ($z = 0$) surfaces. It is evident that they are both approximately uniform in the shaded and not-shaded regions, left aside a thin strip in correspondence of the interface. A similar example with a partially shaded rectangular portion, but in which the pane is monolithic, was considered in [83], by considering the classical version of Biot's variational principle and a different FEM implementation. In that simulation, the temperature field presented singularities at the corner, which were attributed to the irregularity (sharp angle) of the interface boundary [100], [101]. Now, it has been verified that the solution presents a very slight peak in the temperature field at the corner of the shaded region, but apparently does not grow unboundedly. Remarkably, the temperature peak disappears if the angle formed by the interface lines at the corners is just slightly different from 90°: the plots in Figure 5.5 have been obtained for an 89.5° angle. However, the discussion about the potential concentration of temperatures in areas of high curvature is beyond the scope of this thesis.

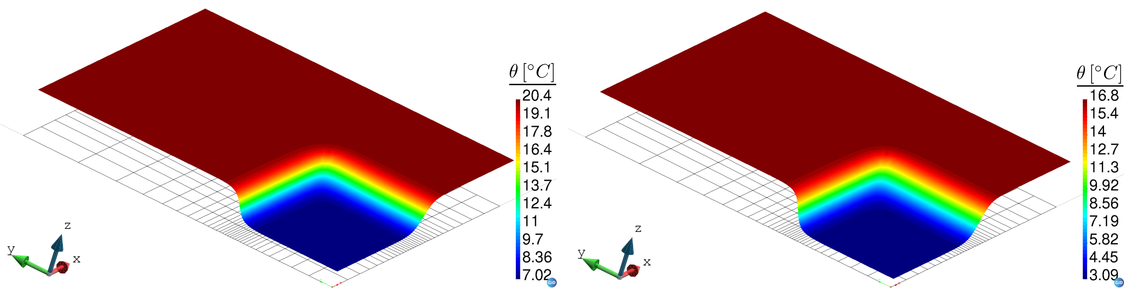

(a) (b)

Figure 5.5: Example 3. Temperature distribution at the steady state, at (a) the internal $z = 0$ and (b) the external $z = s$ surfaces, plotted with the GiD post-processor.

The obtained results are compared with a direct numerical solution of the differential form of the heat-conduction equations, under the aforementioned boundary and initial conditions. This is done with the "pdepe" Matlab tool [102], based on a finite difference approach in both space and time. In this case, the plate has been discretized by using tetrahedral elements, with max size of 15 mm and minimum size of 1 mm, for a total of 129328 elements and 219004 nodes.

Figure 5.6 shows the time variation of the temperatures at the internal ($z = 0$)

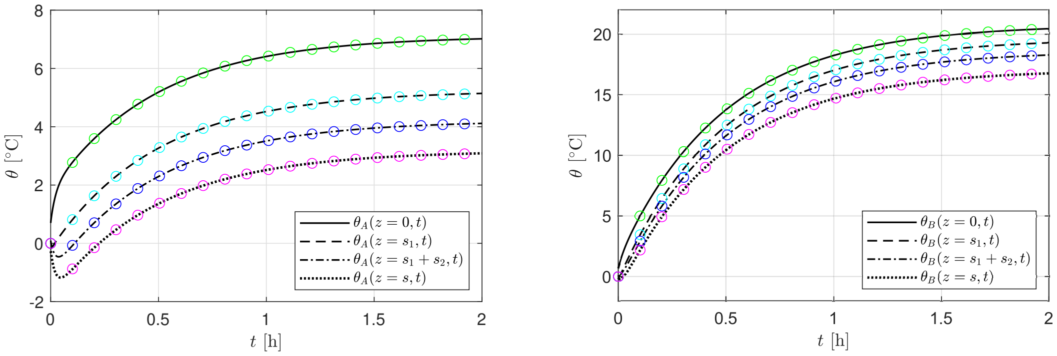

(a) (b)

Figure 5.6: Example 3. Temperature as a function of time t on the external ($z = s$) and internal ($z = 0$) surfaces and at the interfaces ($z = s_1$ and $z = s_2$), in the a) irradiated and b) shaded regions. Comparisons between the proposed approach (lines) and the numerical solution of the differential form of the heat-conduction equations (markers).

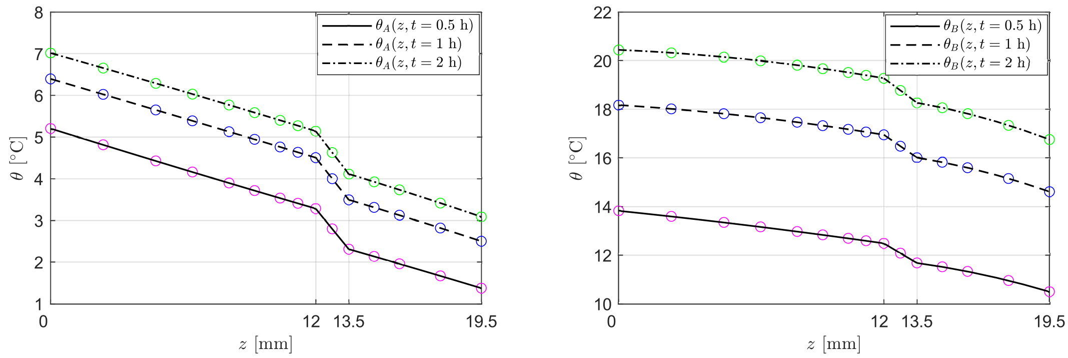

(a) (b)

Figure 5.7: Example 3. Through-the-thickness temperature profile at different times at the same points considered in Figure 5.6. Comparisons between the proposed solutions (lines) and the numerical solution of the differential form of the heat-conduction equations (markers).

and external ($z = s$) surfaces, as well as of the interface temperatures at $z = s_1$ and $z = s_2$, at two different (x, y) coordinates of the laminated panel. Figure 5.6(a) considers a point A of the shaded region far from the interface (where the temperature is constant in practice at the steady state), whereas Figure 5.6(b) refers to a point B of the fully irradiated region, again far from the interface, both indicated in Figure 5.4. The graphs also show the comparison with the direct numerical solution, plotted with markers. The steady state condition is achieved in about two hours.

For the same points A and B, Figure 5.7 records the temperature profile across the thickness of the laminated glass element, for different time instants.

To analyze the in-plane temperature distribution, Figure 5.8 shows the surface and interface temperatures, at the steady state (t =2 h), on the lines L_1 and L_2 indicated in Figure 5.4. These graphs emphasize the sigmoidal temperature profile

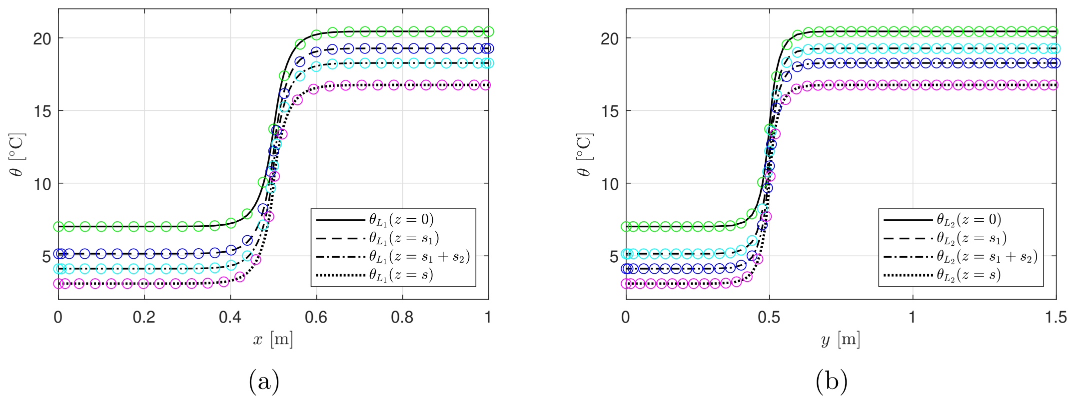

Figure 5.8: Example 3. In-plane temperature distribution at the steady state, on the external and internal surfaces and at the interfaces, calculated on the lines a) L_1 and b) L_2 of Figure 5.4. Comparisons between the proposed approach (lines) and the numerical solution of the differential form of the heat-conduction equations (markers).

in proximity of the interfaces. The transition zone has a width of about ten times the thickness of the whole laminated panel, which confirms the findings of [83].

The comparison with the solution obtained from the differential form of the thermal problem indicates an excellent agreement with our method, being the maximum difference less than 0.2 °C. It has also been verified, in a simpler model problem, that the pde solution requires a much higher number of elements than the proposed approach to obtain comparable results. Since the computational time is comparable for the two methods kept fixed the number of nodes, the novel approach is computationally much more efficient.

5.4 Example 4: *Laminated Glass Panel Under Time Dependent Uneven Heating Conditions*

The developed in-house made code is now used to analyze architectural glazing under varying environmental conditions (temperature and solar radiation), specifically considering the partial shading of the surfaces due by external obstacles (adjacent buildings, trees, sunshades, etc.) and blinds or backups [103]. Indeed, the past experience has evidenced that many failures in building glazing are due to an inhomogeneous temperature distribution in the glass panes consequent to the presence of shadows, which produces the incompatible material straining [104] and, therefore, an eigenstress state that may overcome the glass strength. This represents the root cause of glass failures in architecture [103], [105], [106]. The goal, here, is to investigate how the temperature field is influenced by the amount of shaded area and by its shape.

Reference is made to a rectangular laminated glass element, of size $a = 1$ m $\times$ $b = 1.5$ m, composed of two glass plies of thickness $s_1 = 6$ mm (on the external side) and $s_3 = 12$ mm, bonded by a PVB interlayer of thickness $s_2 = 1.5$ mm, whose cross section is schematically shown in Figure 5.9.

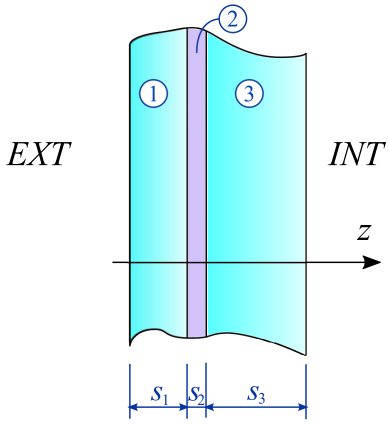

Figure 5.9: Schematics of the cross section of the considered laminated glass element.

Considered values for physical and thermal properties, appearing in the heat conduction equation (4.10), for glass [88], [89] and interlayer [86], [90] are $c_1 = c_3 = 1800\ 10^3$ J/(m^3 K), $c_2 = 1478.3\ 10^3$ J/(m^3 K), $\lambda_1 = \lambda_3 = 1$ W/(m K), $\lambda_2 = 0.236$ W/(m K). The material absorptivity and transmissivity, appearing in (5.3), respectively, are $\alpha_1 = \alpha_3 = 0.23$, $\alpha_2 = 0.01$, $\tau_1 = \tau_3 = 0.67$ and $\tau_2 = 0.99$ [81]. According to French NF DTU 39 P3 2006 [99], it is assumed that only the 10 % of the solar radiation strikes the shaded parts of the panel, $\phi_i(t) = 0.1$ in (5.3) in the shaded regions.

This example certainly represents a very simplified view of a real case. In particular, the presence of a contouring frame, or other types of fixing devices, which certainly contribute to heat transfer, are not considered. Nonetheless, I believe that it is an interesting example for testing the code, because it has been analyzed in other articles with other methods. The results that can be drawn from it are also of a certain practical importance, especially in the characterization of the temperature profile in the transition zone between shaded and irradiated regions.

1. *Influence of the size of the shaded area*

To investigate the influence of the size of the shaded area, the model problem is that of Figure 5.10: the rectangular $a \times b$ laminated glass pane has a shaded portion of width βa, with $a = 1$ m, $b = 1.5$ m , $\beta \in [0, 1]$. Denote with "A" the irradiated region, and with "B" the shaded region.

The solar radiation $G(t)$ and the external temperature $\theta_e(t)$ are made to vary according to daily variations, the same considered in [99]. For a winter scenario, the time dependence of $G(t)$ is approximated [107] with a parabolic law, while $\theta_e(t)$ is assumed sinusoidal in time, as shown in Figure 5.11. The internal and external heat transfer coefficients are $h_i = 8.375$ W/(m^{2}K) and $h_e = 11.926$ W/(m^{2}K), respectively.

In the numerical model, the normal heat displacement is prescribed to be null at

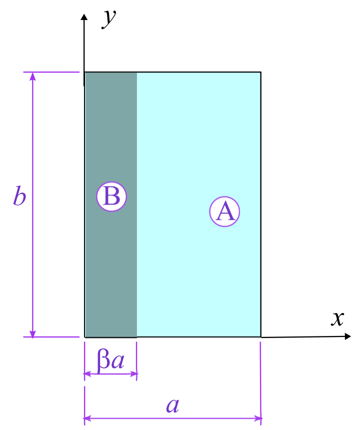

Figure 5.10: Model problem for the evaluation of the effect of shadow size on the temperature distribution of a partially irradiated laminated glass panel.

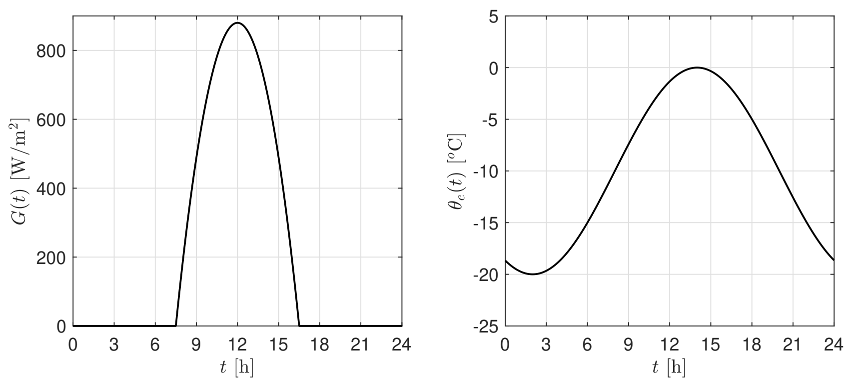

Figure 5.11: Example 4. Daily variation of solar radiation $G(t)$ and external temperature $\theta_e(t)$, for a winter scenario.

the plate edges, while boundary conditions of type C (Robin boundary conditions, (4.15)) are prescribed on the plate surfaces. In the z direction, the plate has been discretized by using one element for each composing layer, while it has been verified that the the convergence is reached[1] by dividing both the shaded and the irradiated region in 10 elements in the x direction. Since, thanks to symmetry, the temperature field is expected to be independent of y, a coarser mesh can be adopted in this direction, and it has been verified that accurate results are obtained with only one element. This results in a total number of only 20 elements.

When half of the pane is shaded ($\beta = 0.5$), Figures 5.12(a) and 5.12(b) show the spatial temperature distribution along x during the light hours (9 A.M., 12 A.M., 3 P.M.), at the external and internal surfaces, respectively. Observe that the temperature is uniform in the two regions, except in a strip across the interface between them. where heat conduction takes place. In this interface region, whose width is of the order of 0.2 m, in agreement with the results of [83], the temperature profile can be well approximated by a sigmoidal curve, whose qualitative shape is the same for the different hours of the day.

[1]Convergence analyses has been performed by increasing the number of elements until the results present an error lower than 0.1 °C with respect to the solution obtained by refining the mesh.

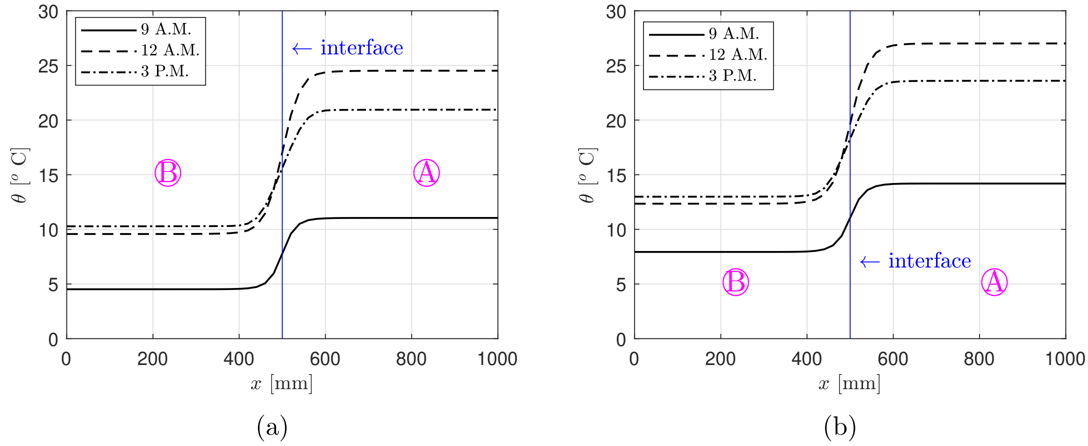

Figure 5.12: Example 4. Spatial temperature distribution, in the x direction, at the a) external and b) internal pane surfaces, at various light hours of the day.

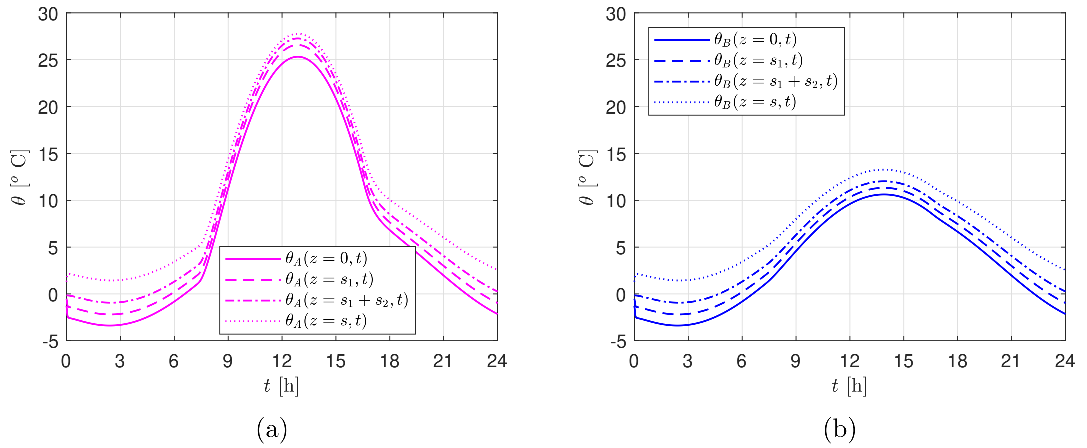

Figure 5.13: Example 4. Time evolution of the temperature on the external, internal and interface surfaces, in the a) irradiated and b) shaded regions.

Figure 5.13 shows the time evolution along a day of the temperature at the external ($z = 0$) and internal ($z = s := s_1 + s_2 + s_3$) panel surfaces, as well as the temperatures at the two glass-polymer interfaces $z = s_1$ and $z = s_1 + s_2$, again for $\beta = 0.5$, evaluated at points of the regions A and B sufficiently far from the interface, where the temperature is substantially uniform. In agreement with [107], the temperature time-evolution is influenced by the parabolic variation of $G(t)$ and the sinusoidal trend of $\theta_e(t)$. In general, the temperature $\theta_A(z,t)$ in the fully irradiated region is more affected by $G(t)$ than by $\theta_e(t)$; the vice-versa for the temperature $\theta_B(z,t)$ in the shaded region, which presents a pseudo-sinusoidal trend.

Figures 5.14(a) and 5.14(b) respectively indicate, as a function of β, the maximum and minimum temperatures recorded along a day at the internal and external surfaces on regions A and B, again evaluated where they are substantially uniform. The size of the shadow is varied from the 10 % to the 90 % of the panel area. Observe that the temperatures are substantially independent of the percentage of shaded area. Furthermore, the minimum temperatures of regions A and B coincide, both on the internal and the external glass surfaces, because these are reached

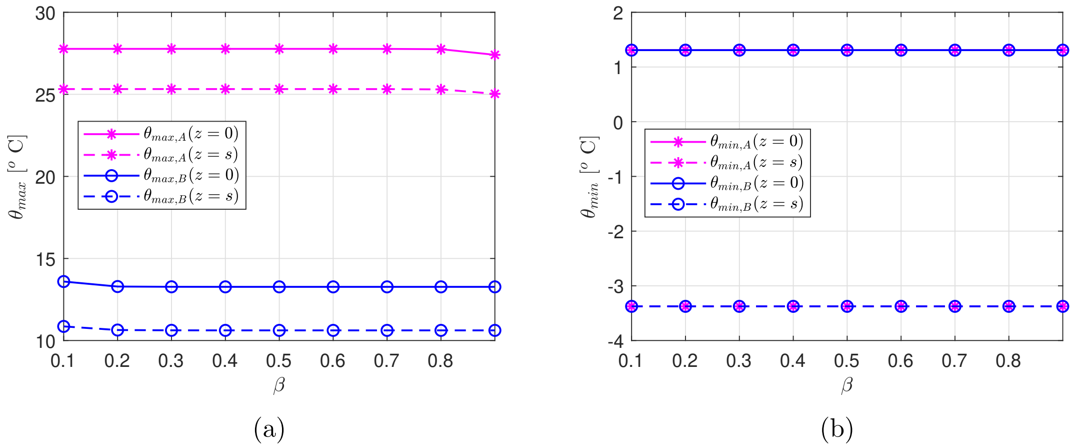

Figure 5.14: Example 4. a) Maximum and b) minimum temperatures in the regions A and B (internal and external surfaces), sufficiently far from the interface, as a function of the amount of shaded area

during the night hours when the solar radiation is nihil.

Figure 5.15 reports the maximum temperature difference $\Delta\theta_{max}$ between the exposed and shaded areas of glass, recorded along the 24 hours, again as a function of the amount of shaded area and evaluated at both the internal and external panel surface. Thermal stress can only be calculated with an elastic analysis taking into account the thermal strain but, kept fixed the geometry, it is certainly related to $\Delta\theta_{max}$ [99], [107]. Observe that $\Delta\theta_{max}$ is only slightly affected by the percentage of shaded area.

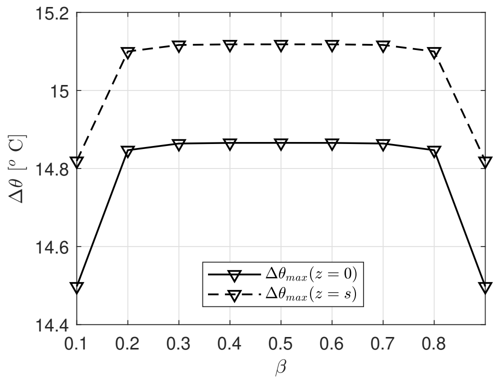

Figure 5.15: Example 4. Maximum temperature difference between regions A and B (internal and external surfaces), as a function of the amount of shaded area

These results would indicate that, in order to evaluate the maximum temperature difference, it is not necessary to consider all possible configurations, since the temperature difference is only mildly affected by the size of the shadow. However, this problem does not consider the effects of heat conduction through contouring frame or fixing device, which can certainly be of importance. Nevertheless, this example was chosen because of its symmetry for code verification: the results obtained with a 3D mesh indeed respect the expected symmetry.

2.*Influence of the shadow shape*

Consider now different shadow shapes, as indicated shown in Figure 5.16. These have been selected from the qualitative classification of dangerousness indicated in [108], where it is stated that the most critical, for the thermal stress, are the "V-shaped" shadows. Similar were studied in [107], but with a simplified engineering model.

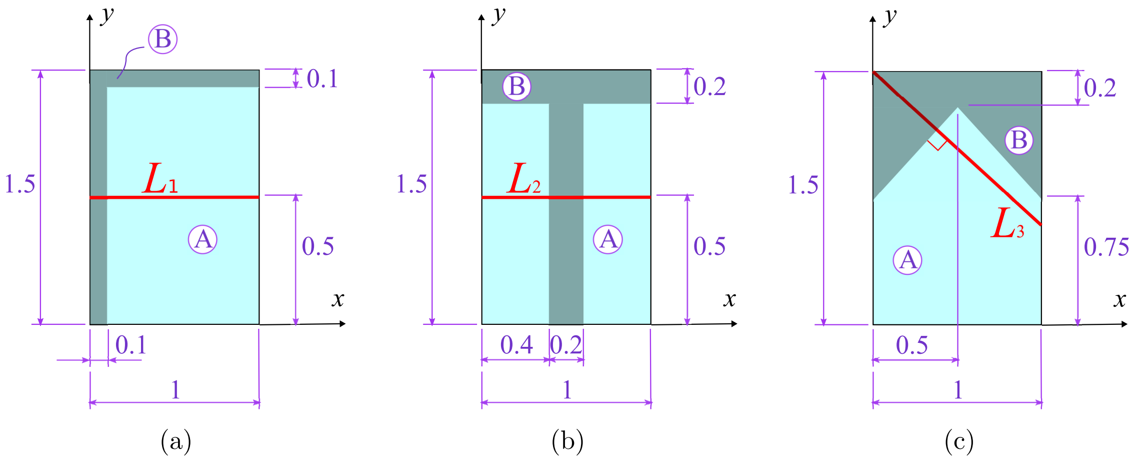

Figure 5.16: Example 4. Different shadow shapes considered in the study: a) L-shaped, b) T-shaped and c) V-shaped.

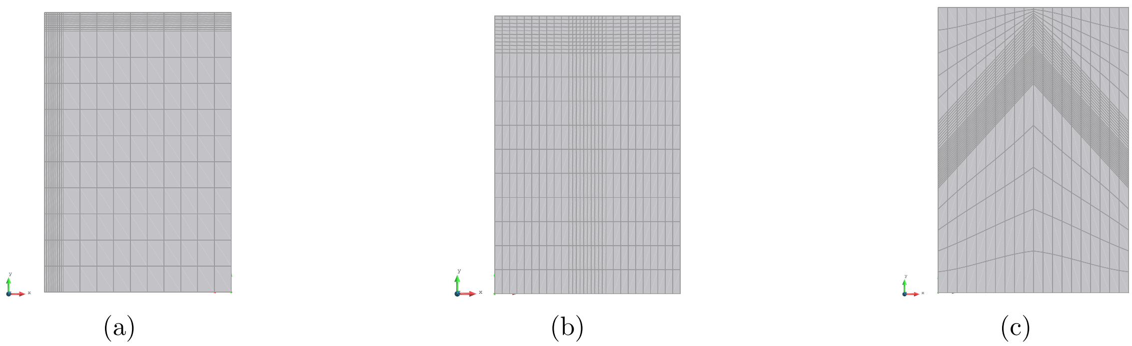

Figure 5.17: Example 4. In-plane mesh considered in the numerical analyses: a) L-shaped, b) T-shaped and c) V-shaped.

The results presented above indicate that, at a distance from the interfaces, the temperatures are homogeneous in both regions A and B, and that their time evolution along the 24 hours is only mildly affected by the shadow size. Therefore, here the shadowed regions have a fixed area. Furthermore, since the width of the strip across the interface where heat conduction occurs is independent of the time-evolution of the temperature, as per Figure 5.12, here only constant environmental conditions are considered. Assumed environmental parameters are G=800 W/m^2, θ_e =-12 °C. For the external and internal heat transfer coefficients, the same values considered before have been used. Figure 5.17 show the adopted in-plane mesh, while, again, in the out-of-plane direction only one element has been used, for each layer. The total number of elements is 1200 for the L-shaped, 1800 for the T-shaped, and 2400 for the V-shaped case. The mesh is refined near the interface between the shaded and unshaded areas, specifically in the direction perpendicular to the interface, where the heat flux variation is the greatest. A uniformly refined mesh yielded similar results but proved to be unnecessarily computationally expensive.

Figures 5.18, 5.19 and 5.20 show the spatial temperature distribution for the three considered shadow shapes after 2 hours, when a steady-state condition has been reached. Plots on the left- and right-hand-side refer to the external and internal panel surfaces, respectively.

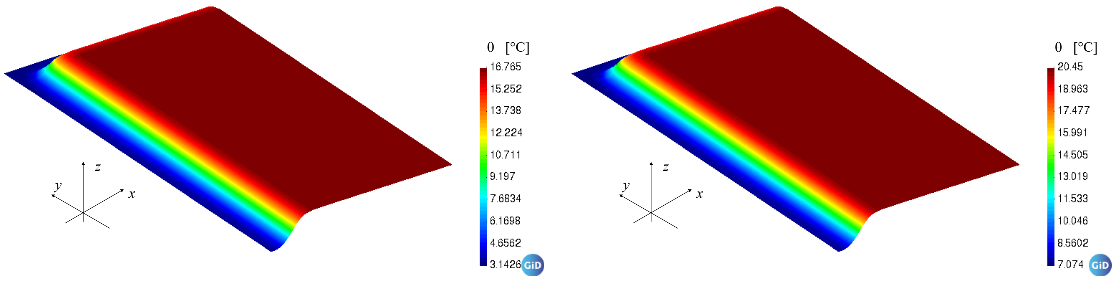

(a) (b)

Figure 5.18: Example 4. L-shaped shadow. Steady-state temperature distribution in correspondence of the a) external and b) internal glass surfaces.

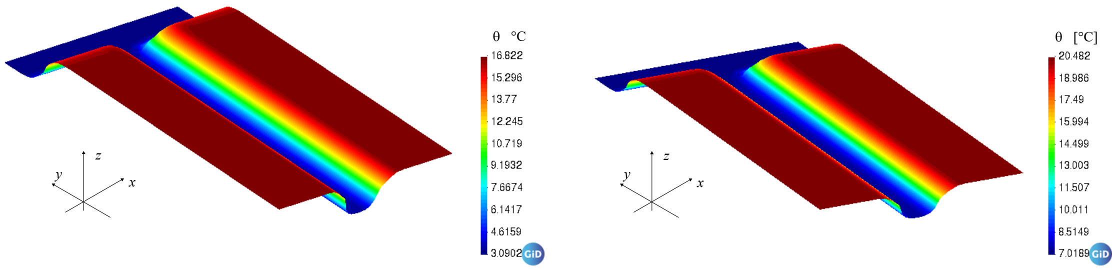

(a) (b)

Figure 5.19: Example 4. T-shaped shadow. Steady-state temperature distribution in correspondence of the a) external and b) internal glass surfaces.

Observe that the temperatures on the homogeneous parts of both regions A and B take the same values for the three cases. The temperature transition between the two regions has the same sigmoidal shape shown in Figure 5.12. This is emphasized by the graphs of Figure 5.21, showing the steady state temperature distribution across the lines L_1, L_2 and L_3 indicated in Figure 5.16, at both the external ($z = 0$) and internal ($z = s$) surfaces.

These results confirm that the sigmoidal trend in the transition region, and the width of the region itself, of about 0.2 m, do not depend on the shape of the shadow. However, one can expect that, when the shaded region is “thin” (its width is lower than 0.2 m), the sigmoid cannot completely develop. Morever, when regions A and B present re-entrant corners, as it is the case for the panel with a V-shaped shadow of Figure 5.20, the temperature distribution can be quite complicated at the corner points.

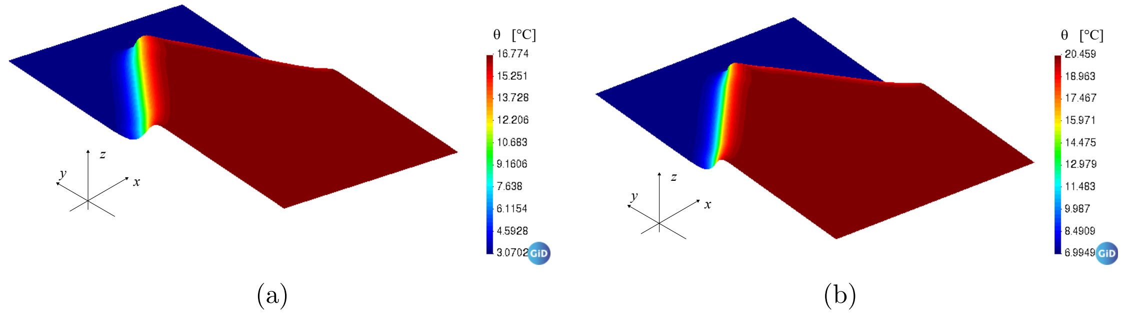

Figure 5.20: Example 4. V-shaped shadow. Steady-state temperature distribution in correspondence of the a) external and b) internal glass surfaces.

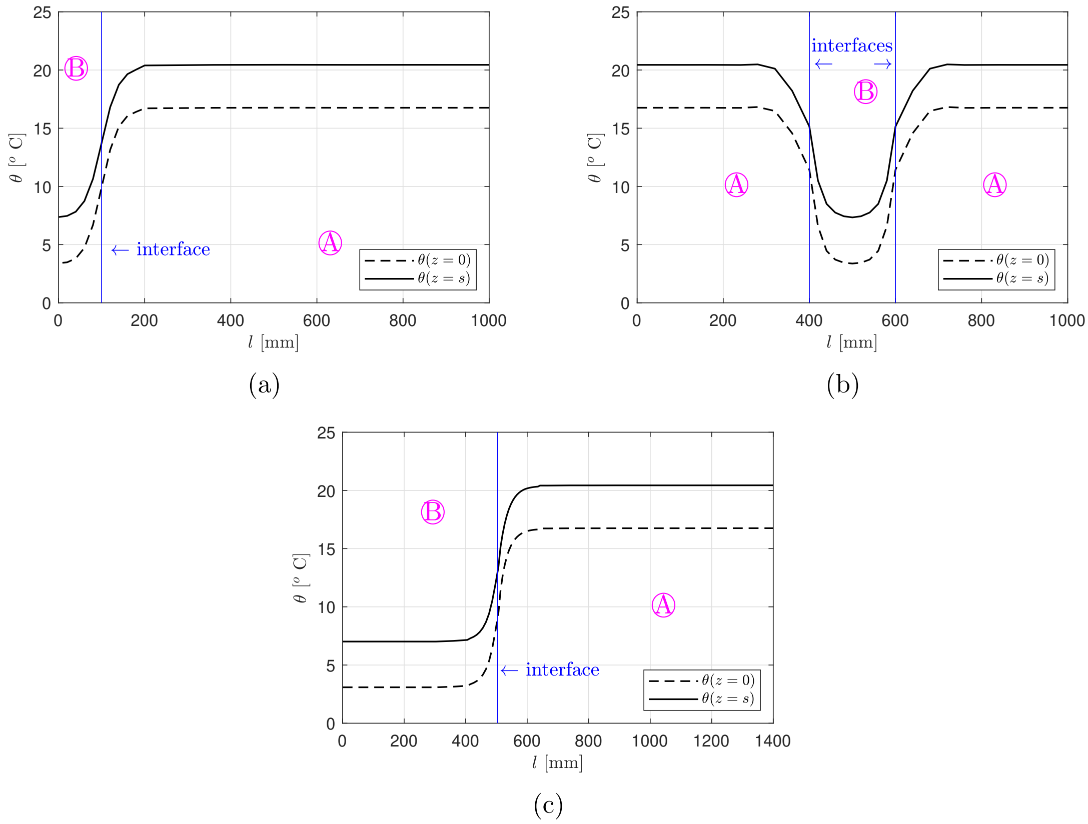

Figure 5.21: Example 4. Temperature distribution at the external ($z = 0$) and internal ($z = s$) surfaces, for the pane with a) L-shaped, b) T-shaped and c) V-shaped shadow.

Modulo the fact that in these examples the heat transmission through the fixing systems is neglected, a possible general conclusion would be that the temperatures in the irradiated and shaded regions are practically independent of the size and shape of the shadow. The temperatures are substantially uniform in each region A or B, apart from a strip across the interface, where they connect with a sigmoidal curve. However, this does not imply at all that the thermal stress is independent of the shape and size of the shadows, since, as confirmed by a recent study [109], this is certainly influenced by possible sources of concentrations. The stress concentrations depend upon the shape of regions A and B, and are particularly sensitive to the presence of corner points and their opening angle.

3.*Influence of the glazing thickness*

In previous studies [83], it was proposed that the width of the conductive strip, representing the region of transition between fully irradiated and shaded zones, is one order of magnitude greater than the thickness of the plate s. This datum is important because it is used in simplified engineering models [107], [110] to estimate the temperature distribution in architectural glazing. Constant environmental conditions, with the same parameters considered before, were assumed. A parametric analysis has been made, to evaluate the relation between the width of the transition region, hereafter denoted to as w, and the panel thickness s.

Preliminary analyses provided evidence that w is approximatively the same in monolithic glass and laminated glass with the same total thickness. For the sake of example, Figure 5.22 shows the temperature distribution at the steady state, for the geometry of Figure 5.10, with $\beta = 0.5$, obtained for a laminated glass composed of two glass plies of thickness $s_1 = 6$ mm, and $s_3 = 12$ mm, and a PVB interlayer of thickness $s_2 = 1.5$ mm, and for a monolithic element 19.5 mm thick. The results confirm that, even if surface temperature are different, the width of the transition region is approximately the same in the two cases.

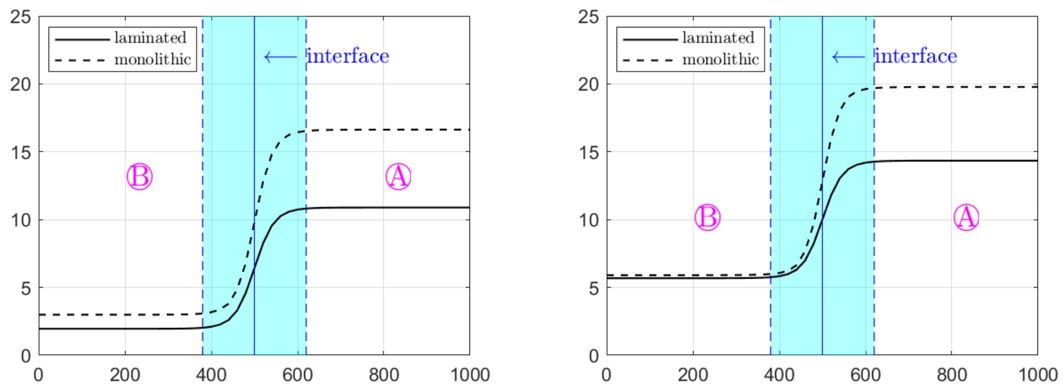

(a) (b)

Figure 5.22: Example 4. Spatial temperature distribution at the a) external and b) internal panel surfaces, in steady-state conditions, for 6 mm + 1.5 mm + 12 mm laminated and 19 mm thick monolithic element. Same geometry of Figure 5.10 for $\beta = 0.5$.

Therefore, the parametric analysis is reported for monolithic panes with thickness varying in the standard range for architectural glazing ($s = 3 \div 19$ mm). Figures 5.23(a) and 5.23(b) respectively show the temperature profile along x on the external an internal panel surfaces, for different values of s in steady-state condition. Observe that the width of the conductive strip, where $\theta(\mathbf{x}, t)$ presents the sigmoidal trend, increases with s. By comparing the Figures observe that, as expected, thick panes present an higher temperature difference between external and internal surfaces than thin panes. Indeed, for a given through-the-thickness heat flux, the temperature variation is higher for higher values of s.

The width of the transition zone is defined as that for which the temperatures differs from those of the neighboring homogeneous parts of regions A and B of more

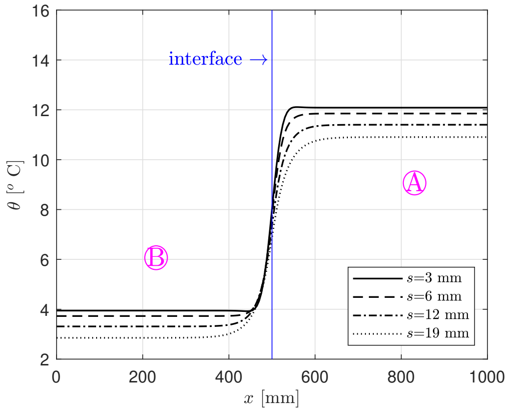

(a)

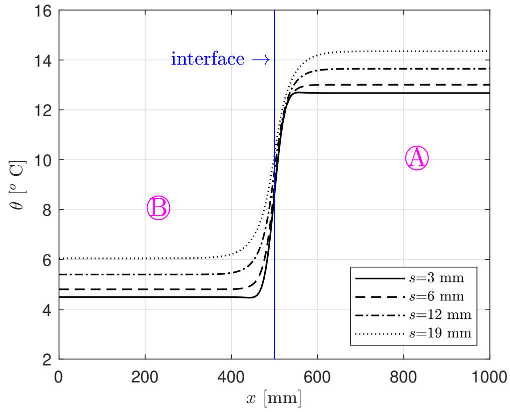

(b)

Figure 5.23: Example 4. Spatial temperature distribution at the a) external and b) internal panel surfaces, in steady-state conditions, for different monolithic panel thicknesses s. Same geometry of Figure 5.10 for $\beta = 0.5$.

than a fixed value (tolerance), here assumed to be 0.1 °C. To accurately capture the trend, the mesh was refined by placing 5 mm thick elements in the x direction in a strip 300 mm width, across the interface , while only one element was used in the glass thickness. Figure 5.24 shows such width of the transition region on both the external (w_{ext}) and the internal (w_{int}) surfaces, as a function of s.

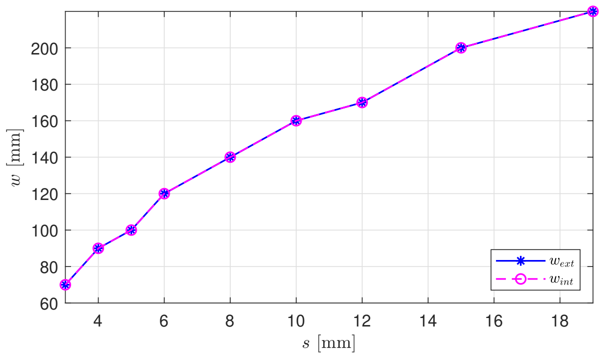

Figure 5.24: Example 4. Width of the temperature transition region, as a function of the monolithic plate thickness on the external (w_{ext}) and the internal (w_{int}) surfaces. Same geometry of Figure 5.10 for $\beta = 0.5$

Observe that $w_{ext} = w_{int}$ and their trend is approximately linearly dependent on s. As an engineering rule of practice, it is reasonable to assume that $w = w_{ext} = w_{int}$ is about 15 times the thickness of the plate. This indication is of paramount importance, because simplified models, such as those presented in [107], [110], [111], allow to estimate, with reasonable accuracy, the temperatures at a distance from the interface in the regions A and B, where they are uniform: one can thus connect such temperatures with a sigmoidal profile in the transition zone once w is known, to completely define the temperature field. Then, a commercial FEM code can be used to calculate the thermal stress. Naturally, the state of stress depends on the gradient of the thermal strain, and for this reason it is important to carefully evaluate the temperature profile in the transition zone.

Chapter 6

Conclusions

This thesis presents an investigation into the thermoelastic analysis of laminated structures, offering insights into design, analysis, and practical implications. The research focused on the structural response of laminated glass beams and transient heat conduction analysis in composite structures, primarily utilizing variational approaches. This final section summarizes the key findings, evaluates the extent to which the objectives were achieved, and discusses the implications of the results, including potential applications and limitations. Lastly, recommendations for future research are proposed to further advance the field and address remaining challenges.

6.1 The Special Zigzag Theory for Inflexed Laminates

This research has successfully developed the "Special Zigzag" theory, a simplified version of the refined zigzag theory that effectively captures the mechanical response of laminated composites. It is particularly applicable to laminated glass beams during the pre-breakage phase. The theory accounts for the slenderness of the glass plies and their high shear modulus relative to the polymeric interlayer, as well as the interlayer's softness. It models the glass plies as Euler-Bernoulli beams, coupled in shear through the soft interlayer, and approximates the viscoelastic response of the interlayer by neglecting its memory and using a quasi-elastic approach.

The straightforward nature of this theory enables the formulation of differential equations that can be solved analytically for statically determinate beams. Slip between glass plies at the beam ends is managed as a geometrical boundary condition, represented by a field corresponding to the average shear angle. Furthermore, the research incorporates a numerical implementation of the theory within a Finite Element (FE) model, facilitating the analysis of more complex scenarios.

The primary benefit of the Special Zigzag theory lies in its simplicity, making it highly valuable for engineering applications. The analytical solutions can be easily integrated into Excel spreadsheets for designing and verifying various laminated glass configurations. Nevertheless, this approach is confined to the linear regime; exploring geometrical non-linearities and the interlayer's viscoelastic effects through fractional calculus represents a promising avenue for future research.

In the specific context of a glass balustrade, the intermediate constraints necessitated segmenting the solution domain into two parts, which were later assembled using appropriate matching conditions. Geometric boundary conditions were applied to the kinematic variables based on the static configuration of the structure, while natural boundary conditions were derived from the relevant variational principle. The model accommodates cross-sectional warping at the beam ends, thereby capturing the real-world scenario of imperfect constraints.

The analysis revealed that significant shear stress concentration in the simply supported section of the balustrade leads to substantial straining of the interlayer, which greatly influences the overall structural behavior. The findings include explicit formulas for deflection and average shear angle, enabling comprehensive stress state calculations for the laminated beam. We derived an exact expression for "effective thickness," defined as the thickness of a monolithic beam with equivalent bending properties regarding stress and deflection. However, the comprehensive explicit solution reduces the necessity for effective thickness. Nonetheless, this derived metric was utilized to compare our approach, which can handle laminates of arbitrary composition, with existing methods in the literature that are limited to three-layer laminated sections.

This investigation operates within the linear regime, where moderate deflection occurs. The impact of geometrical non-linearity is minimal, and second-order effects have negligible influence on the bending and shear diagrams. The viscoelastic response of the polymeric interlayer has not been incorporated, which could enhance the model's development. However, this response is not likely to significantly affect the results due to the brief duration of the applied loads. Thus, a linear elastic assumption for the interlayer, based on a secant shear modulus derived from relaxation tests, is a valid approximation for this problem.

A limitation of this model is its restriction to the linear case. While it is feasible to account for geometric nonlinearity, doing so would lead to a system of differential equations that are challenging to solve analytically. Another potential enhancement involves incorporating the viscoelastic properties of the interlayers, which could be effectively modeled using fractional calculus to describe the viscoelastic response [27].

Additionally, it will be valuable to explore the effects of the model's assumptions on the global behavior of a structure, such as its buckling loads and dynamic response.

Although these refinements will be explored in future developments, the true strength of the proposed approach lies in its simplicity, making it particularly useful for engineering applications.

6.2 The Neat Variational Principle for Thermal Problems in Solids

A novel flux-based variational principle has been developed, representing an advancement of Biot's ingenious variational principle for thermal analysis. This new "neat" principle relies on the weak form of conservation of energy, wherein the Fourier equation serves as a holonomic constraint. This approach emphasizes the heat displacement field—whose time derivative is the heat flux—as the primary variable, contrasting with Biot's method, which incorporates the temperature field into the variational principle. After determining the unknown heat displacement field, the temperature field is retrieved from Fourier's law, along with appropriate boundary and initial conditions.

An interesting formal similarity is observed between the heat displacement field in the thermal problem and the displacement field in mechanical problems, suggesting a commonality in the numerical formulation of thermoelastic problems that warrants further exploration in future research. Based on this, a mechanical analogy is presented for the 1-D case, where the variational principle aligns formally with the equations governing the equilibrium of an elastic bar subjected to viscous constraints.

Furthermore, the flux-based approach allows for a natural treatment of flux boundary conditions, the fourth-order radiation law, and interfacial thermal resistance. However, further investigations are needed regarding the stability of the flux-based formulation to ensure the absence of spurious solutions. This should include studying the Ladyzhenskaya–Babuška–Brezzi (LBB) or inf-sup conditions, performing patch tests, and conducting convergence analyses with a higher number of numerical experiments.

This novel variational principle facilitates the formulation of a C^0 isoparametric finite element. In comparison to standard approaches, where the scalar temperature field is approximated using finite elements or finite differences, the new method relies on approximating the heat displacement vector field, which is much more regular than the temperature field. This allows for a clean treatment of problems with significant temperature gradients, which are challenging to address using traditional methods due to the spatial derivative of temperature requiring higher refinement of the solution domain. The finite element approach, implemented in a custom code, was employed to solve numerous benchmark examples, showing increased accuracy compared to Biot's original approach and excellent agreement with Fourier's series solution, along with improved efficiency.

The neat flux-based variational principle is also used to study specific problems related to laminated glass, particularly concerning uneven heating conditions caused by shadows and supporting frames that block solar radiation. This work is critical for practical engineering problems, as thermally induced stress is a major cause of glass breakage, especially under uneven irradiation conditions. A variety of real-world examples have been considered to provide a comprehensive analysis of these practical issues.

The effects of shadow size and shape on temperature distribution are analyzed for both monolithic and laminated glass. The temperature is found to be regular in regions distant from the interface between shaded and unshaded areas, while in the transition area, the temperature profile exhibits a sigmoidal shape. The size of this transition area is approximately an order of magnitude larger than the glass thickness, typically around 10-15 times. Furthermore, the results indicate that the temperature difference between shadowed and unshaded areas is minimally affected by the size and shape of the shadow. This finding is significant for design and analysis purposes, as it reduces the number of scenarios that require evaluation. However, this does not imply that thermal stress is independent of shadow shape and size; it is expected that thermal stress will concentrate at the corners of shaded areas. This work confirms the usability of simplified models for architectural glazing,where these simple models assume a uniform temperature in areas far from the interface, with an approximation of the size of the transient area; the uniform profiles can be connected by a sigmoidal curve.

Future developments should focus on incorporating materials with temperature-dependent thermal properties and integrating convection between a solid and a moving fluid without relying on the local heat transfer coefficient at the surface, which presents significant challenges. Notably, even in the subsonic flow regime, the local heat transfer coefficient can be out of phase with temperature by 45 degrees. This implies that, on a quarter of the boundary surface between the solid and the fluid, the heat flow direction may erroneously oppose the temperature difference between them. Additionally, incorporating the non-linear radiation law into the model will enable the simulation of problems with high temperature variations, as present in extreme environments like outer space.

Bibliography

[1] E. Oñate, *Structural analysis with the finite element method. Linear statics: volume 2: beams, plates and shells*. Springer Science & Business Media, 2013.

[2] K. H. Lo, R. M. Christensen, and E. M. Wu, "A High-Order Theory of Plate Deformation—Part 1: Homogeneous Plates," *Journal of Applied Mechanics*, vol. 44, no. 4, pp. 663–668, Dec. 1977.

[3] J. N. Reddy and C. F. Liu, "A higher-order shear deformation theory of laminated elastic shells," *International Journal of Engineering Science*, vol. 23, no. 3, pp. 319–330, 1985, ISSN: 0020-7225.

[4] L. Dahsin and L. Xiaoyu, "An overall view of laminate theories based on displacement hypothesis," *Journal of Composite Materials*, vol. 30, no. 14, pp. 1539–1561, 1996.

[5] E. J. Barbero, J. N. Reddy, and J. Teply, "An accurate determination of stresses in thick laminates using a generalized plate theory," *International Journal for Numerical Methods in Engineering*, vol. 29, no. 1, pp. 1–14, 1990.

[6] L. Chun-Ying and L. Dahsin, "An interlaminar stress continuity theory for laminated composite analysis," *Computers & Structures*, vol. 42, no. 1, pp. 69–78, 1992, ISSN: 0045-7949.

[7] M. DI Sciuva, "Bending, vibration and buckling of simply supported thick multilayered orthotropic plates: An evaluation of a new displacement model," *Journal of Sound and Vibration*, vol. 105, no. 3, pp. 425–442, 1986, ISSN: 0022-460X.

[8] H. Murakami, "Laminated composite plate theory with improved in-plane responses," *Journal of Applied Mechanics*, vol. 53, pp. 661–666, 1986.

[9] E. Reissner, "On a certain mixed variational theorem and a proposed application," English, *International journal for numerical methods in engineering*, 1984, ISSN: 0029-5981.

[10] P. C. Chou and J. Carleone, "Transverse shear in laminated plate theories.," *AIAA Journal*, vol. 11, no. 9, pp. 1333–1336, 1973.

[11] R. C. Averill, "Static and dynamic response of moderately thick laminated beams with damage," *Composites Engineering*, vol. 4, no. 4, pp. 381–395, 1994, ISSN: 0961-9526.

[12] V. R. Aitharaju and R. C. Averill, "C^0 zig-zag finite element for analysis of laminated composite beams," *Journal of Engineering mechanics*, vol. 125, no. 3, pp. 323–330, 1999.

[13] M. Cho and R. R. Parmerter, “Efficient higher order composite plate theory for general lamination configurations,” *AIAA Journal*, vol. 31, no. 7, pp. 1299–1306, 1993.

[14] A. Tessler, M. DI Sciuva, and M. Gherlone, “Refinement of timoshenko beam theory for composite and sandwich beams using zigzag kinematics,” Tech. Rep., 2007.

[15] A. Tessler, M. DI Sciuva, and M. Gherlone, “A consistent refinement of first-order shear deformation theory for laminated composite and sandwich plates using improved zigzag kinematics,” *Journal of Mechanics of Materials and Structures*, vol. 5, pp. 341–367, Aug. 2010.

[16] A. Tessler, M. DI Sciuva, and M. Gherlone, “A homogeneous limit methodology and refinements of computationally efficient zigzag theory for homogeneous, laminated composite, and sandwich plates,” *Numerical Methods for Partial Differential Equations*, vol. 27, pp. 208–229, Jan. 2011.

[17] M. Gherlone, A. Tessler, and M. DI Sciuva, “C0 beam elements based on the refined zigzag theory for multilayered composite and sandwich laminates,” *Composite Structures*, vol. 93, no. 11, pp. 2882–2894, 2011, ISSN: 0263-8223.

[18] E. Oñate, A. Eijo, and S. Oller, “Simple and accurate two-noded beam element for composite laminated beams using a refined zigzag theory,” *Computer Methods in Applied Mechanics and Engineering*, vol. 213-216, pp. 362–382, 2012, ISSN: 0045-7825.

[19] A. Haydar and G. Royer-Carfagni, “A Simple Model for Inflexed Multilayered Laminated Glass Beams Based on Refined Zig-Zag Theory,” *Journal of Applied Mechanics*, vol. 90, no. 1, p. 011 002, Oct. 2022, ISSN: 0021-8936.

[20] L. Galuppi and G. Royer-Carfagni, “The post-breakage response of laminated heat-treated glass under in plane and out of plane loading,” *Composites Part B: Engineering*, vol. 147, pp. 227–239, 2018, ISSN: 1359-8368.

[21] R. A. Behr, J. E. Minor, and H. S. Norville, “Structural behavior of architectural laminated glass,” *Journal of Structural Engineering*, vol. 119, no. 1, pp. 202–222, 1993.

[22] Y. Shitanoki, S. J. Bennison, and Y. Koike, “Analytic Models of a Thin Glass–Polymer Laminate and Development of a Rational Engineering Design Methodology,” *Journal of Applied Mechanics*, vol. 81, no. 12, p. 121 009, Dec. 2014, ISSN: 0021-8936.

[23] L. Galuppi and G. Royer-Carfagni, “The effective thickness of laminated glass: Inconsistency of the formulation in a proposal of en-standards,” *Composites Part B: Engineering*, vol. 55, pp. 109–118, 2013, ISSN: 1359-8368.

[24] L. Galuppi and G. Royer-Carfagni, “Laminated beams with viscoelastic interlayer,” *International Journal of Solids and Structures*, vol. 49, no. 18, pp. 2637–2645, 2012, ISSN: 0020-7683.

[25] M. Di Paola, L. Galuppi, and G. Royer Carfagni, “Fractional viscoelastic characterization of laminated glass beams under time-varying loading,” *International Journal of Mechanical Sciences*, vol. 196, p. 106 274, 2021, ISSN: 0020-7403.

[26] L. Viviani, M. Di Paola, and G. Royer-Carfagni, "Fractional viscoelastic modeling of laminated glass beams in the pre-crack state under explosive loads," *International Journal of Solids and Structures*, vol. 248, p. 111 617, 2022, ISSN: 0020-7683.

[27] L. Viviani, M. Di Paola, and G. Royer-Carfagni, "A fractional viscoelastic model for laminated glass sandwich plates under blast actions," *International Journal of Mechanical Sciences*, vol. 222, p. 107 204, 2022, ISSN: 0020-7403.

[28] L. Galuppi and G. Royer-Carfagni, "Buckling of three-layered composite beams with viscoelastic interaction," *Composite Structures*, vol. 107, pp. 512–521, 2014, ISSN: 0263-8223.

[29] A. Van Duser, A. Jagota, and S. Bennison, "Analysis of glass/polyvinyl butyral laminates subjected to uniform pressure," *Journal of Engineering Mechanics*, vol. 125, no. 4, pp. 435–442, 1999.

[30] E. Wölfel, "Nachgiebiger verbund. eine näherungslösung und deren anwendungsmöglichkeiten," *Der Stahlbau*, vol. 56, no. 6, 1987.

[31] ASTM, *ASTM E-1300. Standard Practice for Determining Load Resistance of Glass in Buildings*. 2016.

[32] L. Galuppi and G. Royer-Carfagni, "Effective thickness of laminated glass beams: New expression via a variational approach," *Engineering Structures*, vol. 38, pp. 53–67, 2012.

[33] L. Galuppi and G. Royer-Carfagni, "The effective thickness of laminated glass plates," *Journal of Mechanics of Materials and Structures*, vol. 7, no. 4, pp. 375–400, 2012.

[34] L. Galuppi and G. Royer-Carfagni, "Enhanced effective thickness of multi-layered laminated glass," *Composites Part B: Engineering*, vol. 64, pp. 202–213, 2014.

[35] CEN, *FprCEN/TS 19100/2. Design of glass structures - Part 2: Design of out-of-plane loaded glass components*. 2021.

[36] L. Galuppi, G. Manara, and G. Royer Carfagni, "Practical expressions for the design of laminated glass," *Composites Part B: Engineering*, vol. 45, no. 1, pp. 1677–1688, 2013.

[37] L. Galuppi, G. Manara, and G. Royer Carfagni, "Erratum: Practical expressions for the design of laminated glass (composites part b: Engineering (2013) 45 (1677-1688))," *Composites Part B: Engineering*, vol. 56, pp. 599–601, 2014.

[38] V. I. Newmark NM Siess CP, "Test and analysis of composite beams with incomplete interaction," *Proceedings Society Experimental Stress Analysis*, vol. 9, pp. 75–92, 1951.

[39] J. N. Reddy, "A generalization of two-dimensional theories of laminated composite plates," *Communications in Applied Numerical Methods*, vol. 3, pp. 173–180, 1987.

[40] D. Owen and Z. Li, "Elasto-plastic numerical analysis of anisotropic laminated plates by a refined finite element model," in *Computational Plasticity: Models Software and Application*, E. O. E. Owen R Hinton, Ed., Swansea, UK: Pineridge Press, 1987, pp. 749–775.

[41] M. Amabili, P. Balasubramanian, R. Garziera, and G. Royer-Carfagni, "Blast loads and nonlinear vibrations of laminated glass plates in an enhanced shear deformation theory," *Composite Structures*, vol. 252, p. 112 720, 2020.

[42] M. DI Sciuva, "An improved shear-deformation theory for moderately thick multilayered anisotropic shells and plates," *Journal of Applied Mechanics*, vol. 54, pp. 589–596, 1987.

[43] M. DI Sciuva, "Development of an anisotropic, multilayered, shear-deformable rectangular plate element," *Computers & structures*, vol. 21, no. 4, pp. 789–796, 1985.

[44] R. C. Averill, "Static and dynamic response of moderately thick laminated beams with damage," *Composites Engineering*, vol. 4, no. 4, pp. 381–395, 1994.

[45] A. Tessler, M. DI Sciuva, and M. Gherlone, "A refined zigzag beam theory for composite and sandwich beams," *Journal of Composite Materials*, vol. 43, no. 9, pp. 1051–1081, 2009.

[46] D. Baraldi, "A simple mixed finite element model for laminated glass beams," *Composite Structures*, vol. 194, pp. 611–623, 2018.

[47] L. Galuppi and G. Royer-Carfagni, "Conjugate-beam analogy for inflexed laminates," *International Journal of Solids and Structures*, vol. 206, pp. 396–411, 2020, cited By 2.

[48] G. H. Silva, R. L. Riche, J. Molimard, and A. Vautrin, "Exact and efficient interpolation using finite elements shape functions," *European Journal of Computational Mechanics*, vol. 18, no. 3-4, pp. 307–331, 2009.

[49] V. Quaglini, S. Cattaneo, and L. Biolzi, "Numerical assessment of laminated cantilevered glass plates with point fixings," *Glass Structures & Engineering*, vol. 5, no. 2, pp. 187–204, 2020.

[50] L. Galuppi and A. J. Nizich, "Cantilevered laminated glass balustrades: The conjugate beam effective thickness method—part i: The analytical model," *Glass Structures & Engineering*, vol. 6, no. 4, pp. 377–395, 2021.

[51] A. Haydar and G. Royer-Carfagni, "Analytical Solution and Exact Effective Thickness of Multilayered Laminated Glass Cantilevered Balustrades," *Journal of Applied Mechanics*, vol. 90, no. 6, p. 061 003, Feb. 2023, ISSN: 0021-8936.

[52] L. Galuppi and G. Royer-Carfagni, "Enhanced effective thickness of multi-layered laminated glass," *Composites Part B: Engineering*, vol. 64, pp. 202–213, 2014, ISSN: 1359-8368.

[53] A. J. Nizich and L. Galuppi, "Cantilevered laminated glass balustrades: The conjugate beam effective thickness method—part II: Comparison and application," *Glass Structures & Engineering*, vol. 7, no. 1, pp. 23–43, 2022.

[54] I. Calderone, P. Davies, S. J. Bennison, H. Xiaokun, and L. Gang, "Effective laminate thickness for the design of laminated glass," *Proceedings of Glass performance days*, pp. 12–15, 2009.

[55] D. E. Carlson, “Linear thermoelasticity,” in *Linear Theories of Elasticity and Thermoelasticity: Linear and Nonlinear Theories of Rods, Plates, and Shells*, Springer, 1973, pp. 297–345.

[56] J. P. Carter and J. R. Booker, “Finite element analysis of coupled thermoelasticity,” *Computers & Structures*, vol. 31, no. 1, pp. 73–80, 1989, Special Issue: Finite Element Methods in Engineering, ISSN: 0045-7949.

[57] H. S. Carslaw and J. C. Jaeger, *Conduction of Heat in Solids*, 2nd ed. Oxford: Oxford University Press, 1959.

[58] J. B. J. Fourier, *Théorie analytique de la chaleur.* Gauthier-Villars, 1888, vol. 1.

[59] J. H. I. Lienhard and J. H. V. Lienhard, *A heat transfer textbook, 5th edition.* Phlogiston press, 2019.

[60] T. J. LARDNER, “Biot’s variational principle in heat conduction,” *AIAA Journal*, vol. 1, no. 1, pp. 196–206, 1963.

[61] P. L. Kapitza, “Heat transfer and superfluidity of helium ii,” *Phys. Rev.*, vol. 60, pp. 354–355, 4 Aug. 1941.

[62] Y. Benveniste and T. Miloh, “The effective conductivity of composites with imperfect thermal contact at constituent interfaces,” *Int J Eng Sci*, vol. 24, no. 9, pp. 1537–1552, 1986.

[63] R. Lipton and B. Vernescu, “Composites with imperfect interface,” *Proc R Soc Lond A*, vol. 452, no. 1945, pp. 329–358, 1996.

[64] C.-W. Nan, R. Birringer, D. R. Clarke, and H. Gleiter, “Effective thermal conductivity of particulate composites with interfacial thermal resistance,” *J Appl Phys*, vol. 81, no. 10, pp. 6692–6699, 1997.

[65] J. Chen, X. Xu, J. Zhou, and B. Li, “Interfacial thermal resistance: Past, present, and future,” *Reviews of Modern Physics*, vol. 94, no. 2, p. 025 002, 2022.

[66] R. Peterson and A. Anderson, “Acoustic-mismatch model of the kaptiza resistance,” *Physics Letters A*, vol. 40, no. 4, pp. 317–319, 1972, ISSN: 0375-9601.

[67] W. A. Little, “The transport of heat between dissimilar solids at low temperatures,” *Canadian Journal of Physics*, vol. 37, no. 3, pp. 334–349, 1959.

[68] L. Onsager, “Reciprocal relations in irreversible processes. i.,” *Phys. Rev.*, vol. 37, pp. 405–426, 4 Feb. 1931.

[69] L. Onsager, “Reciprocal relations in irreversible processes. ii.,” *Phys. Rev.*, vol. 38, pp. 2265–2279, 12 Dec. 1931.

[70] J. W. S. B. Rayleigh, *The theory of sound.* Macmillan, 1896, vol. 2.

[71] P. Rosen, “On Variational Principles for Irreversible Processes,” *The Journal of Chemical Physics*, vol. 21, no. 7, pp. 1220–1221, Jul. 1953, ISSN: 0021-9606.

[72] L. G. CHAMBERS, “A variational principle for the conduction of heat,” *The Quarterly Journal of Mechanics and Applied Mathematics*, vol. 9, no. 2, pp. 234–235, Jan. 1956, ISSN: 0033-5614.

[73] M. A. Biot, "New methods in heat flow analysis with application to flight structures," *Journal of the Aeronautical Sciences*, vol. 24, no. 12, pp. 857–873, 1957.

[74] S. D. NIGAM and H. C. AGRAWAL, "A variational principle for convection of heat," *Journal of Mathematics and Mechanics*, vol. 9, no. 6, pp. 869–883, 1960, ISSN: 00959057, 19435274.

[75] E. M. Sparrow and R. Siegel, "A Variational Method for Fully Developed Laminar Heat Transfer in Ducts," *Journal of Heat Transfer*, vol. 81, no. 2, pp. 157–164, May 1959, ISSN: 0022-1481.

[76] D. F. Hays and H. N. Curd, "Heat conduction in solids: Temperature-dependent thermal conductivity," *International Journal of Heat and Mass Transfer*, vol. 11, no. 2, pp. 285–295, 1968, ISSN: 0017-9310.

[77] E. Lorenzini, "A variational formulation applied to heat conduction equation," *Bulletins de l'Académie Royale de Belgique*, vol. 56, no. 1, pp. 367–379, 1970.

[78] A. Haydar, L. Galuppi, and G. Royer-Carfagni, "A neat flux-based weak formulation for thermal problems which develops biot's variational principle," *International Journal of Engineering Science*, vol. 202, p. 104 103, 2024, ISSN: 0020-7225.

[79] M. A. Biot, *Variational principles in heat transfer. A unified Lagrangian analysis of dissipative phenomena.* Oxford University Press, London, 1970.

[80] W. Yuan, N. Yu, L. Li, and Y. Fang, "Heat transfer analysis in multi-layered materials with interfacial thermal resistance," *Compos Struct*, vol. 293, p. 115 728, 2022.

[81] L. Galuppi and G. Royer-Carfagni, "Biot's variational method to determine the thermal strain in layered glazings," *Int J Sol Struct*, vol. 249, p. 111 657, 2022.

[82] L. Galuppi and G. Royer-Carfagni, "Thermal analysis of architectural glazing in uneven conditions based on Biot's variational principle: Part I - Description of the finite element modelling," *Glass Struct Eng*, vol. 8, pp. 41–56, 2023.

[83] L. Galuppi and G. Royer-Carfagni, "Thermal analysis of architectural glazing in uneven conditions based on Biot's variational principle: Part II - Validation and case-studies," *Glass Struct Eng*, pp. 1–24, 2023.

[84] O. C. Zienkiewicz, R. L. Taylor, and J. Z. Zhu, *The finite element method: its basis and fundamentals.* Elsevier, 2005.

[85] L. Galuppi, A. Haydar, and G. Royer-Carfagni, "Specialization of a new flux-based approach to thermal problems. numerical study of glass façades of buildings with cast shadows," *Journal of Building Engineering*, p. 110 949, 2024, ISSN: 2352-7102.

[86] G. Alvarez, J. Flores, and C. A. Estrada, "The thermal response of laminated glass with solar control coating," *Journal of Physics D: Applied Physics*, vol. 31, no. 21, p. 3057, 1998.

[87] K. Pietrak and T. S. Wisniewski, “Methods for experimental determination of solid-solid interfacial thermal resistance with application to composite materials,” *Journal of Power Technologies*, vol. 94, no. 4, p. 270, 2014.

[88] “EN 572-1 – Glass in building – Basic soda lime silicate glass products. Part 1: Definitions and general physical and mechanical properties,” CEN/TC 129, Standard, 2012.

[89] “N180E – Glass and Thermal Safety,” CEN/TC129/WG8 – Pilkington, Standard, 2004.

[90] C. Carrot, A. Bendaoud, C. Pillon, O. Olabisi, and K. Adewale, “Polyvinyl butyral,” in *Handbook of Thermoplastics, red.* ACRC Press, 2016, pp. 89–138.

[91] “ISO 15099 – Thermal Performance of windows, doors and shading devices – Detailed calculation,” ISO/TC 163/SC 2, Standard, 2003.

[92] C. Marino, A. Nucara, M. Pietrafesa, and E. Polimeni, “The effect of the short wave radiation and its reflected components on the mean radiant temperature: Modelling and preliminary experimental results,” *J Build Eng*, vol. 9, pp. 42–51, 2017.

[93] “EN ISO 6946 – Building components and building elements – Thermal resistance and thermal transmittance – Calculation method,” ISO/TC 163 and CEN/TC 89, Standard, 2007.

[94] K. J. A. Revfeim, “Simplified relationships for estimating solar radiation incident on any flat surface,” *Sol Energy*, vol. 28, no. 6, pp. 509–517, 1982.

[95] C. Demain, M. Journée, and C. Bertrand, “Evaluation of different models to estimate the global solar radiation on inclined surfaces,” *Renew Energy*, vol. 50, pp. 710–721, 2013.

[96] J. L. Wright, “Calculating center-glass performance indices of windows,” *ASHRAE Transactions*, vol. 121, 1998.

[97] K. Vengatesan, “Windows film to glass: Numerical simulation software for avoiding thermal stress,” Ph.D. dissertation, IST Tecnico Lisboa Lisbon, Portugal, 2017.

[98] L. Evangelisti, C. Guattari, F. Asdrubali, and R. de Lieto Vollaro, “An experimental investigation of the thermal performance of a building solar shading device,” *Journal of Building Engineering*, vol. 28, p. 101 089, 2020.

[99] “NF DTU 39 P3 Travaux de bâtiment – Travaux de vitrerie-miroiterie – Partie 3: Mémento calculs des contraintes thermiques,” CSTB, Standard, 2006.

[100] L. Fox, “Some experiments with singularities in linear elliptic partial differential equations,” *Proc R Soc Lond A*, vol. 323, no. 1553, pp. 179–190, 1971.

[101] Z. Yosibash, *Singularities in elliptic boundary value problems and elasticity and their connection with failure initiation.* Springer, 2012.

[102] MATLAB, *version R2023a - academic use.* Natick, Massachusetts: The MathWorks Inc., 2023.

[103] M. Poláková, S. Schäfer, and M. Elstner, "Thermal glass stress analysis–design considerations," in *Challenging Glass Conference Proceedings*, vol. 6, 2018, pp. 725–740.

[104] L. Galuppi, A. Franco, and C. Bedon, "Architectural glass under climatic actions and fire: Review of state of the art, open problems and future perspectives," *Build*, vol. 13, no. 4, p. 939, 2023.

[105] D. Stahn, "Thermal stresses in heat-absorbing building glass subjected to solar radiation," in *Thermal Stresses in Severe Environments*, Springer, 1980, pp. 305–323.

[106] P. Foraboschi, "Analytical modeling to predict thermal shock failure and maximum temperature gradients of a glass panel," *Materials & Design*, vol. 134, pp. 301–319, 2017.

[107] L. Galuppi, M. Maffeis, and G. Royer-Carfagni, "Enhanced engineered calculation of the temperature distribution in architectural glazing exposed to solar radiation," *Glass Struct Eng*, vol. 6, pp. 425–448, 2021.

[108] "CNR-DT 210/2013 - Guide for the Design, Construction and Control of Buildings with Structural Glass Elements," National Research Council of Italy, Standard, 2013.

[109] S. Zandekarimi and G. Royer Carfagni, "The stress state in an elastic disk due to a temperature variation in one sector," *J Appl Mech*, vol. in press, 2024.

[110] L. Galuppi, M. Maffeis, and G. Royer-Carfagni, "Engineered calculation of the uneven in-plane temperatures in Insulating Glass Units for structural design," *Glass Struct Eng*, vol. 7, pp. 71–99, 2022.

[111] L. Galuppi, M. Maffeis, A. Haydar, and G. Royer-Carfagni, "Innovative FEM for the thermal analysis of architectural glazing exposed to solar radiation. Proposal for a simplified engineering approach," in *Proceedings of Glass Performance Days, Tampere (FI)*, 2023.

Acknowledgments

I would like to express my deepest gratitude to my supervisor, Prof. Gianni Royer-Carfagni, for his invaluable guidance, support, and encouragement throughout my research journey. His expertise and insightful feedback have been instrumental in shaping my work and helping me navigate the challenges of this project. I am truly grateful for the opportunity to learn from him and for his unwavering belief in my abilities.

I would like to extend my heartfelt thanks to my co-supervisor, Laura Galuppi, for her exceptional support throughout my research. Her expertise and constructive feedback have been invaluable in enhancing the quality of my work. I am grateful for her encouragement and for the insightful discussions that have enriched my understanding of the subject.

Special thanks to my girlfriend, Katerina Janisova, for helping me buy a discounted chair from Ikea.

I would also like to thank my parents for the decision to have more than three kids; otherwise, I wouldn't have been here. A special thanks also to my four siblings, whom I love dearly.

Special thanks to my dear friends from Brescia, Michelle Fabbri and Basel Dalla, who stood by me during difficult times.

Surely, I extend my gratitude to my friends and colleagues Braghin, Santi, Mangoni, Fusi, Peng, Zandekarimi, Soldati, Dalboni, and Viviani, Boni, for their support and all the fun moments and jokes we shared together.

Finally, I would like to acknowledge the partial financial support of my PhD from Maffeis Engineering SpA.